AFRL-VS-HA-TR-2006-1146

Collaborative Research: Ground Truth of African and Eastern Mediterranean Shallow Seismicity Using SAR Interferometry and Gibbs Sampling Inversion

Benjamin A. Brooks
Francisco Gomez
Eric Sandvol
L. Neil Frazer

University of Hawaii
2530 Dole St., ORS
SAK D200
Honolulu, HI 96822-2303

Final Report

5 October 2006

AIR FORCE RESEARCH LABORATORY
Space Vehicles Directorate
29 Randolph Road
AIR FORCE MATERIEL COMMAND
Hanscom AFB, MA 01731-3010

NOTICES

AFRL-VS-HA-TR-2006-1146 HAS BEEN REVIEWED AND IS APPROVED FOR PUBLICATION IN ACCORDANCE WITH ASSIGNED DISTRIBUTION STATEMENT.

//Signature//	//Signature//
ROBERT RAISTRICK Contract Manager	BRIAN GRIFFITH, Maj, USAF, Chief Battlespace Surveillance Innovation Center

0REPORT DOCUMENTATION PAGE

Form Approved
OMB No. 0704-0188

1. REPORT DATE *(DD-MM-YYYY)*
October 2006

2. REPORT TYPE
Final Report

3. DATES COVERED *(From - To)*
24-Dec-03 to 23-Jun-06

4. TITLE AND SUBTITLE
Collaborative Research: Ground Truth of African and Eastern Mediterranean Shallow Seismicity Using SAR Interferometry and Gibbs Sampling Inversion

5a. CONTRACT NUMBER
F19628-03-C-0107

5b. GRANT NUMBER

5c. PROGRAM ELEMENT NUMBER
62601F

6. AUTHOR(S)
Benjamin A. Brooks[1], Francisco Gomez[2], Eric A. Sandvol[2] and Neil Frazer[1]

5d. PROJECT NUMBER
1010

5e. TASK NUMBER
SM

5f. WORK UNIT NUMBER
A1

7. PERFORMING ORGANIZATION NAME(S) AND ADDRESS(ES)

University of Hawaii
2530 Dole St., ORS
SAK D200
Honolulu, HI 96822-2303

8. PERFORMING ORGANIZATION REPORT NUMBER

9. SPONSORING / MONITORING AGENCY NAME(S) AND ADDRESS(ES)
Air Force Research Laboratory
29 Randolph Road
Hanscom AFB, MA 01731-3010

10. SPONSOR/MONITOR'S ACRONYM(S)
AFRL/VSBYE

11. SPONSOR/MONITOR'S REPORT NUMBER(S)
AFRL-VS-HA-TR-2006- 1146

12. DISTRIBUTION / AVAILABILITY STATEMENT
Approved for Public Release; Distribution Unlimited.

13. SUPPLEMENTARY NOTES
[1] University of Hawaii
[2] University of Missouri

14. ABSTRACT

We evaluate the use of Synthetic Aperture Radar Interferometry (InSAR) to provide GT5 or better locations for shallow earthquakes of moderate size (Mw 5 – 6.5) in primarily Africa and the Middle East, although we also included some events from Asia. We find that InSAR is capable of routine detection of surface displacements associated with small (< Mw 5.5) seismic events. Additionally, we find that, in some cases, inversion of the surface displacement field alone can meet GT5 criteria. In many cases, however, although GT location criteria appear to be met by the inversion, the overall solution (including strike, rake, and dip of the fault plane) is not consistent with additional information such as focal mechanism and so there may be some question to its overall accuracy. This suggests that in order to start to properly create an InSAR/GT catalog, the next level inversion should incorporate prior information (properly propagating errors) such as the focal mechanism. We provide 2 new GT5 events for the existing catalog. We were successful in collecting seismic data from which we were able to measure origin times for all sixteen events. Collected waveforms for the Sultan Dagi, Turkey event help us identify the likely existence of a small foreshock.

15. SUBJECT TERMS
Location Calibration, InSAR, Geodetic Inversion

16. SECURITY CLASSIFICATION OF:

a. REPORT	b. ABSTRACT	c. THIS PAGE	17. LIMITATION OF ABSTRACT	18. NUMBER OF PAGES
U	U	U	SAR	77

19a. NAME OF RESPONSIBLE PERSON
Robert J. Raistrick

19b. TELEPHONE NUMBER *(include area code)*
781-377-3726

Table of Contents

Figures

1. INTRODUCTION

In order for nuclear monitoring to be most effective, variations in seismic travel times for specific regions must be accounted for in a process commonly referred to as 'location calibration'. To improve seismic event location using sparse regional networks, calibration employs empirical observations and/or the development of appropriate models that correct for the effects of earth seismic velocity heterogeneity *(Council, 1997; Pomeroy et al., 1982)*. The cornerstone for successful calibration of IMS stations at regional and near-teleseismic distances is the development of ground truth (GT) events that are well-located with well-defined location uncertainties (e.g. GT5 refers to event location error less than 5 km) (Myers and Schultz, 2000; Schultz et al., 1998). Empirical observations of GT events are necessary so that path propagation effects can be determined separately from source mislocation effects. For these efforts, GT5 or better events are most valuable, though in remote or hostile regions they are often difficult to acquire because of sparse seismic networks or inaccessibility of data.

Synthetic Aperture Radar Interferometry (InSAR), combined with elastic dislocation modeling, is an especially promising tool for acquiring GT information in remote areas (Begnaud et al., 2000b; Lohmann et al., 2002). For individual seismic events, InSAR has the capability of producing sub-centimeter surface displacement fields, which can be inverted for earthquake source given a kinematic model relating source to expected ground motion (e.g.Okada, 1985). The inverse problem is multiparametric (usually 9 parameters) and non-linear and so it requires fairly powerful techniques and substantial computational cost if issues such as resolution, uncertainty, and uniqueness are to accompany solutions for GT candidate events.

Under this contract, we have focused on evaluating the use of InSAR to provide GT5 or better locations for shallow earthquakes of moderate size (Mw 5 – 6.5) in primarily Africa and the Middle East, although we also included some events from Asia. Our principal goals for this project were:

1. To evaluate the InSAR technique in general for routine detection of surface displacements associated with small (< M_w 5.5) seismic events in remote areas such as North Africa and the Eastern Mediterranean.

2. To evaluate whether InSAR displacement fields combined with a Gibbs Sampling inversion approach to the coseismic geodetic inverse problem (Brooks and Frazer, 2005a) could routinely yield GT5 or better locations for the detected events and so be used to create a consistently determined InSAR GT catalog. It is important to note that in this initial phase our evaluation focused on inverting the surface displacement field without any preconditioning from other information sources (such as regional tectonic information) whose errors could be difficult to quantify.

3. To provide new GT5 events for the existing catalog. The areas studied comprise significant gaps in the existing database for GT events – for example, prior to our study, there were only 2 GT5 or better located events for the entire continent of Africa, despite the relatively large number of $M_w > 5$ events scattered throughout the region (Engdahl et al., 1998) (Figure 1).

4. We have collected seismic waveforms and travel times for sixteen events that we have estimated hypocentral locations from the INSAR data. We are providing these travel times and seismic waveforms on a DVD will all of the associated measured displacement fields.

In summary, and expanded upon in this report, our goals were achieved with varying success levels:

1. We find that InSAR is capable of routine detection of surface displacements associated with small ($< M_w$ 5.5) seismic events.

2. We find that, in some cases, inversion of the surface displacement field alone can meet GT5 criteria. In many cases, however, although GT location criteria appear to be met by the inversion, the overall solution (including strike, rake, and dip of the fault plane) is not consistent with additional information such as focal mechanism and so there may be some question to its overall accuracy. This suggests that in order to start to properly create an InSAR/GT catalog, the next level inversion should incorporate prior information (properly propagating errors) such as the focal mechanism.

3. We provide 2-4 new GT5 events for the existing catalog.

4. We were successful in collecting seismic data from which we were able to measure origin times for all sixteen events. Furthermore collected waveforms for the Sultan Dagi event help us identify the likely existence of a small foreshock.

2. BACKGROUND

2.1. InSAR

The most well-known examples of InSAR used as a geodetic tool involve images of co-seismic surface deformation of large ($M > 6.5$) earthquakes (Massonnet et al., 1993; Zebker et al., 1994) over hundreds to thousands of square kilometers. However, because the technique can be sensitive to surface deformations on the order of a few millimeters (Peltzer and Rosen, 1995) with pixel sizes of 10s of meters, InSAR is now becoming an effective tool for measuring of subtle earthquake deformations (Burgmann et al., 2000;

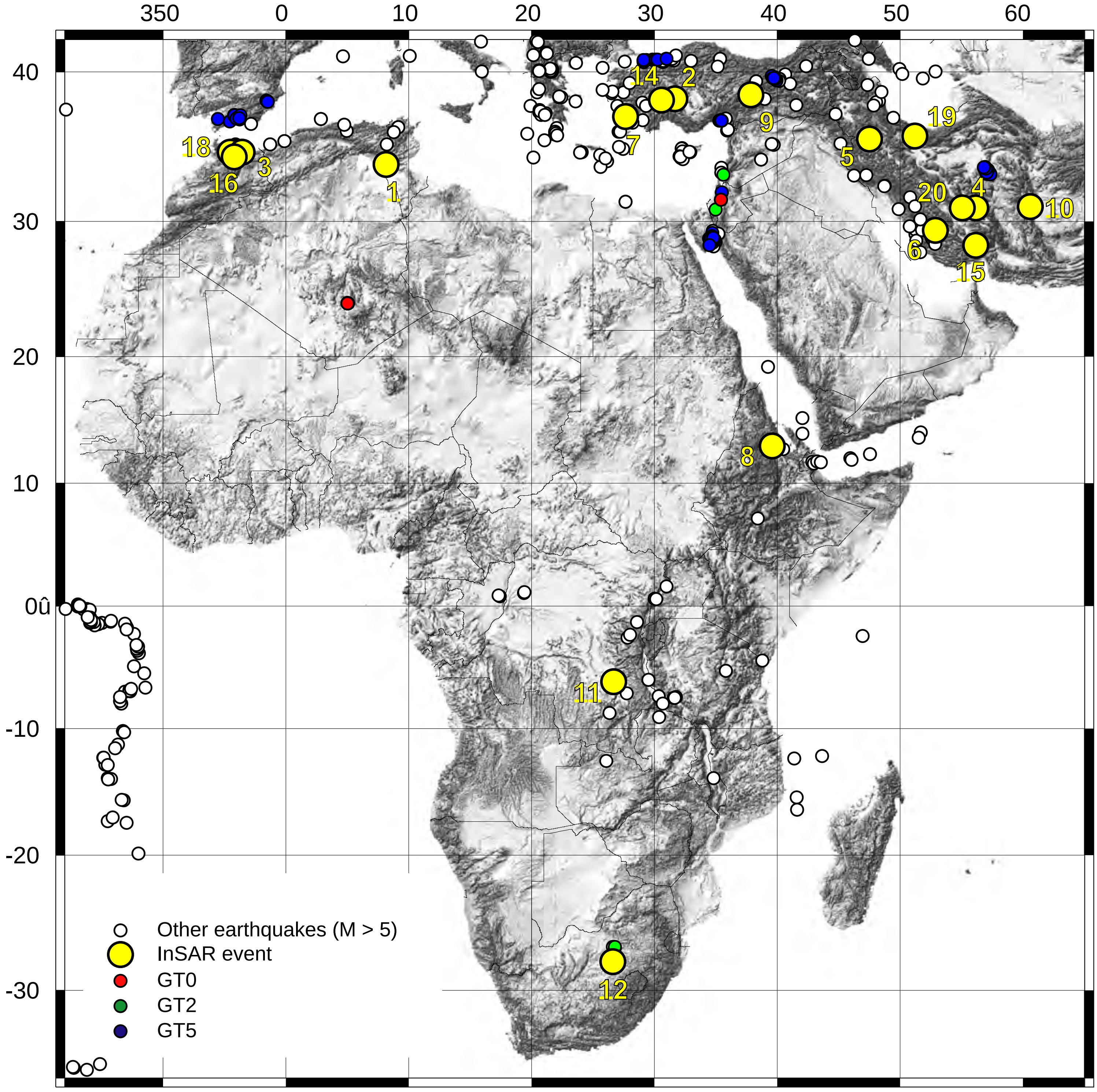

Figure 1. Location map of Africa, the Eastern Mediterranean, and Persian Gulf. Red, green, and blue circles indicate existing GT events. Yellow circles show InSAR events from this study. White circles show other earthquakes with magnitude greater than M 5.

Massonnet et al., 1993; Zebker et al., 1994). This is of particular interest to the nuclear monitoring community as InSAR has recently been shown to be capable of providing GT5 or better event locations (Begnaud et al., 2000a; Lohmann et al., 2002).

Generally, the use of InSAR for measuring earth surface deformation related to earthquakes involves phase-differencing of before and after radar images and removal of the topographic phase signal with a digital elevation model (which, itself, can be created using InSAR techniques) (Burgmann et al., 2000). InSAR only measures the change in range along the radar's line-of-sight (LOS) and so it is most sensitive to movement projected in these directions. For instance, for the same event, multiple InSAR-derived, LOS-projected deformation fields can be obtained from ascending, descending, or combined orbital paths. The general technique has been reviewed extensively by other authors (Burgmann et al., 2000; Rosen et al., 2000) and here we discuss only those features most pertinent to its use for remotely-sensed GT purposes.

Radar system design parameters that limit the detection of deformation signals by InSAR include the resolution of the radar image, the width of the imaging swath, measurement noise, and the wavelength of the radar signal (Massonnet and Feigl, 1998). For example, some deformation gradients associated with large, surface-rupturing earthquakes often exceed the 1/2 wavelength limit of displacement per pixel. This results in the loss of interferometric correlation. At the other extreme, and of concern to this proposed work, mm- to cm-scale displacements such as those from moderate earthquakes (as well as postseismic and interseismic deformation) can sometimes be overwhelmed by changes in atmospheric refraction (Zebker et al., 1997). Commonly, stacking techniques involving multiple interferograms help to mitigate atmospheric artifacts (e.g. Sandwell and Price, 1998; e.g. Sandwell and Sichoix, 2000); additionally, stochastic approaches based on calibration by GPS meteorology are a line of current active research (Foster et al., 2006; Williams et al., 1998).

Our ability to measure crustal deformation using InSAR is further limited by the degree of coherence between the radar signals backscattered from targets on the ground at the two times of imaging. If the ground comprising the radar footprint moves significantly, or if there are changes in the dielectric properties of the ground, then the radar signals will lack coherence. Interferometric coherence can vary temporally such as with seasons, (Lu and Freymueller, 1998; Wicks et al., 1998) and coherence is also affected by the relative positions of the SAR platform at the two acquisition times (i.e., the satellite baseline) (Zebker and Villasenor, 1992). In our study area we expected coherence conditions to be favorable because of the generally semi-arid to arid environments of North Africa, East Africa, and the eastern Mediterranean. These expectations are based on InSAR results from similar environments (e.g., eastern California) (Massonnet and K.L. Feigl, 1995), as well as our own work from northwestern Syria and Lebanon (Gomez et al., 2006).

For this study, we used the InSAR method to document small surface deformations from moderate to large earthquakes in Africa and the Middle East (Figure 1). Our InSAR processing strategy is standard with a small number of exceptions. Radar data from the European Space Agency's ERS and Envisat satellites were processed using the Gamma Remote Sensing suite of processing tools (Werner et al., 2000), and the topographic phase was removed using the available DEM data for the Middle East (usually SRTM, Shuttle Radar Topgraphic Mission, http://srtm.usgs.gov). We employed recently developed methods involving minimum-cost-flow algorithms weighted by interferometric coherence to better unwrap patchy interferograms (Chen and Zebker, 2000; Constantini, 1998).

2.2. Coseismic Geodetic Inverse Problem & Gibbs Sampling

Ground displacements from InSAR deformation maps can be used to invert for earthquake source parameters in a general class of problems called the coseismic geodetic inverse problem. This is written in the standard form, $\boldsymbol{Gm} = \boldsymbol{d}$ where $\boldsymbol{d}$ is a vector of the measured displacements, $\boldsymbol{m}$ is a vector of the source parameters to be inverted for, and $\boldsymbol{G}$ is a matrix of Green's functions which contain the physics relating the two. For a double-couple earthquake source, elastic dislocation Green's functions (Okada, 1985) are usually employed and $\boldsymbol{m}$ has 9 components describing the location, orientation and amount of slip for the dislocation. When auxiliary data exist, such as surface traces of coseismic ground rupture or dense seismologic networks, some of these parameters may be eliminated and the general problem can be formulated with fewer free parameters or even linearized allowing for the details of the earthquake slip distribution process to be investigated (Price and Burgmann, 2002).

For the smaller, more remote events which are the focus of this report, however, the full 9 parameter problem must be solved and so the method used to address this multidimensional, non-linear inverse problem becomes important. For instance, gradient-based methods are susceptible to getting stuck in local minima and so more advanced methods are necessary (Murray et al., 1996). Monte Carlo methods (Mosegaard and Sambridge, 2002) such as GS are particularly powerful tools for multidimensional non-linear inversion and this is the primary routine we will employ for our analysis of the North African seismic events. Although GS has been used in other geophysical problems (Basu and Frazer, 1990; Jaschke, 1997) it has not been explicitly applied to the coseismic geodetic problem to the best of our knowledge; thus the application of GS to this problem is, itself, a research focus of this proposal.

Gibbs sampling falls within a widely used class of Monte Carlo-based sampling algorithms (Mosegaard and Sambridge, 2002) of which Simulated Annealing (Basu and Frazer, 1990; Cervelli et al., 2001; Kirkpatrick et al., 1983; Metropolis et al., 1953; Rothman, 1985) is perhaps the best known. In contrast to Simulated Annealing which only attempts to find the peak of the multidimensional posterior distribution, $\sigma(m)$, GS actually samples from $\sigma(m)$. The collection of samples is then used to compute whatever marginal distributions or statistics are desired.

In particular, the Heat Bath algorithm (Creutz, 1980; Rebbi, 1984) employs GS to sample from the Gibbs-Boltzmann probability distribution, p_j, such that

$$p_j(\boldsymbol{m}) = \frac{\exp(-E_j / T)}{\sum_{j=1}^{N_s} \exp(-E_j / T)} \qquad (1)$$

where, as above, $\boldsymbol{m}$ is a vector of model parameters, E_j is the free energy of the j^{th} of N states, and T is temperature. We always set $E(m) = -\ln \sigma(\boldsymbol{m})$, so that when $T = 1$, eq. 1 will be sampling from $\sigma(\boldsymbol{m})$. For example, if $\sigma(\boldsymbol{m})$ is a Gaussian then, in the algorithm the misfit, $E(\boldsymbol{m})$, is the familiar squared residual $(\boldsymbol{d}\text{-}\boldsymbol{Gm})^T \boldsymbol{C}^{-1} (\boldsymbol{d}\text{-}\boldsymbol{Gm})$ where $\boldsymbol{C}$ is the data covariance matrix.

Ideally, to sample from an arbitrary $\sigma(m)$ one simply defines E in equation (1) by $E(m) = -\ln \sigma(m)$, then samples at $T = 1$. As the number of sweeps becomes infinite the system's equilibrium distribution becomes the Gibbs-Boltzmann distribution (Geman and Geman, 1984; Rothman, 1986) for T=1. In practice, before beginning to sample at $T = 1$, GS moves to the sampling temperature via a cooling schedule whose characteristics affect the performance of the associated inversion method (Rothman, 1985). If cooled too rapidly, the system will not be in equilibrium, and sampling will be biased, but cooling too slowly is computationally inefficient. (Statisticians who use Gibbs sampling refer to this period as the "burn-in time.") A common practice is to cool very slowly from a high temperature to T_*, the critical temperature at which a phase change occurs (Basu and Frazer, 1990). At T_*, low-E models are preferred, but the system is still warm enough for the sampler to escape from local energy minima. If $T_* < 1$, then sampling at T =1 can occur without danger of premature freezing; if, however, $T_* > 1$, then sampling at $T = 1$ is not possible and sampling at T_* gives samples from $(\sigma(\boldsymbol{m}))^{1/T_*}$ which is a much broader distribution than $\sigma(\boldsymbol{m})$. Because $\sigma(\boldsymbol{m})$ is typically multidimensional, correcting for this T-scaling is non-trivial and so it has been neglected in previous implementations of the method. Recently we have devised a way, using importance sampling (Press et al., 1992), to correct for the T-scaling and so provide an *a posteriori* correction for GS results (Brooks and Frazer, 2005b). Our development now allows GS routines to sample in an unbiased way from any arbitrary $\sigma(\boldsymbol{m})$, even if $T > 1$. For real data examples, where determining a unique T_* might be difficult, our experience motivates an approach in which we discard the notion of sampling at a single temperature and instead sample at various *sampling temperatures* T_s in parallel.

The power of the Gibbs Sampling approach for GT efforts is that the repeated sampling of parameter space allows for the construction of marginal posterior probability distributions (marginals) for each of the estimated parameters. This greatly facilitates the assessment of the resolution of important parameters such as hypocentral location and focal mechanism. Moreover, as stated above, although other authors have employed sampling-based Monte Carlo approaches to the coseismic geodetic inverse problem (e.g.Lohmann et al., 2002; Wright et al., 2004), the Gibbs Sampling approach is backed by theoretical work showing that as the number of sweeps becomes infinite the system's equilibrium distribution becomes the Gibbs-Boltzmann distribution for $T=1$ (Geman and Geman, 1984; Rothman, 1986). To the best of our knowledge, there is not similar theory backing the other methods and so the Gibbs Sampling approach removes much of the subjectivity associated with the inverse method itself in the coseismic geodetic inverse problem.

2.3 Project Team

These efforts were accomplished through a collaboration between the University of Hawaii (UH), the University of Missouri – Columbia (UMC), and Lawrence Livermore National Laboratory (LLNL).

UH personnel included Dr. Benjamin Brooks and Dr. Neil Frazer. Dr. Brooks served as the lead PI overseeing the execution of the entire project. Dr. Brooks and Dr. Frazer were primarily responsible for development and application of the Gibbs Sampling algorithm to determine GT event locations.

UMC personnel included Dr. Francisco Gomez and Dr. Eric Sandvol, as well two graduate students: Mr. Deepak Manjunath and Mr. Bao Xueyang . Dr. Gomez and Mr. Manjunath were responsible for all aspects of InSAR processing. Dr. Sandvol and Mr. Bao conducted the seismological tasks.

3. TECHNICAL APPROACH

3.1 SAR INTERFEROMETRY (INSAR)

The first task of this project involved imaging the surface deformation associated with moderate earthquakes using Synthetic Aperture Radar Interferometry (InSAR).

We have finalized the INSAR processing and successfully created displacement fields for 20 different earthquakes of magnitude less than 6.5. After the initial phases of the project and discussion with AFRL personnel, it became clear that there was high interest in determining if the technique would work for Mw 5.4 and smaller events and so we focused on these events in the latter portion of the project. Thus, of the 20 total candidate events for which interferograms were succesfully created, 8 were less than or equal to M_w 5.4, 12 were less than or equal to M_w 5.8, and 16 were less than or equal to M_w 6.0 (Figure 2).

3.1.1 Challenges

Our efforts to apply InSAR to document small surface deformation encountered several distinct challenges described below.

Uncertainty with Seismological Location.

Owing to the sparse seismic network coverage for many of the areas studied, the moderate-size earthquakes were originally reported based on regional and teleseismic arrival times. The resulting locations may typically have horizontal uncertainties of ± 40 km . Considering that a typical SAR image covers an area ~100 km wide, it was not uncommon to find that the earthquake was in an adjacent image track, rather than the one containing the location of the reported epicenter.

Data Availability.

Availabilty of appropriate data has been a challenge, particularly with the archived ERS data. It should be remembered that the ERS satellites were not developed with InSAR applications in mind. Furthermore, the ERS platforms had considerably less onboard storage than more recent platforms. The consequence of this is that, for many locations in the Middle East and Africa study area, little or no data were collected during 1992 – 2000. Furthermore, ERS data suitable for interferometry have been unavailable sine early 2001. This resulted from the failure of the navigational systems on the ERS 2 platform (ERS 1 was deceased by this time). Even in the cases when data were collected prior to 2001, satellite baselines were often inappropriate for InSAR. The orbits of the ERS satellites was maintained with a 2 km tube, which is not sufficiently strict to facilitate InSAR.

However, as discussed later, availability of appropriate data has improved (and will likely continue to improve) with the new generation of space-borne SAR platforms – many of these were designed with InSAR applications in mind. Specific for this effort, ESA’s Envisat has produced C-band SAR data suitable for interferometry since mid 2003. Over the timespan of this study, Envisat has acquired and archived a considerable volume of image data suitable for interferometry.

Inteferometric Decorrelation.

Temporal decorrelation of interferograms posed another challenge in all but the most arid of environments. The phase of the radar backscatter is the ensemble sum of all scatterers within the footprint of the radar echo. In all but the most arid and isolated regions, ground conditions (e.g., soil moisture, vegetation, etc.) will change seasonally, and even from year to year. These changes result in a loss of interferometric coherence over long time spans. This proved a challenge along coastal areas in the Mediterranean region, as well as in the interior of Africa. Interferometry in arid regions, such as Iran, maintains coherence over considerably longer time spans (e.g., 2 – 3 years). Hence, to mitigate problems with temporal decorrelation, ideally one would calculate itnerferograms for as short of a time span as possible that brackets the earthquake in time. Of course, this depends on the availability of appropriate data as discussed above.

Magnitude-Depth Limitations.

Another challenge pertains to the amount of surface deformation and the sensitivity of the SAR platform to deformation. The C-band (5.6 cm wavelength) radar systems used in this study are sensitive to changes in Line-of-Site distance of several millimeters (REF) (a full cycle of phase corresponds with 2.8 cm of range change). For unambiguous identification of an earthquake, at least ½ cycle of phase change (i.e., a total of ~1.4 cm) may be required. The surface deformation depends on earthquake size and depth of the earthquake – and these are not mutually exclusive. The deeper the earthquake, the wider the area of deformation, but the magnitude of surface deformation is reduced. Hence, InSAR is capable of detecting earthquakes of Mw ~5.0, but typically if they are shallow.

Atmospheric Phase Contribution.
Atmosphereic phase anomalies pose additional challenges to identifying small deformations. Differences in tropospheric moisture between the two scenes used to construct the interferogram can results in propogation path delays capable of contributing up to one to two cycles of interferometric phase. Hence, these can obscure the subtle signature of small surface deformations (where deformation results in 1 or fewer cycles). In some cases that we studied, atmospheric phase anomalies dominated the interferograms to such an extent that identifying the earthquake was not possible. In other cases, the earthquake could be distinguished as a smaller wavelength phase anomaly compared with the longer wavelengths typical of many atmospheric anomalies.

3.2 GIBBS SAMPLING INVERSION

For each interferogram created with for a candidate event, we followed the following procedure to perform the Gibbs Sampling inversion and yield our Ground Truth results for each event (described in section 4):

1) Because interferograms are only internally referenced and may contain a constant phase (or displacement) shift, we 'zero-meaned' or subtracted the mean displacement value from the whole inteferogram. In determining the mean we excluded displacement values associated with the earthquake itself, as those would bias the mean estimate.

2) We subsampled the area associated with the deformation (and a generous surrounding region as well) using a quadtree sampling algorithm (e.g.Jónsson et al., 2002). Often the quadtree algorithm would oversample in areas of high displacement gradient if its threshold was set too low and so we would usually augment by hand the intial suite of points determined with a higher threshold quadtree sampling. Typically sub-sampled data sets comprised between 100 and 200 displacement samples.

3) We determined the range of sampling temperatures (T_s) for the GS inversions by performing a series of 'short-runs' (Basu and Frazer, 1990; Brooks and Frazer, 2005a) as described above. Our forward model is the well-known 9 parameter dislocation in an elastic half space (Okada, 1985).

4) Using a range of T_s values from the short-runs we performed the full GS inversion. Based on our previous work (Brooks and Frazer, 2005a) the cooling schedules for our individual runs always comprised more than 100,000 samples resulting in over 20 million forward model evaluations. Every 10,000 samples we

plotted marginal distributions of the 9 parameters and evaluated convergence (through comparison with the previous intervals results).

5) We examined the marginals of each run at different T_s and chose the most well-behaved one for final presentation. As shown in Brooks and Frazer (2005), if T_s is too high then marginals will be too flat, essentially needing far many more samples to approach a realistic distribution. If T_s is too low, then sampling from local minima is more likely to occur, although the Heat Bath algorithm itself is particularly good at staying away from local minima.

3.3 SEISMOLOGICAL ANALYSES

3.3.1 Seismic Waveform Data Collection

We have continued to collected broadband waveforms for all of our GT10 or better events that we have determined the optimal hypocentral solutions. We have collected only broadband waveforms in order to be able to utilize the longer period energy (greater than 10 seconds) to obtain the optimal source parameters. We have also chosen to focus on local and regional seismic waveforms for this data analysis because these stations provide the best constraints on the hypocentral location parameters.

For the South Africa event we have found 7 regional broadband seismograms (InSAR event # 12). For the Sultan Dag (InSAR events # 2,14) and Tunisia (InSAR event #1) earthquakes we have found approximately 25 three component broadband seismograms with excellent signal to noise ratios within 30 degrees of the event. We have used the seismic waveforms in the Sultan Dag event to identify a small foreshock preceding the main shock by about 3 seconds.

In addition to these events we have collected seismic waveforms for sixteen InSAR events for which we have estimated hypocentral locations.

3.3.2 Origin Time Estimates using Seismic Data

We have finalized our techniques to either fix the hypocenter or epicenter and solver for the optimal origin/time or do a grid search for the depth. We are using LocSAT while constraining the hypocentral location and only allowing the origin time to vary. We have used a both a more and less restrictive phase data selection criteria. An example of one of these origin times determinations for the South Africa event (InSAR event # 12) is shown in Figure A1 (all of the seismological figures are found in Appendix A, see below).

We have also done a grid search over different depths and found, not at all surprisingly, an almost complete trade-off between origin time and the depth. Differences in the RMS fit are almost certainly insignificant (there is a small minima at the correct depth range however). However, since the South Africa earthquake has limited regional phase data available our solution for events in Turkey and Morocco tend to have smaller standard errors.

In Appendix A we have included the results of our phase data analysis and travel time inversions for all sixteen events. We observe some interesting patterns in the travel time residuals indicating some localized velocity variations near the source and possible misidentification of the first arrival. In general we observe the largest errors and broader residual distribution (see Appendix A) for those stations which have a smaller number of local phase data.

We note, however, that these analyses are dependent on the hypocentral estimates from the InSAR candidate events. As discussed below in section 4, some of these estimates are not in agreement with auxiliary data such as focal mechanisms and so should be considered accordingly.

3.3.3 Propagation of Errors in Origin Time Estimates

In order to determine the trade-off between origin time and the depth we propagated errors derived from marginal distributions for depth. We have propagated the errors by taking a two standard deviation based on the marginal distributions and conducted origin time inversions for two end member hypocentral solutions based solely on the geodetic solution. We have found in general that the origin times vary by slightly 0.1 second for every km in depth error. Most events had a 2 standard deviation of 2 km or less resulting in a smaller than 0.2 s error. It is important to note that this is larger than our standard estimates using just the phase data.

4. RESULTS

For each candidate event we present: a) the unwrapped phase from the interferogram; b) the line-of-sight displacement field; c) the marginal posterior distributions from the Gibbs Sampling (GS) inversion; and d) the focal mechanism for the event, usually from the Harvard CMT catalog (Figures 3-23).

Event 1: M_w 5.0, Tunisia (3/20/1997)
The event is detectable (Figure 3a). Maximum range-change values are ~ 3 cm and standard deviation of far-field noise is less than 5 mm, the smallest such value in our data set (Figure 2**)**. GS results yield well-constrained location and aspect ratio parameters which meet GT5 criteria (Figure 3c). Other parameters are well-constrained except for rake and strike marginal distributions which are bi-modal. The strike and dip marginals are consistent with the seismological focal mechanism (Figure 3c) although rake results suggest a more significant component of strike-slip than the seismological focal mechanism. Thus, it is likely that this event meets GT5 criteria.

Event 2: Mw 5.1,South Turkey-a (12/15/2000)

The event is detectable (Figure 4a), although some discontinuities in the near-field may indicate unwrapping errors. Additionally the NE-quadrant of the displacement field is not sampled due to decorrelation from a large lake. Maximum range-change values are ~ 3cm and standard deviation of far-field noise is close to 1 cm. The GS results suggest that GT5 criteria are met. Strike and dip marginals are bi- or tri-modal. The centroid location is to the south of the peak downward displacements by a few kilometers. This suggests a very shallow dipping fault in the opposite direction of the what could be expected in the region from the NW-dipping fault-bounded range front. Rake results suggest oblique slip, with a component of normal faulting. There is no seismological focal mechanism with which to compare results but, without other contrary information, it is likely that this event meets GT5 criteria.

Event 3: M_w 5.1, Morocco (12/4/2004)

The event is detectable (Figure 5a). Maximum range-change values are ~ 3 cm and standard deviation of far-field noise is ~5 mm (Figure 2). Most of the GS results are well-constrained, however the width marginal is very broad and strongly skewed towards values upwards of 30km (Figure 5c), as a result, the centroid is located significantly to the west of the displacement field.

The results suggest a very unlikely length/width aspect ratio of ~ ¼ for the slip patch. Moreover, the kinematics from the GS inversion strongly prefer a ~S-striking, right lateral nodal plane which is in the exact opposite sense of the seismological focal mechanism (Figure 5c).

We explore this discrepancy further by examining forward models of the displacements expected from the seismological focal mechanisms as well as from those favored by the GS inversion (Figure 6). The models from the N-S striking nodal plane of the CMT solution demonstrates the well-defined, 4-lobe pattern expected from a nearly vertical strike-slip fault (Figure 6a,b). For the E-W striking nodal plane, however, when this 4-lobed pattern is projected onto an InSAR line-of-sight (LOS) vector nearly parallel to the fault plane itself, a 2-lobed pattern results (Figure 6c,d). This is because the large horizontal motions contribue substantially more to the overall pattern when they are sub-parallel to the LOS. The relative LOS displacement values are too large, however, in comparison to the data set (Figure 6d). For the favored GS solution (Figure 6e,f), there is also a subdued 4-lobe pattern but it is stretched-out towards the west, and this suggests an explanation for the ‘un-geological’ GS results. Examination of the displacement field (Figure 5b) shows a wide area of positive range change values extending west of the co-seismic displacement field for greater than 30km. We also note that this event is one of two (the other is event 8) whose InSAR-estimated scalar moments are close to an order of magnitude greater than the seismological-estimated moment (Figure 24). It is possible that this over-estimated moment is caused by either an atmospheric artifact or the occurrence of post-seismic deformation. Thus, in order to yield GT5 results with confidence, then, mitigating steps must be taken such as stacking, or removal of the atmosphere via a weather model(Foster et al., 2006), and so this event does not currently meet GT5 criteria.

Event 4: M_w 5.2, North Iran-b (5/14/2005)

There is a deformation feature that is clearly detectable in the image (Figure 7a), although it is a subsidence feature and the event is a thrust fault (Figure 7c). The GS inversion yields well-constrained results for a normal fault (Figure 7c). Nonetheless the discrepancy between CMT and InSAR solutions is too large to permit consideration of this event for GT purposes.

Event 5: M_w 5.2, Northwest Iran (9/26/2005)

There are no clearly detectable events in this data set (Figure 8). In general, it is a noisy data set, with maximum range changes greater than 10cm. The CMT indicates a thrust mechanism and so we would expect a small, concentrated uplift field. There are too many potential such fields in the data set and so we cannot definitively choose one on which to perform the GS inversion to determine GT parameters.

Event 6: M_w 5.2, Iran (4/30/1999)

The event is detectable (Figure 9a). Maximum range-change values are ~ 5 cm and standard deviation of far-field noise is ~5 mm (Figure 2**)**. In a manner very similar to event 3 (Figure 5), most of the GS results are well-constrained, however the width marginal is very broad and strongly skewed towards values upwards of 30km (Figure 9c), as a result, the centroid is located significantly to the west of the displacement field. It is doubtful that the features to the west of the uplift field are related to the earthquake slip process itself, although we cannot rule out secondary subisdence features caused by earthquake shaking. More likely, the features are the result of atmospheric anomalies which have contaminated the GS inversion results. Without taking atmospheric mitigation steps this data set and its inversion do not satisfy GT5 criteria.

Event 7: M_w 5.3, Southwest Turkey (12/20/2004)

The event is detectable (Figure 10a). Maximum range-change values are ~ 3 cm and standard deviation of far-field noise is ~4 mm (Figure 2**)**. Upwards of 50% of the coseismic field, however, is not recorded due to decorrelation (Figure 10a). The GS results yield well-constrained GT5 location parameters; however the rake marginals strongly favor left-lateral strike-slip faulting, whereas the CMT indicates normal faulting. It is likely that this is due to the decorrelated region in the NE quadrant of the coseismic field (Figure 10b) which produced a non-unique displacement field. Given the discrepancy between the InSAR and CMT solutions, this event does not satisfy GT5 criteria.

Event 8: M_w 5.4, Eritrea (10/22/2004)

The event is detectable (Figure 11a). Maximum range-change values are ~ 15 cm and standard deviation of far-field noise is ~1.5 cm (Figure 2). The GS inversion yields well-constrained parameters, however, the favored strike of ~060 and left-lateral mechanism are in disagreement with the Harvard CMT (Figure 11c) as well as with the published mechanism of (Hagos et al., 2006). We note, however, that this event is also one of two (the other is event 3) whose InSAR-estimated scalar moments are close to an order of magnitude greater than the seismological-estimated moment (Figure 24). It is possible that this over-estimated moment is caused by either an atmospheric artifact or the occurrence of post-seismic deformation. Thus, in order to yield GT5 results with confidence, then, mitigating steps must be taken such as stacking, or removal of the atmosphere via a weather model(Foster et al., 2006), and so this event does not currently meet GT5 criteria.

Event 9: M_w 5.6, East Turkey (8/11/2004)
The event is detectable (Figure 12a). Maximum range-change value is ~ 4 cm and standard deviation of far-field noise is ~8.6 mm (Figure 2). In the eastern portion of the displacement field there is a wedge-shaped discontinuity that is likely due to an uwrapping error. In general, parameters are well-constrained well-enough for GT5 critieria but the rake and dip marginal marginals indicate low-angle thrust faulting whereas the CMT is strike-slip. It is probable that the discrepancy between the InSAR and CMT solutions is due to the displacement field being contaminated by unwrapping errors and accordingly this event does not currently satisfy GT5 criteria.

Event 10: M_w 5.7, Iran (4/10/1998)
The event is detectable (Figure 13a). Maximum range-change value is ~ 4 cm and standard deviation of far-field noise is ~4.7 mm (Figure 2). GT parameters are, in general, well-constrained though the strike marginal is bi-modal and rake is slightly bi-modal with a principal mode favoring a thrust mechanism. Although most parameters are consistent with the CMT, the thrust mechanism is not consistent with the CMT which is strike-slip. Accordingly, our conclusion is that GT5 criteria cannot be verified because of the inconsistency between the InSAR and CMT solutions.

Event 11: M_w 5.7, Zaire (12/11/1995)
There are no clearly detectable events in this data set that can be unequivocally associated with the seismic event (Figure 14). The CMT indicates an oblique normal mechanism and so we would expect a small, concentrated susbidence field. Maximum range change values are ~ 4cm. Due to atmospheric noise, there are too many potential such fields in the data set and so we cannot definitively choose one on which to perform the GS inversion to determine GT parameters.

Event 12: M_w 5.7, South Africa (4/22/1999)
The event is detectable (Figure 15). Maximum range-change value is ~ 2 cm and standard deviation of far-field noise is ~4 mm (Figure 2). GT parameters are generally well-constrained although width is inordinately large, with values tending towards greater than 30km. This displacement field was associated with a well-known mine collapse (Doyle et al., 2001) in Welkom, South Africa, and so it is likely that the source was not a well-defined double-couple. Moreover, there is no CMT available for the event. The inordinately large width values associated with an otherwise well-behaved displacement field suggest that the event is not well-modeled by a double-couple. In addition, because of the lack of a CMT with which to compare solutions, this event does not currently satisfy GT5 criteria.

Event 13: M_w 6.0, Tibet-a (3/27/2004)
The event is detectable (Figure 16). Maximum range-change value is ~ 10 cm and standard deviation of far-field noise is ~1.5 cm (Figure 2). The GS inversion yields well-constrained parameters which are consistent with the CMT (Figure 16c). The length marginal marginal has a peak at ~17km, however. Thus, due to the aspect ratio of the slip patch, the uncertainty on the event's source is larger than the ± 5km length scales for GT5 determination and so this event does not satisfy GT5 criteria.

Event 14: M_w 6.0, South Turkey-b (12/15/2000)
The event is detectable (Figure 17). This is the larger (and later) of the two events that occurred on this day. (The first event is our event 2 (Figure 4)). Maximum range-change value is ~ 6 cm and standard deviation of far-field noise is ~8.5 mm (Figure 2). The GS inversion yields well-constrained parameters which are consistent with the CMT and favor the the NE-dipping nodal plane (Figure 17c). The length marginal marginal has a peak at ~25 km, however. Thus, due to the aspect ratio of the slip patch, the uncertainty on the event's source is larger than the ± 5km length scales for GT5 determination and so this event does not satisfy GT5 criteria.

Event 15: M_w 6.0, South Iran (11/27/2005)
The event is detectable (Figure 18). Maximum range-change value is ~ 12 cm and standard deviation of far-field noise is ~1.2 cm (Figure 2). The GS inversion yields well-constrained parameters which are consistent with the CMT, though rake in the InSAR solution is slightly more oblique than the pure thrust CMT (Figure 18c). The length marginal marginal has a peak at ~9km, which is close to the ± 5km length scales for GT5 determination. When the distributions of other parameters, however, such as length and location are considered this event does not satisfy GT5 criteria.

Event 16: M_w 6.0, Morocco (5/31/1994)
The event is detectable (Figure 19), though the InSAR displacement field is very patchy and partial due to large regions of decorrelation. Maximum range-change value is ~ 4 cm and standard deviation of far-field noise is ~3.9 mm (Figure 2). The GS inversion yields some well-constrained parameters, but favored rake values suggests the opposite sense of shear compared with the CMT focal mechanism, and the dips are too shallow. It is probable that this is due to the partial nature of the displacement field, as many of our InSAR solutions for similar magnitude events (i.e. events 13-15) are consistent with CMT focal mechanisms. This event has also been studied in detail by others (Akoglu et al., 2006; Biggs et al., 2006) and it already exists in the GT catalog from the seismological study of Calvert et al. (1997). Given these other studies, and the likliehood that the event's size would preclude it from GT5 consideration we do not pursue it further for GT5 purposes.

Event 17: M_w 6.2, Tibet-b (7/11/2004)
The event is detectable (Figure 20). Maximum range-change value is ~ 12 cm and standard deviation of far-field noise is ~1.2 cm (Figure 2). The GS inversion yields well-constrained parameters which are consistent with the CMT (Figure 17c). Both the length and width marginals exhibit spreads from ~3 to 13km with peaks at at ~3 and 6.5 km,

respectively. The centroidal depth has a peak value at ~ 9km. Thus, a large portion of the possible solutions for this event fall within GT5 criteria, though there are also a significant number of solutions which exceed GT5 criteria.

Event 18: M_w 6.3, Morocco (2/24/2004)
The event is detectable (Figure 21). Maximum range-change value is ~ 15 cm and standard deviation of far-field noise is ~2.5 cm (Figure 2). The GS inversion has some well-constrained parameters though rake and strike are bi-modal and the shallow dips yield significant inconsistency with the CMT focal mechanism. In a manner similar to Event 17, however, length, width and depth parameters permit a substantial number of solutions which meet GT5 criteria.

Event 19: M_w 6.3, Iran (5/28/2004)
The event is detectable (Figure 22). Maximum range-change value is ~ 5 cm and standard deviation of far-field noise is ~1 cm (Figure 2). The GS inversion yields well-constrained parameters which are consistent with the CMT, though strike is bimodal (Figure 22c). The length and width marginal marginals are skew symmetric with peaks at ~2-3km and long tails reaching values greater than 20 km. The centroidal depth marginal marginal has a peak at ~17 km and tails reaching from ~10 to 24 km. Thus, a large portion of the possible solutions for this event fall within GT5 criteria, though there are also a significant number of solutions which exceed GT5 criteria.

Event 20: M_w 6.4, North Iran-a (2/22/2005)
The event is detectable (Figure 23). Maximum range-change value is ~ 20 cm and standard deviation of far-field noise is ~1.9 cm (Figure 2). The maximum displacement of the event itself is missing, owing to decorrelation (Figure 23a,b). The GS inversion yields mostly well-constrained parameters though they are not all consistent with the CMT (Figure 23c) – particularly strike and rake, which implies strike-slip faulting though the CMT is a thrust mechanism. It is most likely that the lack of a complete displacement field creates nonuniqueness in the solution and explains the inconsistency with the focal mechanism. Moreover, the length and width paramters, while well-constrained would combine to yield aspect ratios greater than 10x10 km and so this event would not meet GT5 criteria.

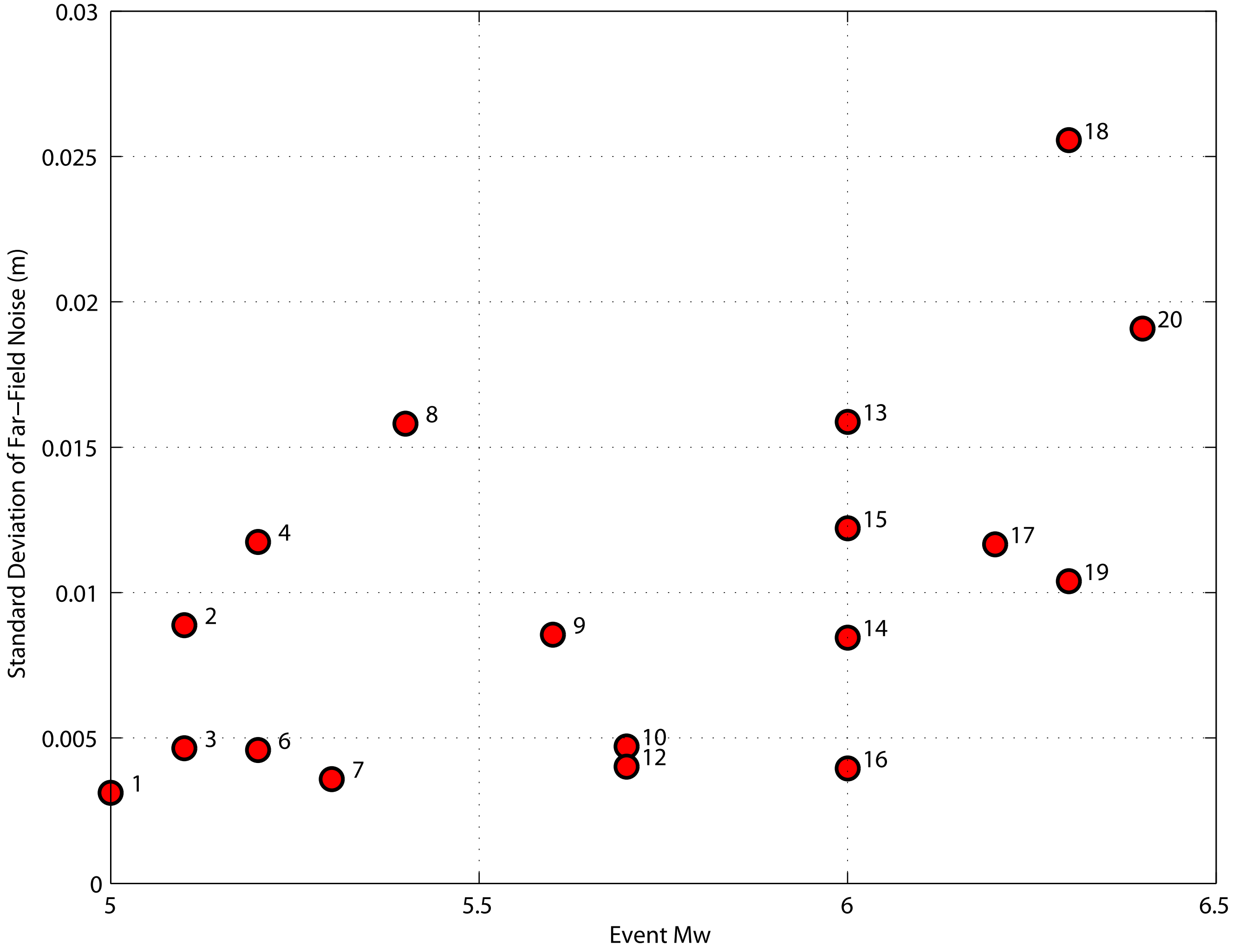

Figure 2. Far-field noise values and Mw from the studied events. Event ID numbers are indicated.

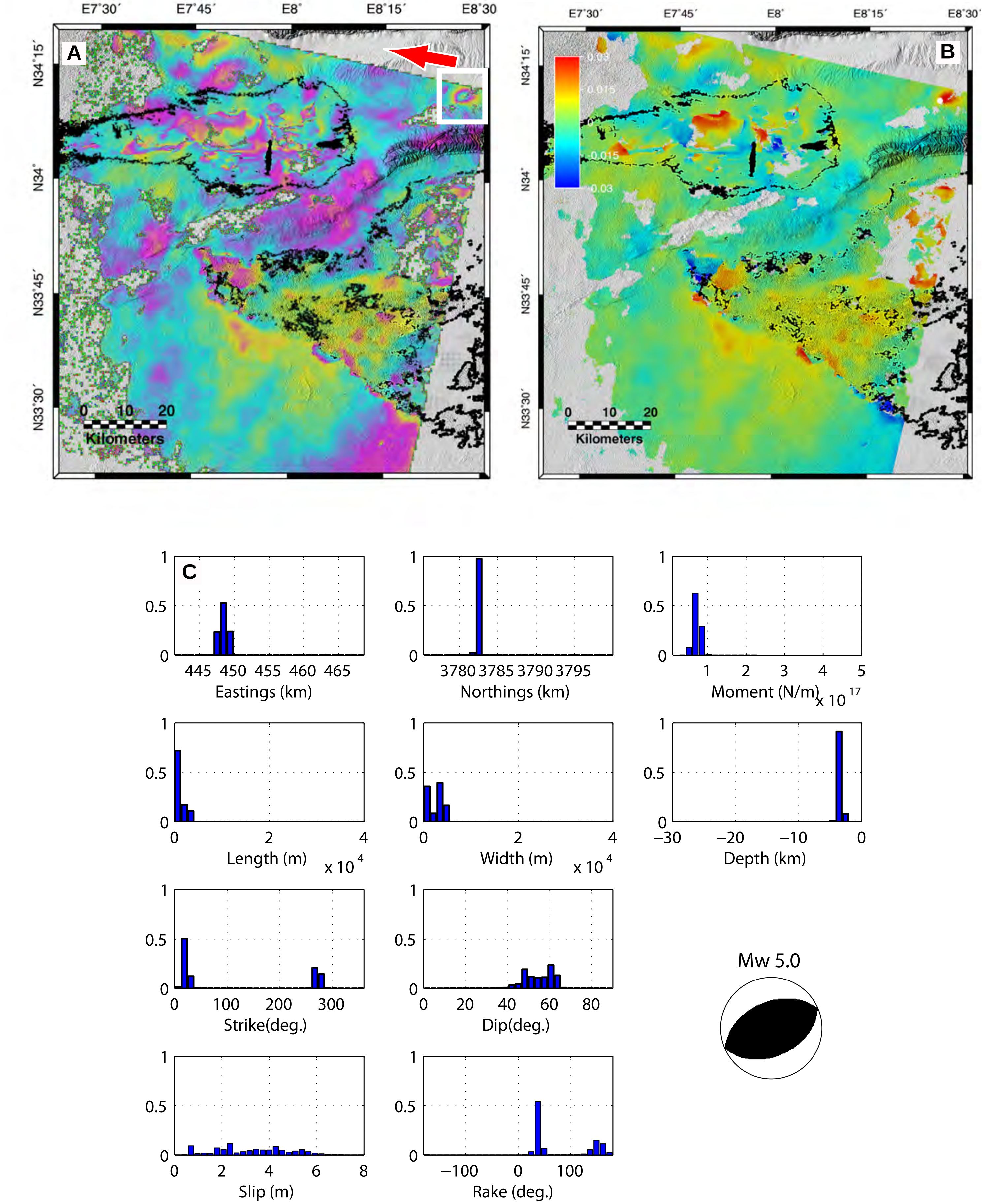

Figure 3. Event 1: 3/20/97, Tunisia. Descending satellite view. A. Unwrapped interferometric phase (1 color cycle = 2 pi). B. Line-of-sight displacement field. Red Arrow indicates the look-direction of the satellite. White dot indicates epicenter location of the favored model.C. Gibbs Sampling inversion results with Ts = 5 and 180,000 iterations and ISC focal mechanism.

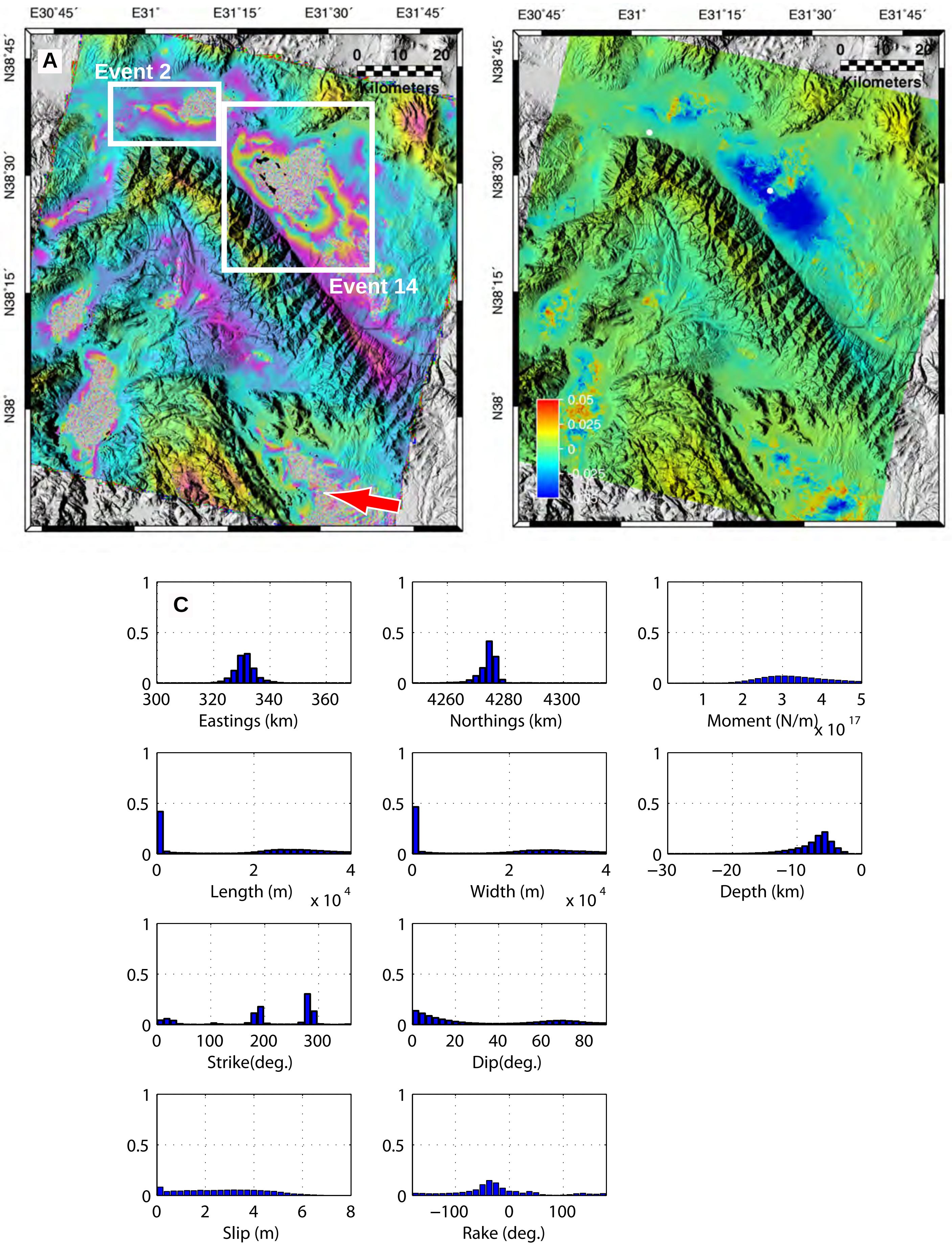

Figure 4. Event 2: 12/15/2000, Turkey. Descending satellite view. A. Unwrapped interferometric phase (1 color cycle = 2 pi). B. Line-of-sight displacement field. Red Arrow indicates the look-direction of the satellite. White dot indicates epicenter location of favored model. Gibbs Sampling inversion results with Ts = 1 and 100,000 iterations.

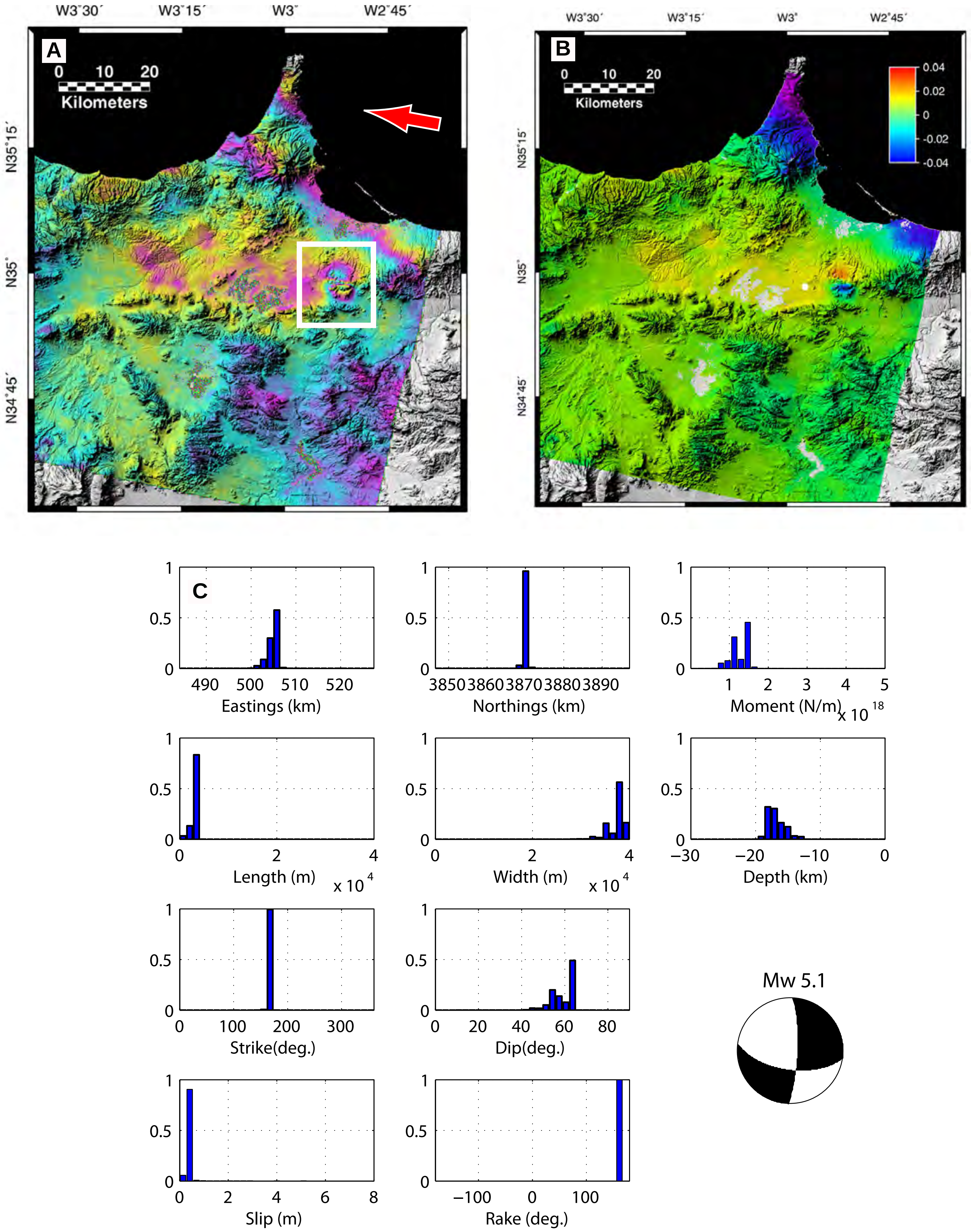

Figure 5. Event 3: 23/4/04, Morocco. A. Unwrapped interferometric phase (1 color cycle = 2 pi). B. Line-of-sight displacement field. Red Arrow indicates the look-direction of the satellite. White dot indicates epicenter location of the favored model. C. Gibbs Sampling inversion results with Ts = 3 and 200,000 iterations and Harvard CMT.

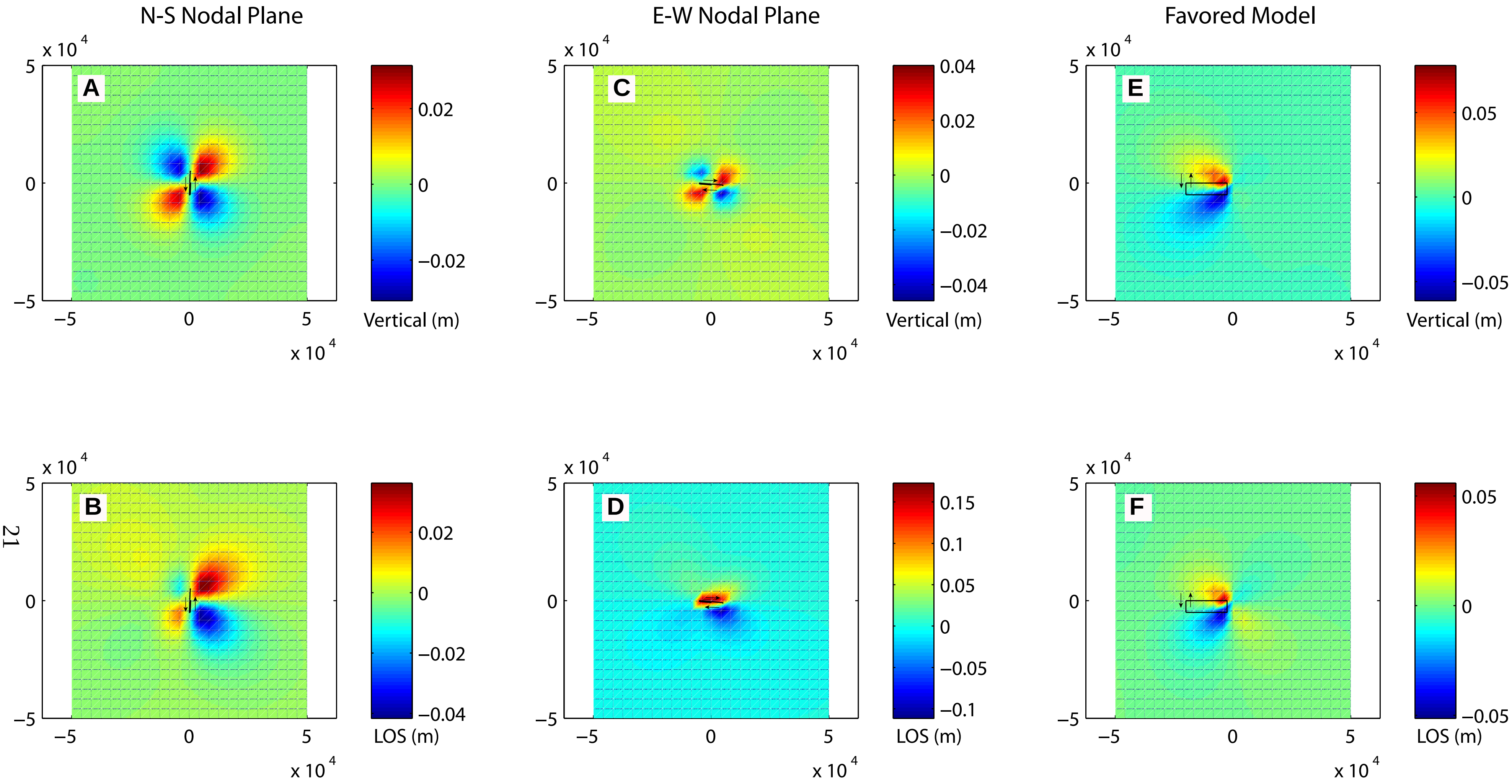

Figure 6. Forward models associated with candidate solutions (NS nodal plane, EW nodal plane, and the Favored Model) for Event 3 displacement fields. A,C,E: vertical displacements; B,D,F: total displacements projected onto descending line of sight (LOS). In each figure the fault plane trace and sense of slip is indicated.

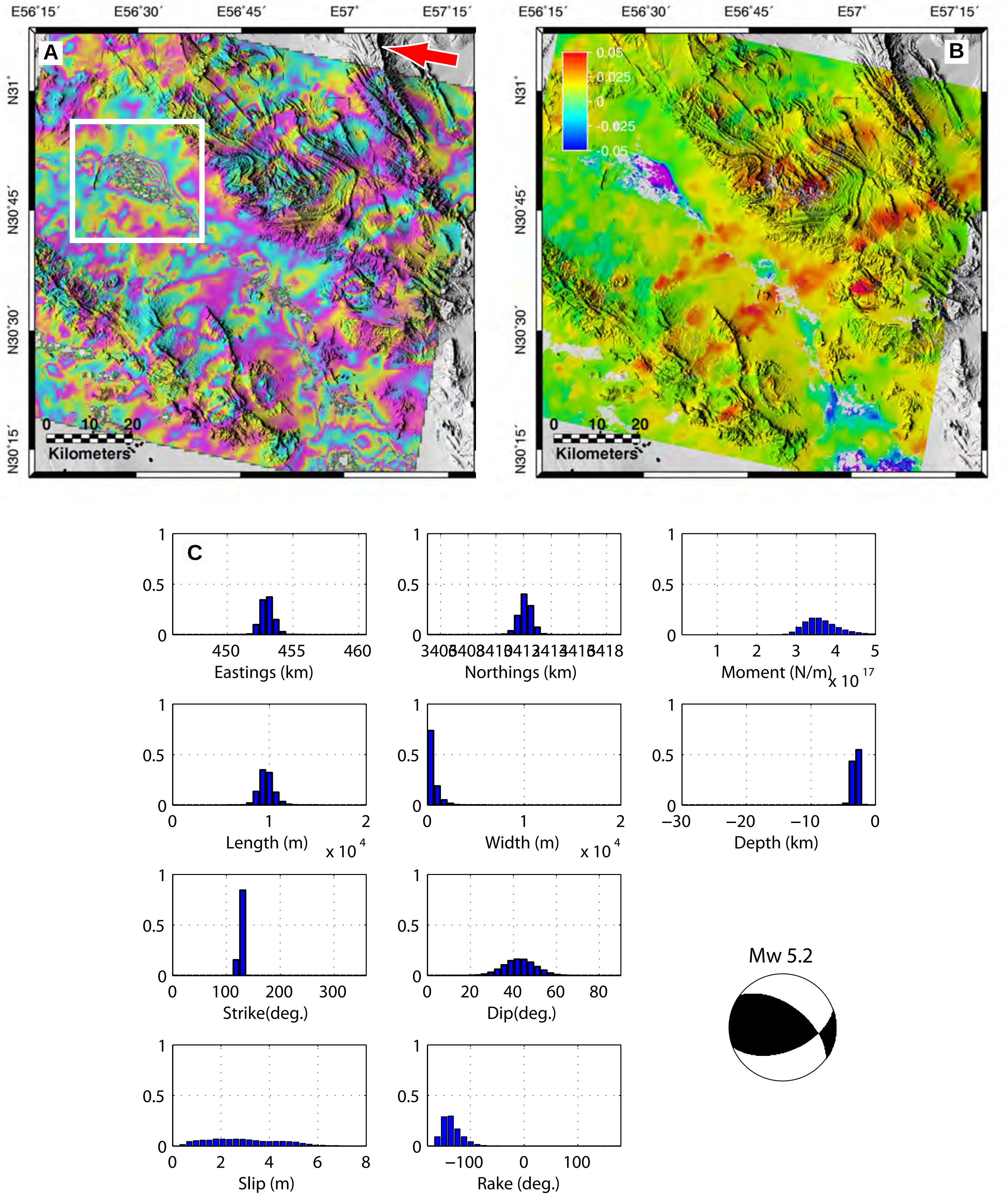

Figure 7. Event 4: 5/14/05, Iran. Descending satellite view. A. Unwrapped interferometric phase (1 color cycle = 2 pi). B. Line-of-sight displacement field. Red Arrow indicates the look-direction of the satellite. C. Gibbs Sampling inversion results with Ts =1 and 100,000 iterations and Harvard CMT .

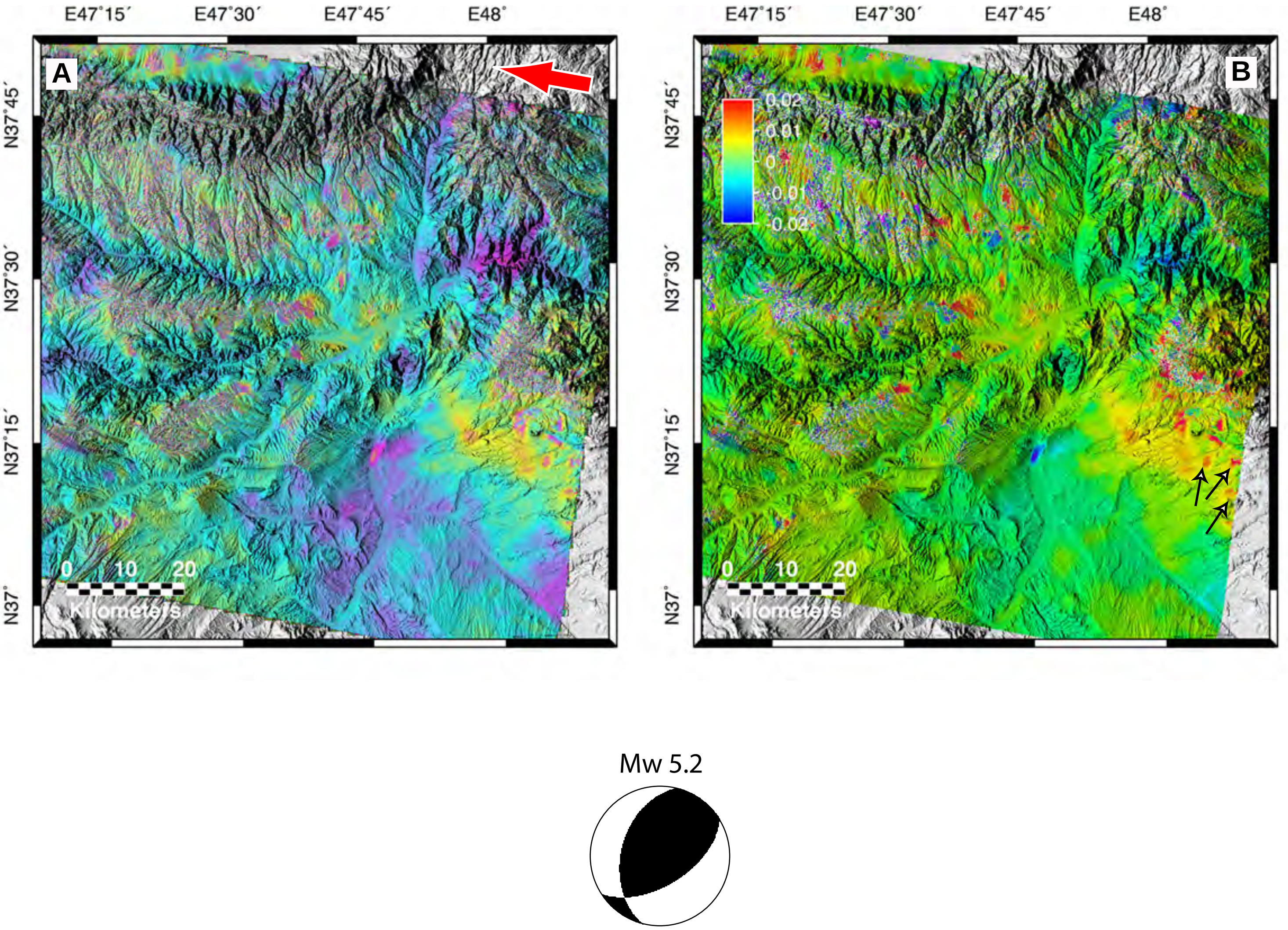

Figure 8. Event 5: 9/26/05, Iran. Descending satellite view. A. Unwrapped interferometric phase (1 color cycle = 2 pi). B. Line-of-sight displacement field. Red Arrow indicates the look-direction of the satellite. White arrows indicate potential small uplift fields that could be associated with the earthquake. Harvard CMT.

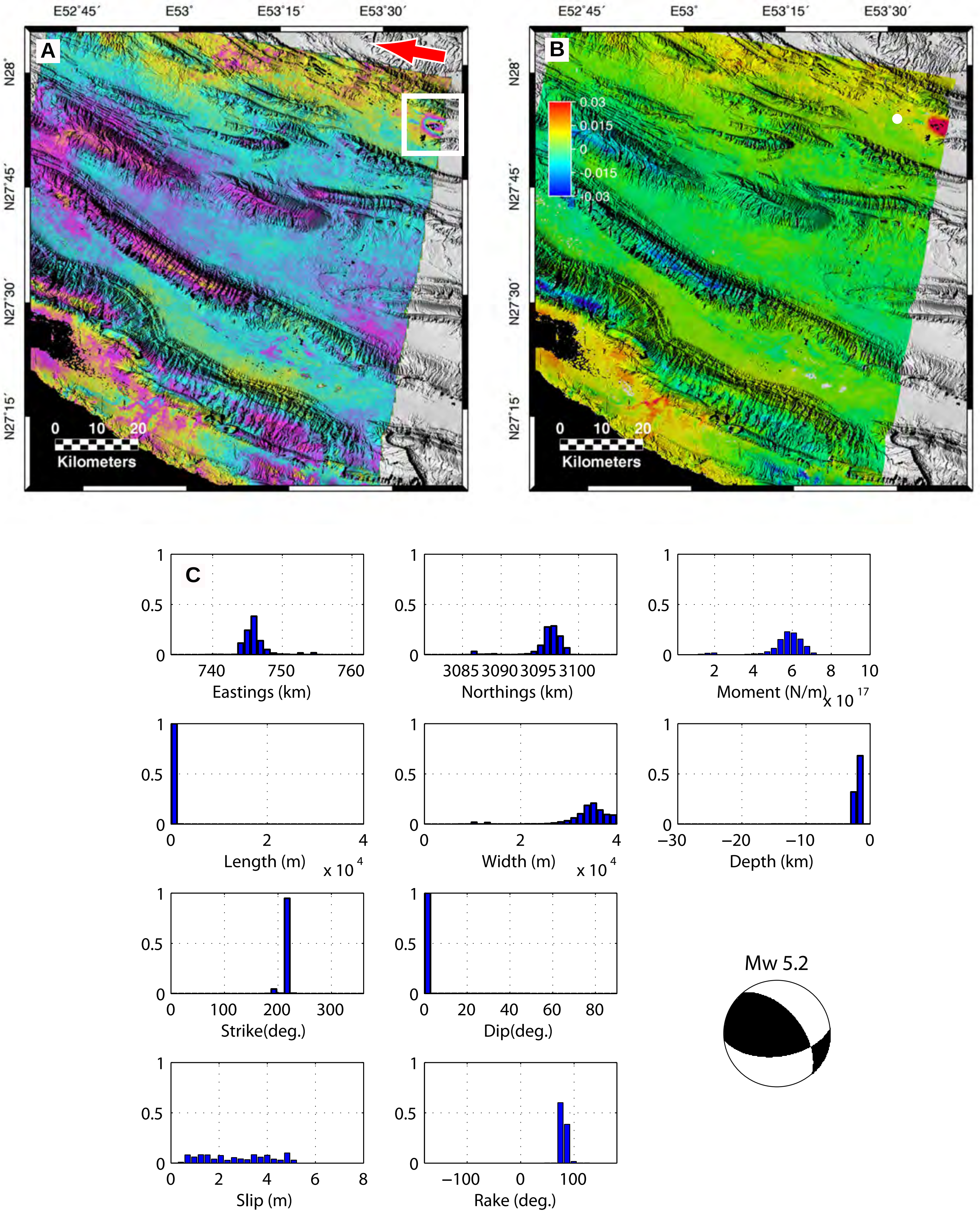

Figure 9. Event 6: 4/30/99, Iran. Descending satellite view. A. Unwrapped interferometric phase (1 color cycle = 2 pi). B. Line-of-sight displacement field. Red Arrow indicates the look-direction of the satellite. White dot indicates epicenter location of favored model. C. Gibbs Sampling inversion results with Ts = 4 and 200,000 iterations and

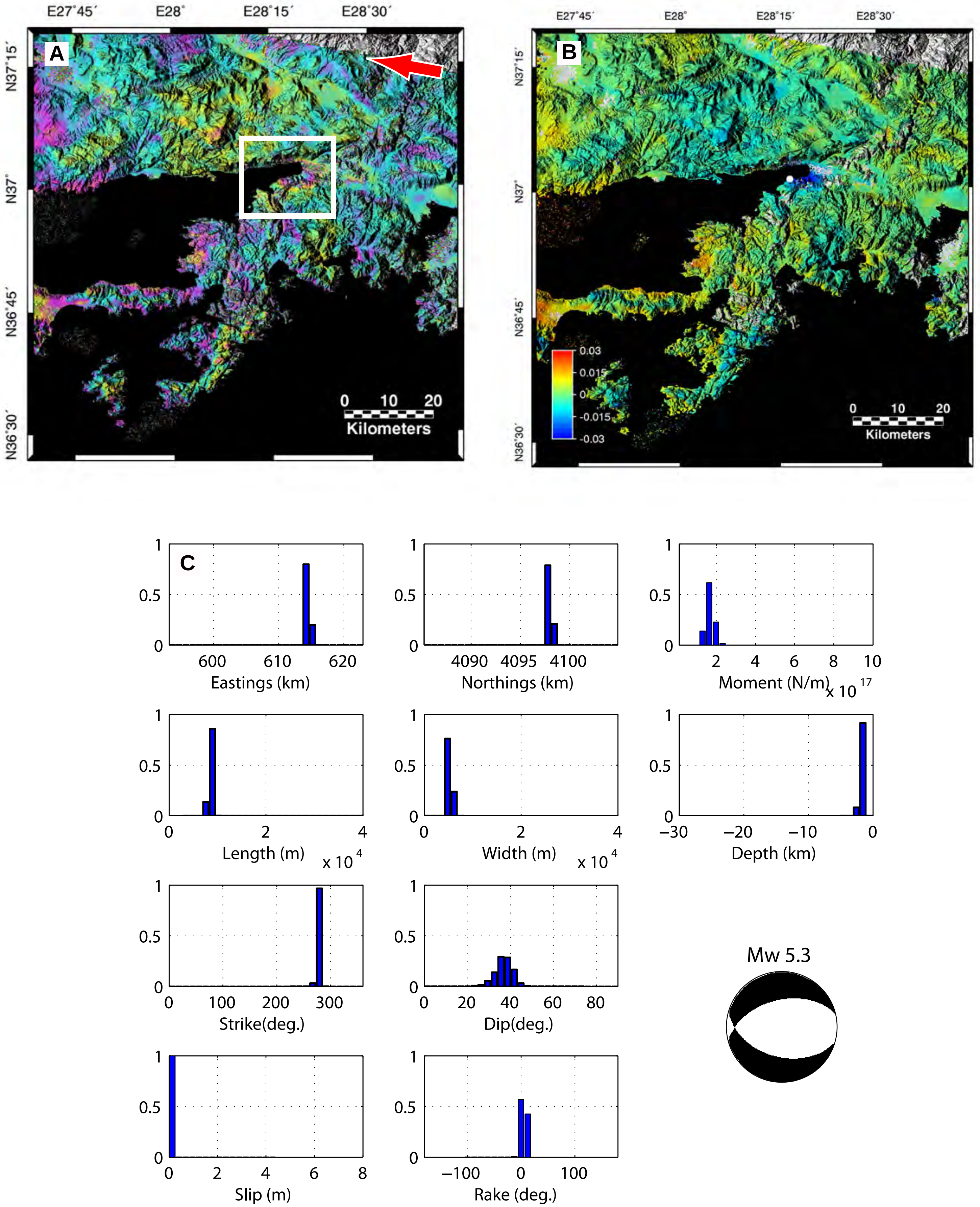

Figure 10. Event 7: 12/20/04, Turkey. Descending satellite view. A. Unwrapped interferometric phase (1 color cycle = 2 pi). B. Line-of-sight displacement field. Red Arrow indicates the look-direction of the satellite. White dot indicates favored epicenter. C. Gibbs Sampling inversion results with Ts =1 and 200,000 iterations and Harvard CMT.

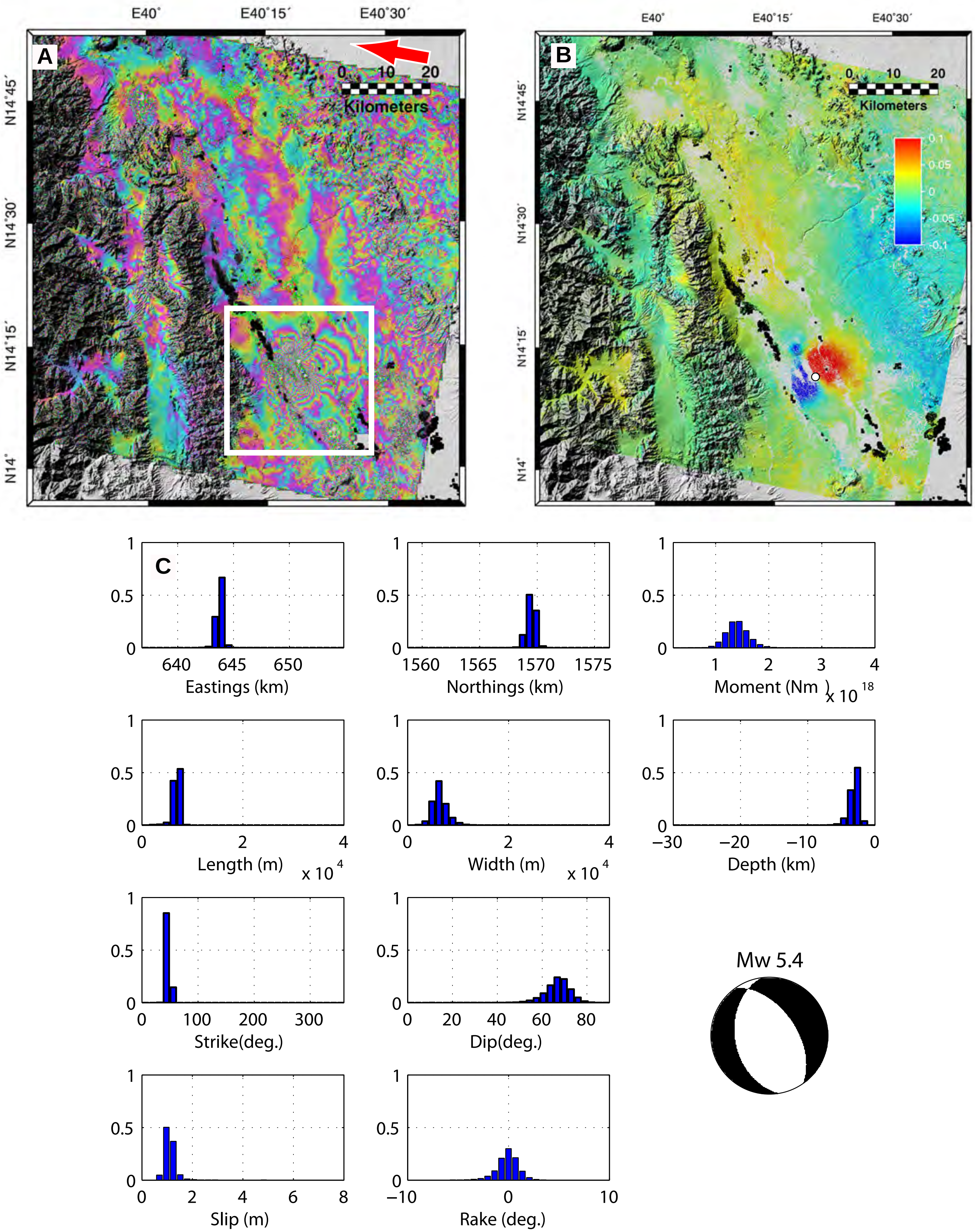

Figure 11. Event 8: 10/22/2004, Eritrea. Descending satellite view. A. Unwrapped interferometric phase (1 color cycle = 2 pi). B. Line-of-sight displacement field. Red Arrow indicates the look-direction of the satellite. White dot indicates epicenter location of favored model. C. Gibbs Sampling inversion results with Ts = 1 and 200,000 iterations.

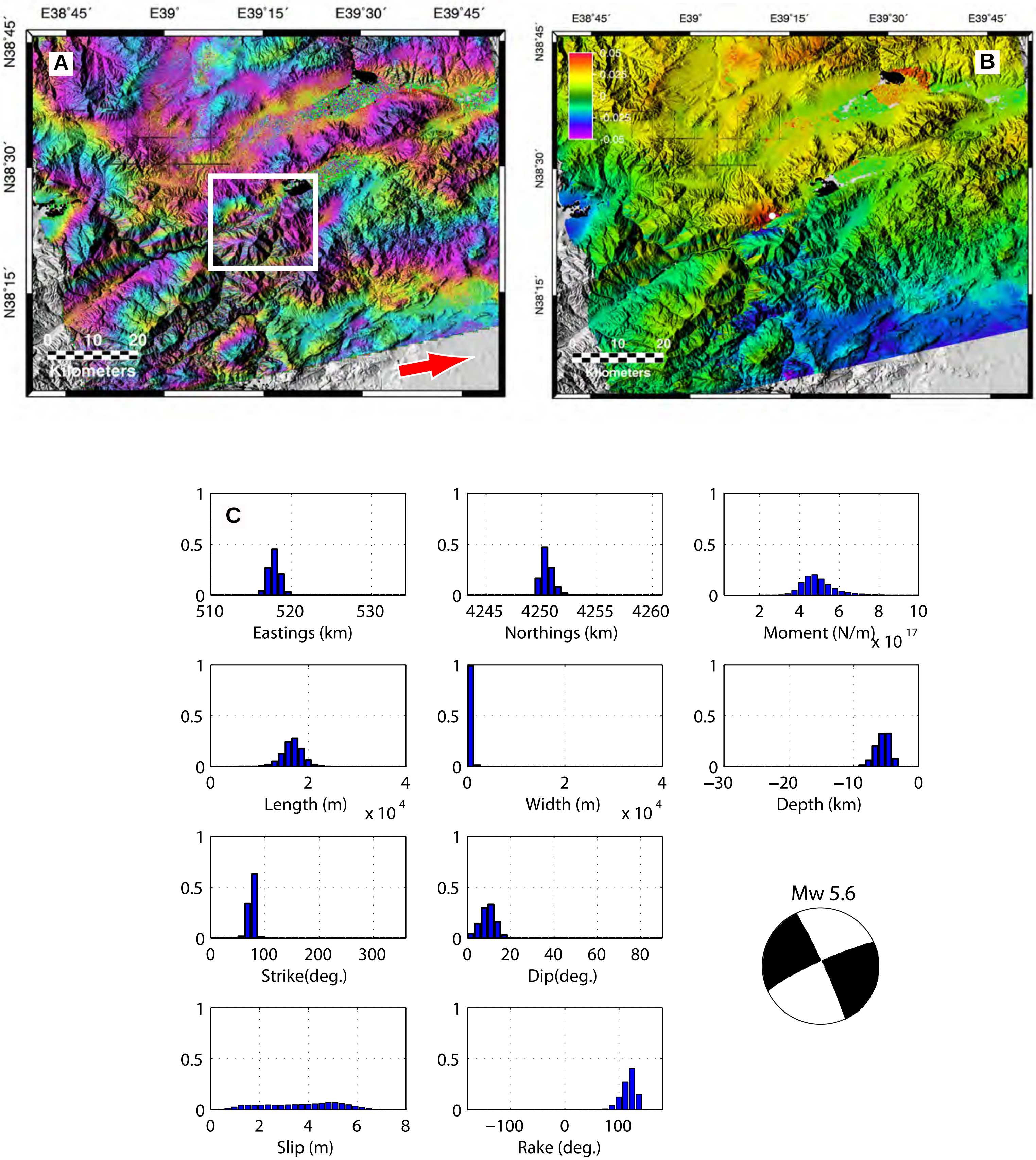

Figure 12. Event 9: 8/11/04, Turkey. Ascending satellite view. A. Unwrapped interferometric phase (1 color cycle = 2 pi). B. Line-of-sight displacement field. Red Arrow indicates the look-direction of the satellite. White dot indicates epicenter of favored model C. Gibbs Sampling inversion results with Ts =1, 190,000 iterations and Harvard

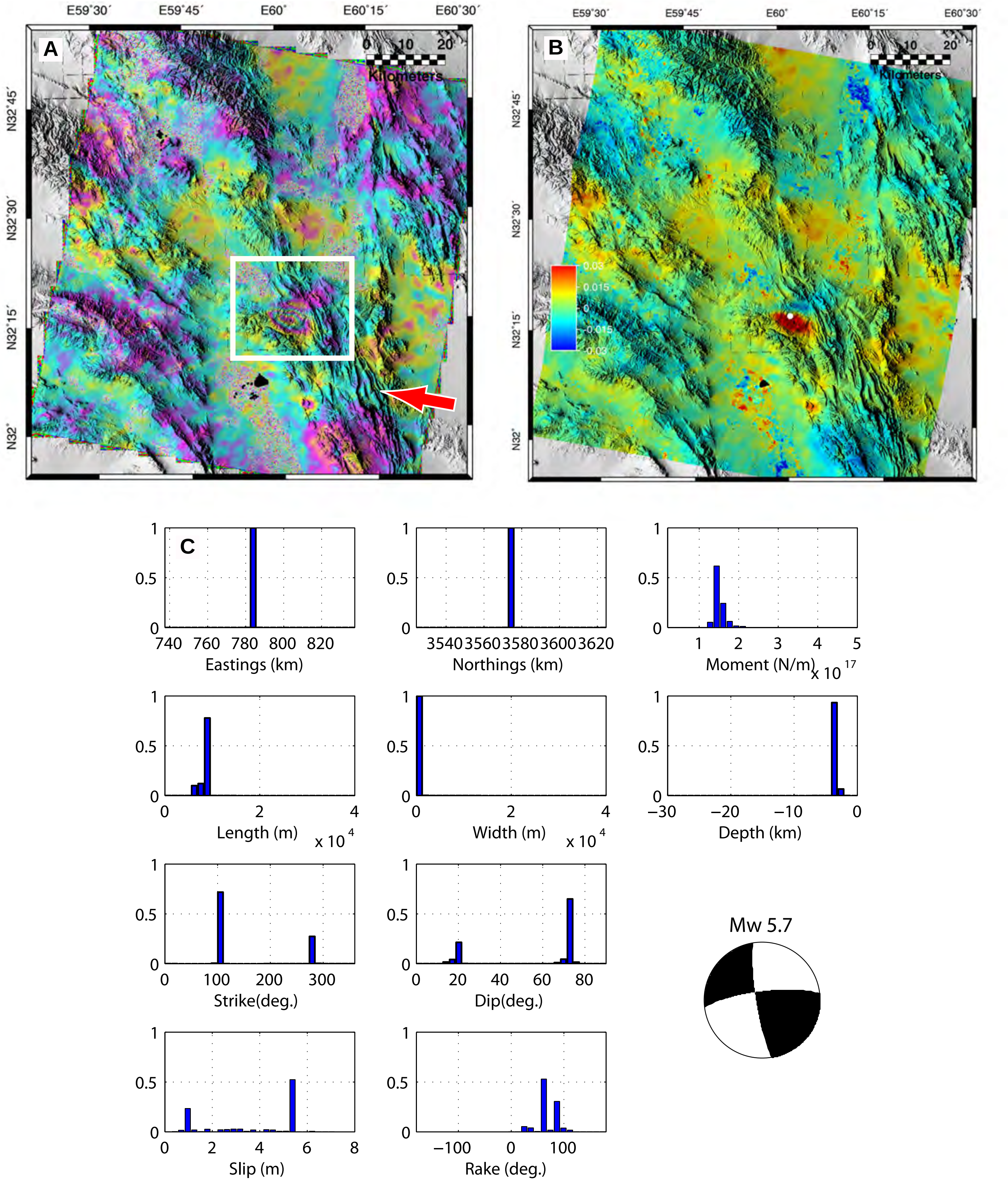

Figure 13. Event 10: 4/10/98, Iran. Descending satellite view. A. Unwrapped interferometric phase (1 color cycle = 2 pi). B. Line-of-sight displacement field. Red Arrow indicates the look-direction of the satellite. White dot indicates the epicenter location of the favored model C. Gibbs Sampling Results with Ts = 10; 390,000 iterations and

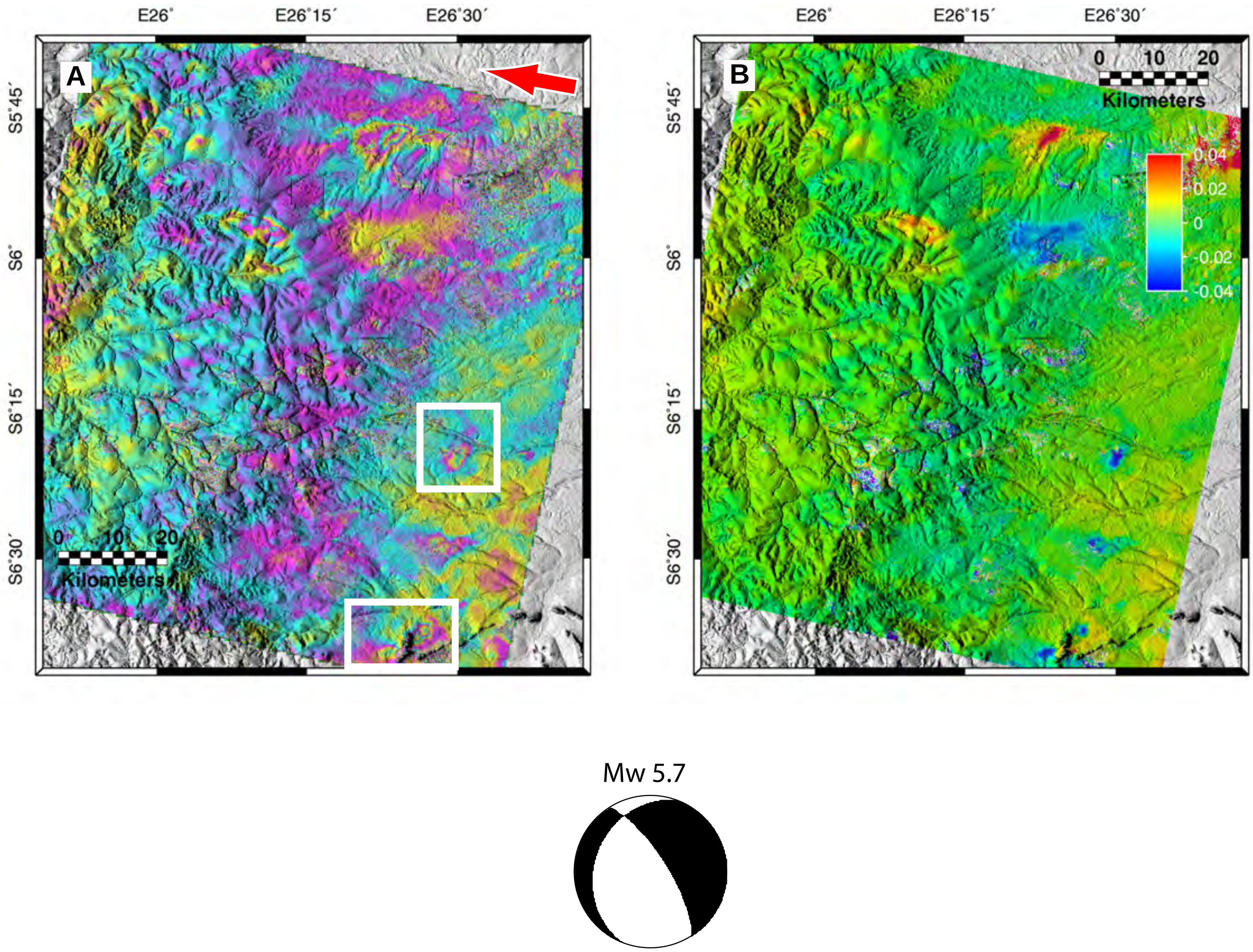

Figure 14. Event 11: 12/11/95, Zaire (Rep. of Congo). Descending satellite view. A. Unwrapped interferometric phase (1 color cycle = 2 pi). B. Line-of-sight displacement field. Red Arrow indicates the look-direction of the satellite. Harvard CMT. White boxes in A contain possible subsidence fields associated with the normal faulting event.

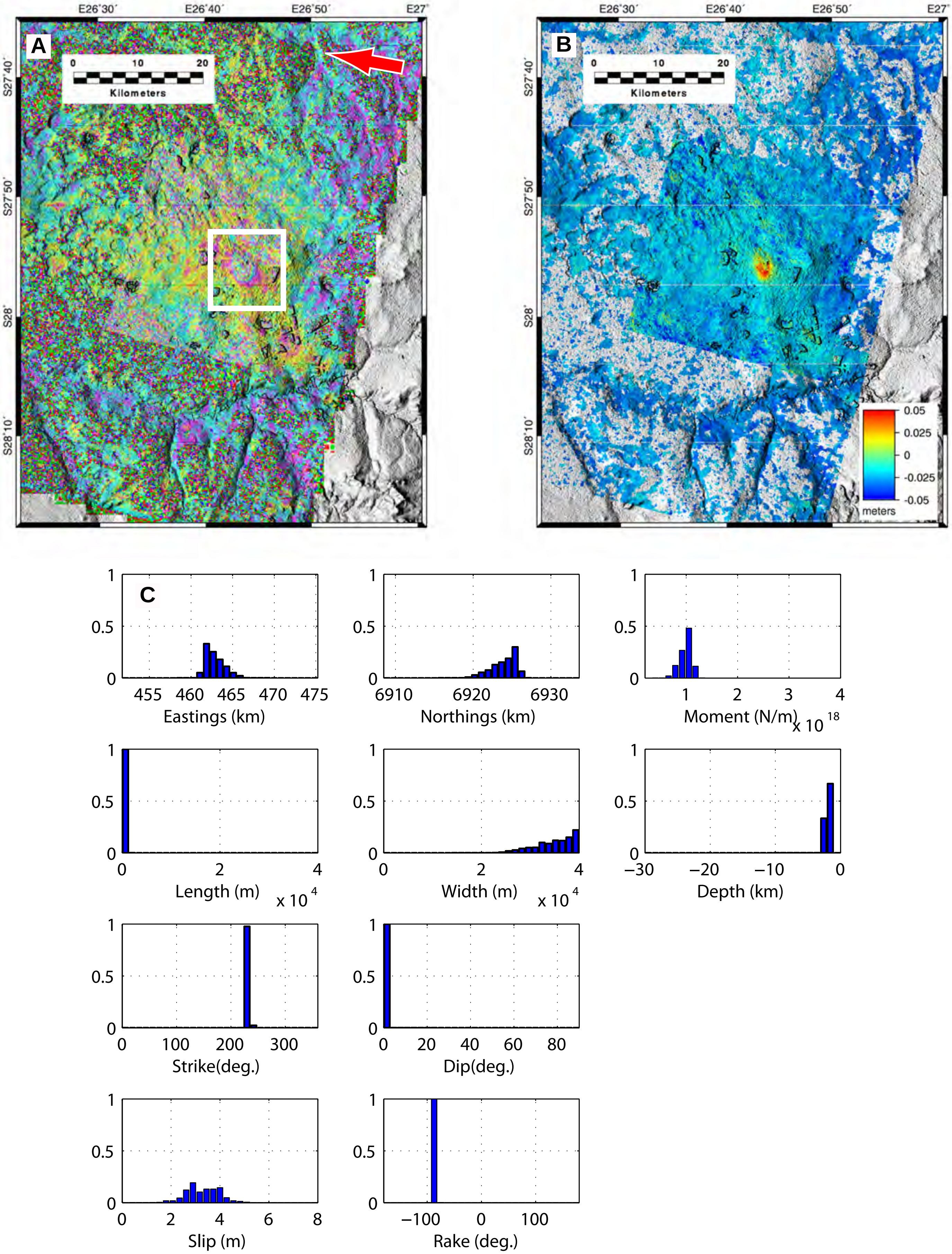

Figure 15. Event 12: 4/22/99, South Africa. Descending satellite view. A. Unwrapped interferometric phase (1 color cycle = 2 pi). B. Line-of-sight displacement field. Red Arrow indicates the look-direction of the satellite. C. Gibbs Sampling Results with Ts = 5; 180,000 iterations.

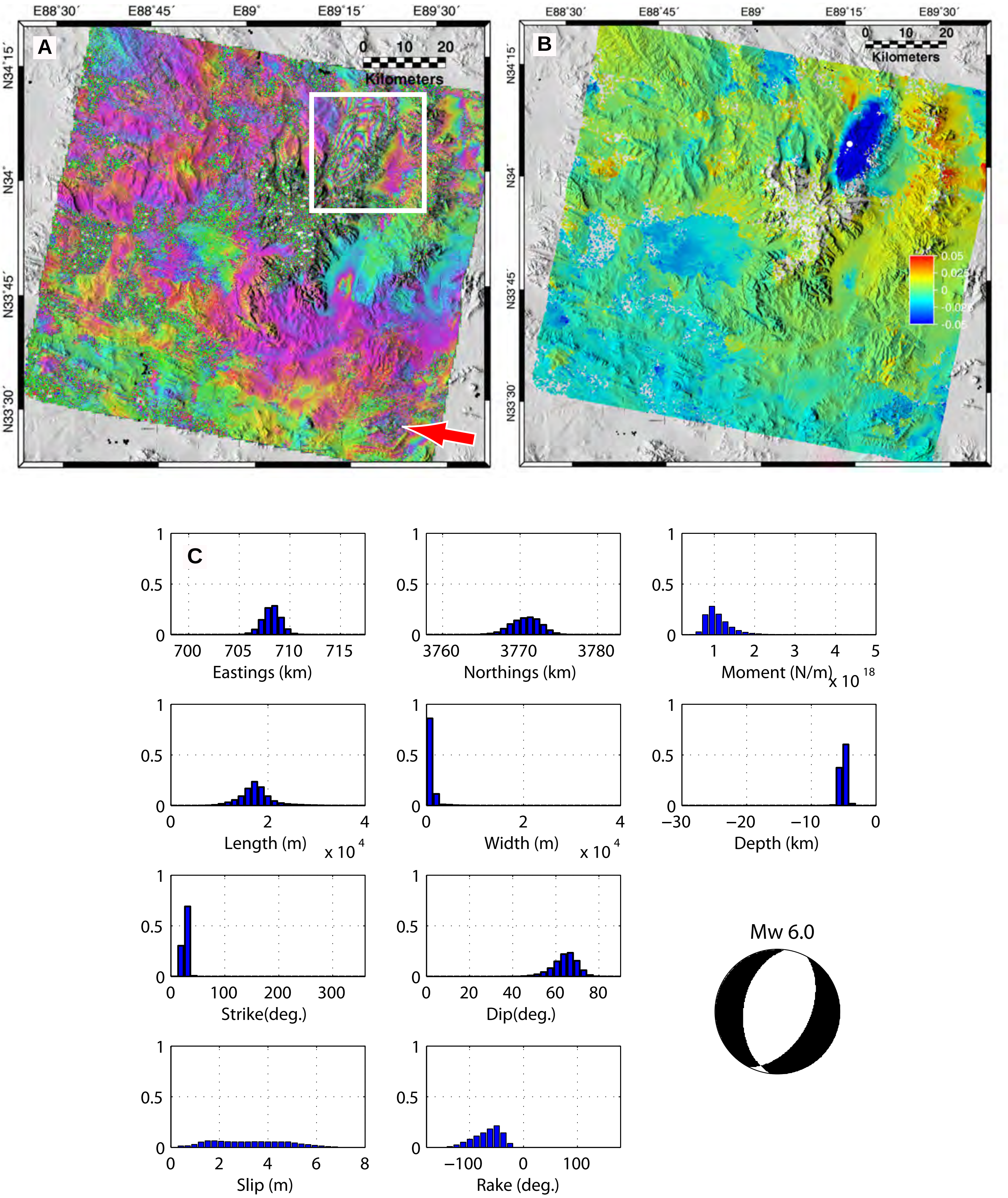

Figure 16. Event 13: 3/27/04, Tibet. Descending satellite view. A. Unwrapped interferometric phase (1 color cycle = 2 pi). B. Line-of-sight displacement field. Red Arrow indicates the look-direction of the satellite. White dot indicates epicenter location of the favored model. C. Gibbs Sampling inversion results with Ts =1 and 120,000 iterations and Harvard CMT.

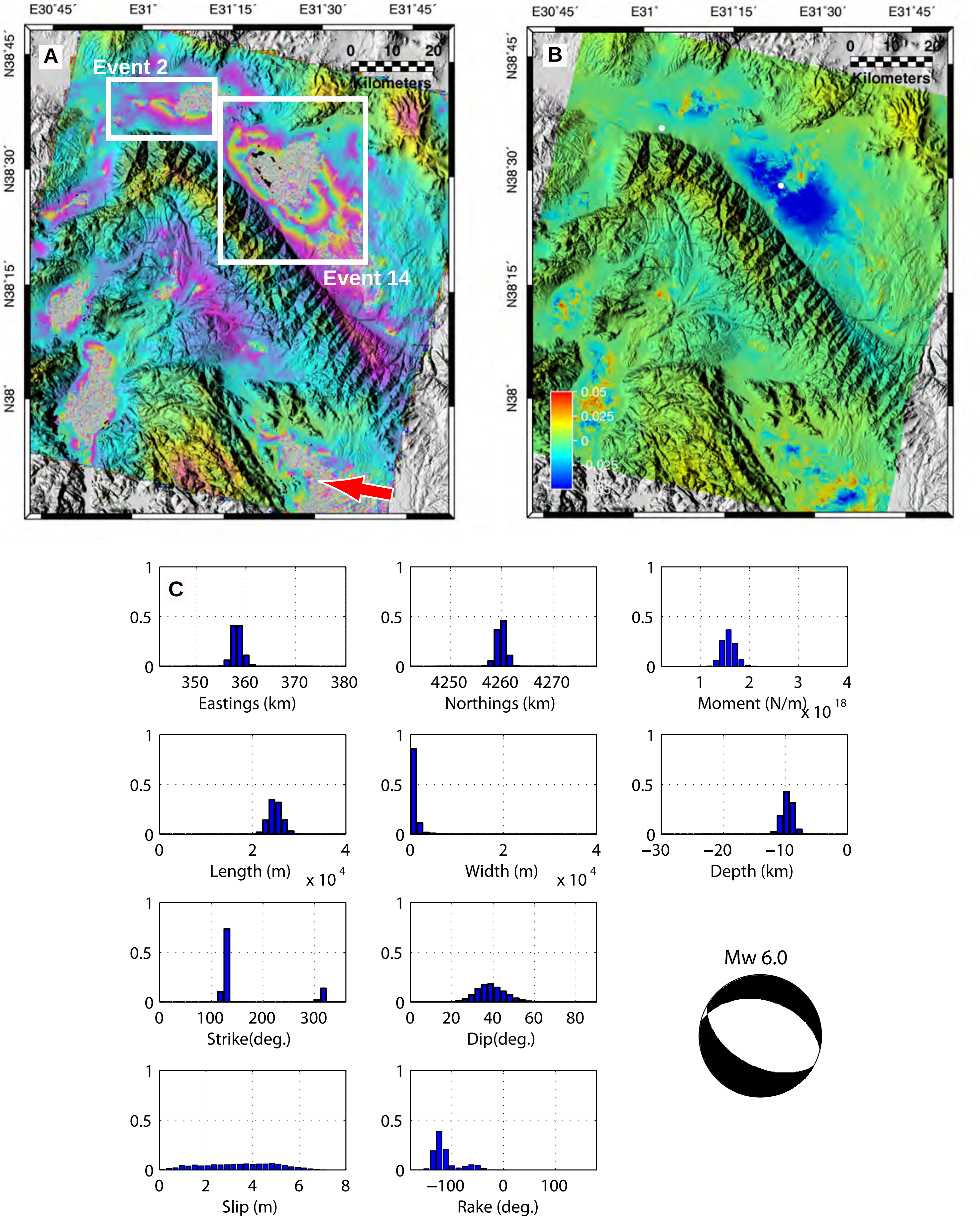

Figure 17. Event 14: 12/15/2000, Turkey. Descending satellite view. A. Unwrapped interferometric phase (1 color cycle = 2 pi). B. Line-of-sight displacement field. Red Arrow indicates the look-direction of the satellite. White dot indicates epicenter location of the favored model. C. Gibbs Sampling inversion results with Ts =3 and 140,000

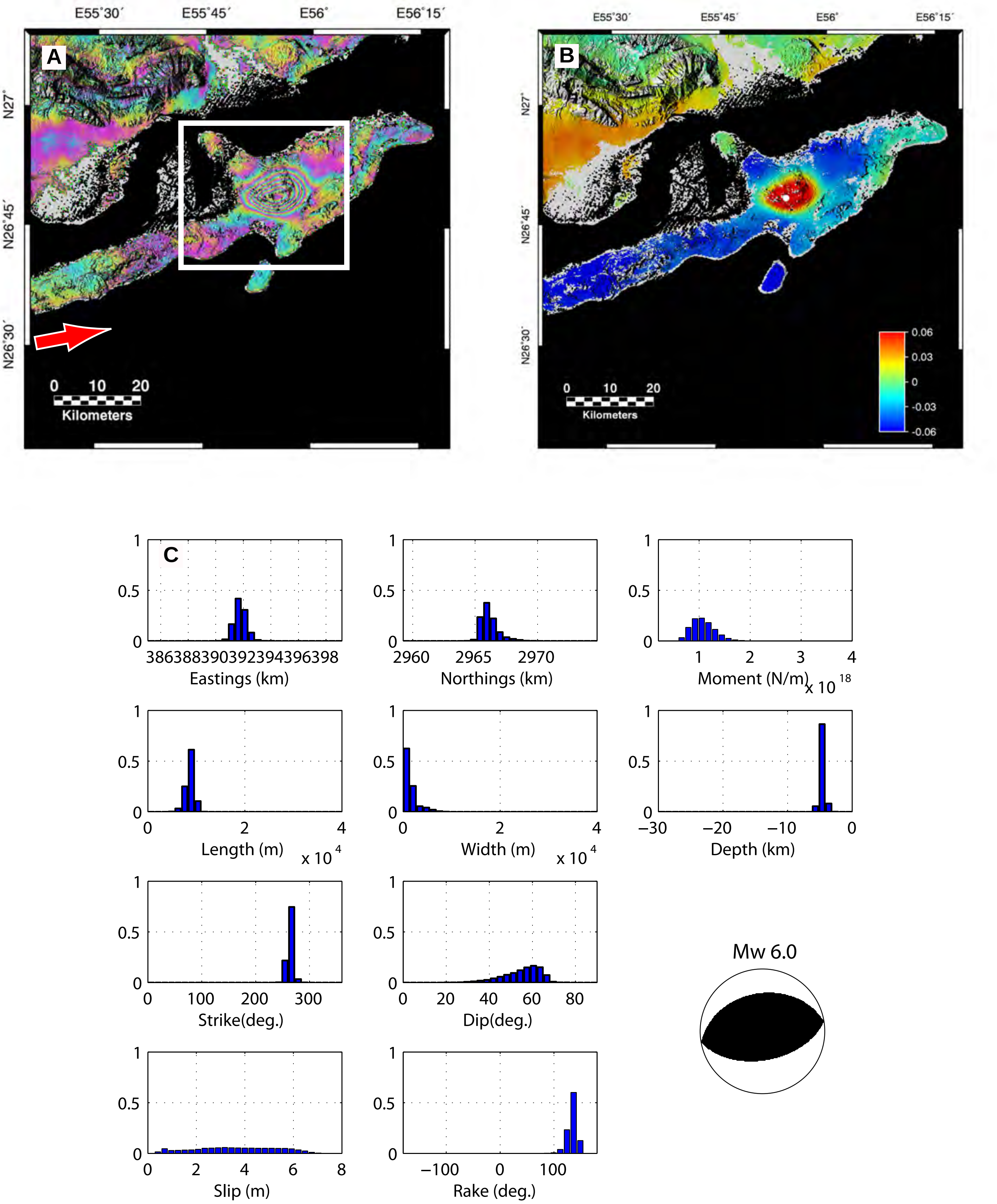

Figure 18. Event 15: 11/27/05, Iran. Ascending satellite view. A. Unwrapped interferometric phase (1 color cycle = 2 pi). B. Line-of-sight displacement field. Red Arrow indicates the look-direction of the satellite. White dot indicates epicenter location of the favored model. C. Gibbs Sampling inversion results with Ts = 1 and 100,000 iterations and Harvard CMT.

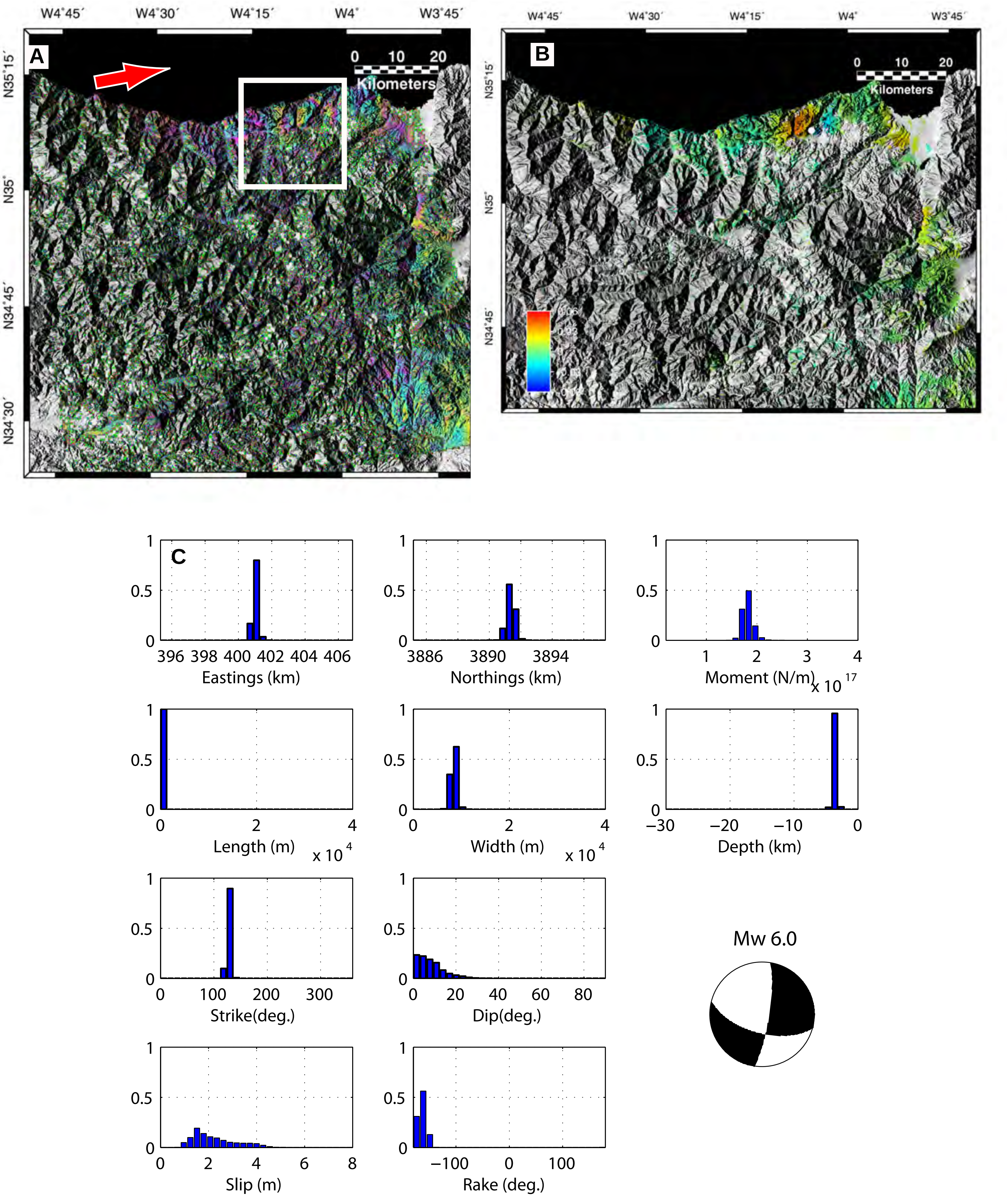

Figure 19. Event 16: 5/31/94, Morocco. Ascending satellite view. A. Unwrapped interferometric phase (1 color cycle = 2 pi). B. Line-of-sight displacement field. Red Arrow indicates the look-direction of the satellite. White dot indicates epicenter location of the favored model. C. Gibbs Sampling inversion results with Ts = 1 and 100,000 iterations and Harvard CMT.

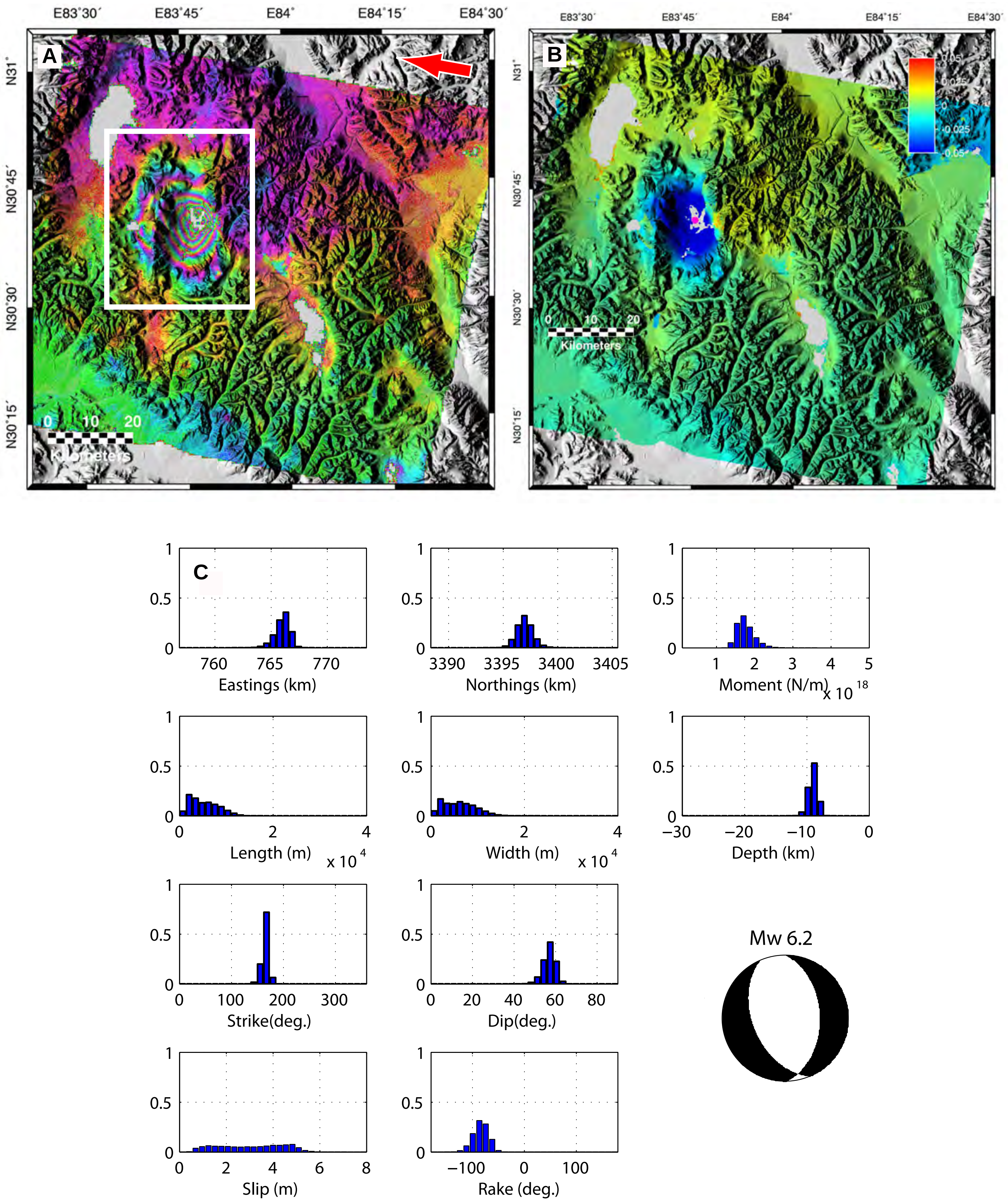

Figure 20. Event 17 7/11/04, Tibet. Descending satellite view. A. Unwrapped interferometric phase (1 color cycle = 2 pi). B. Line-of-sight displacement field. Red Arrow indicates the look-direction of the satellite. Magenta dot indicates epicenter location of the favored model. C. Gibbs Sampling inversion results with Ts =1 and 100,000

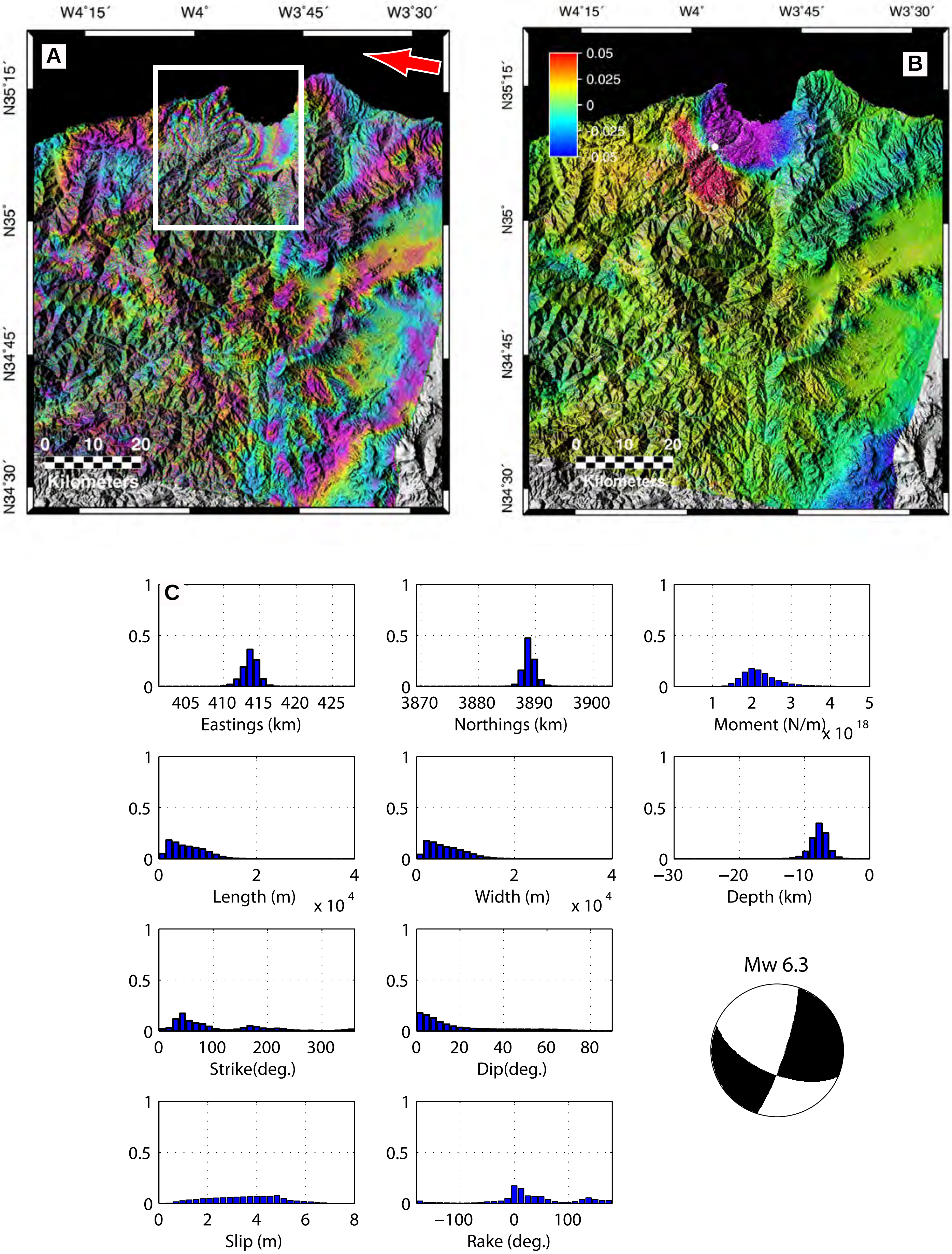

Figure 21. Event 18: 2/24/04, Morocco. Descending satellite view. A. Unwrapped interferometric phase (1 color cycle = 2 pi). B. Line-of-sight displacement field. Red Arrow indicates the look-direction of the satellite. White dote indicates epicenter location of the favored model. C. Gibbs Sampling inversion results with Ts=1, 190,000 iterations and Harvard CMT.

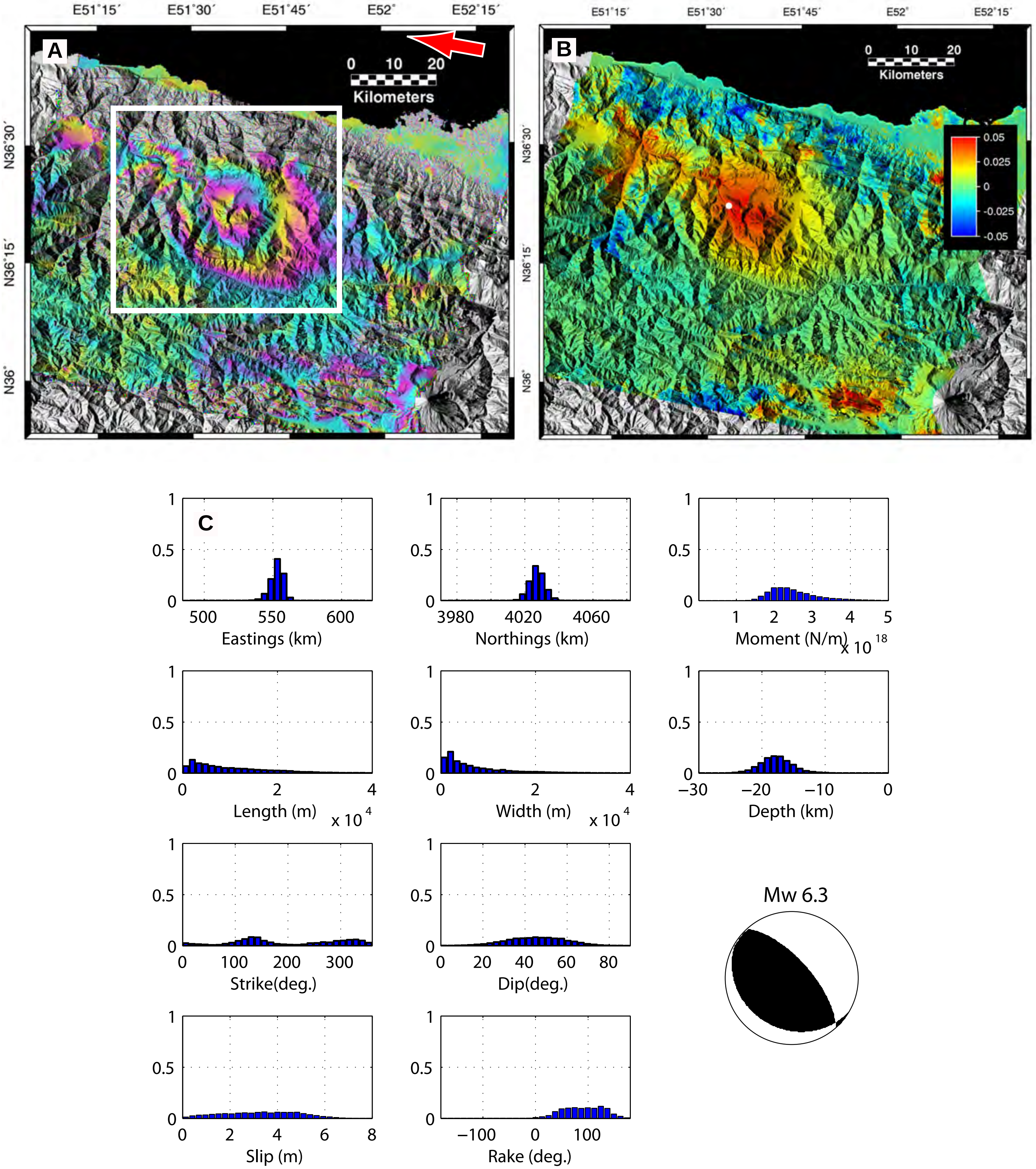

Figure 22. Event 19: 5/28/2004, Iran. Descending satellite view. A. Unwrapped interferometric phase (1 color cycle = 2 pi). B. Line-of-sight displacement field. Red Arrow indicates the look-direction of the satellite. White dot indicates epicenter location of the favored model. C. Gibbs Sampling inversion results with Ts =3 and 140,000 iterations.

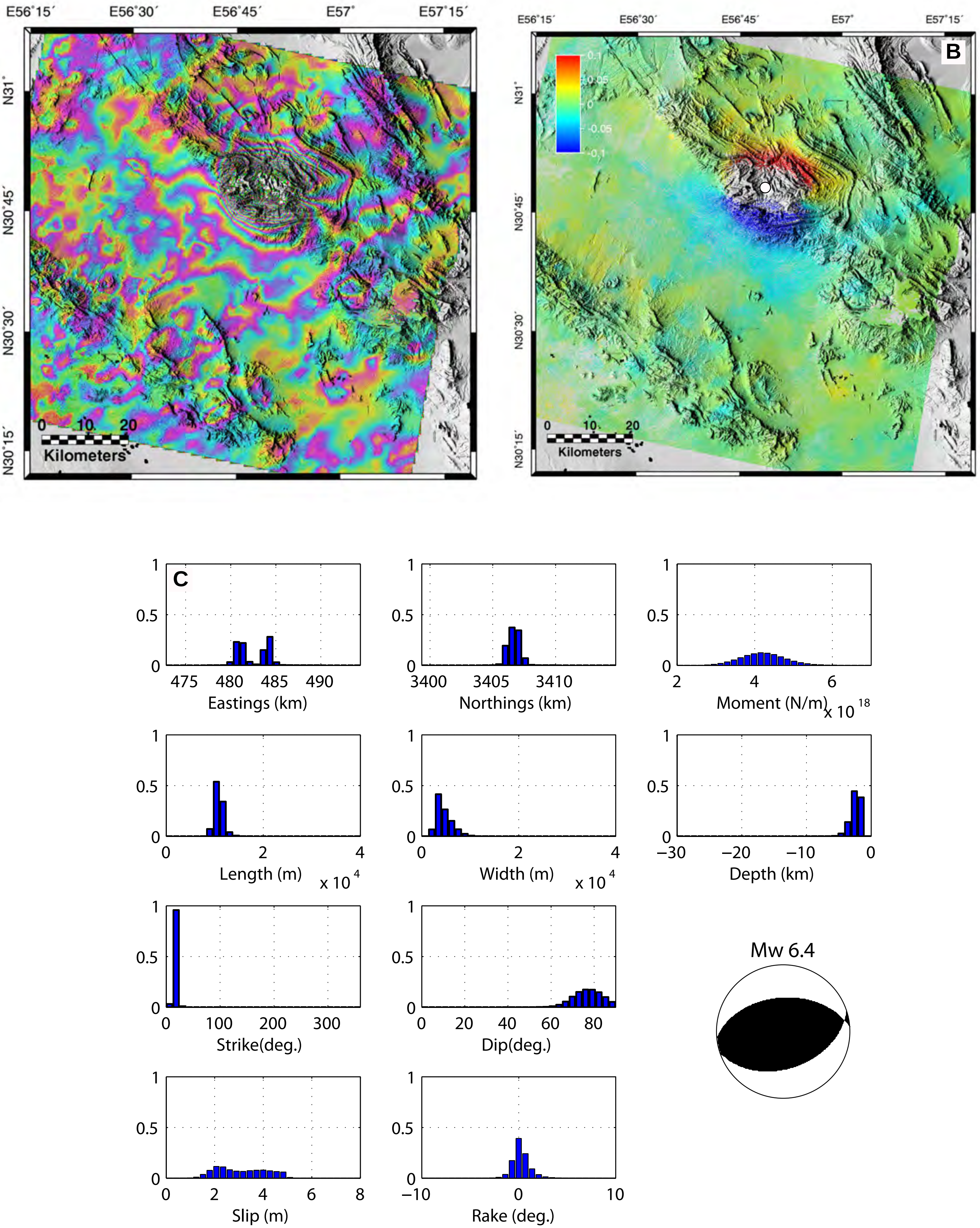

Figure 23. Event 20: 2/22/05, Iran. Descending satellite view. A. Unwrapped interferometric phase (1 color cycle = 2 pi). B. Line-of-sight displacement field. Red Arrow indicates the look-direction of the satellite. White dot indicates epicenter location of the favored model. C. Gibbs Sampling inversion results with Ts = 1 and 180,000 iterations and Harvard CMT.

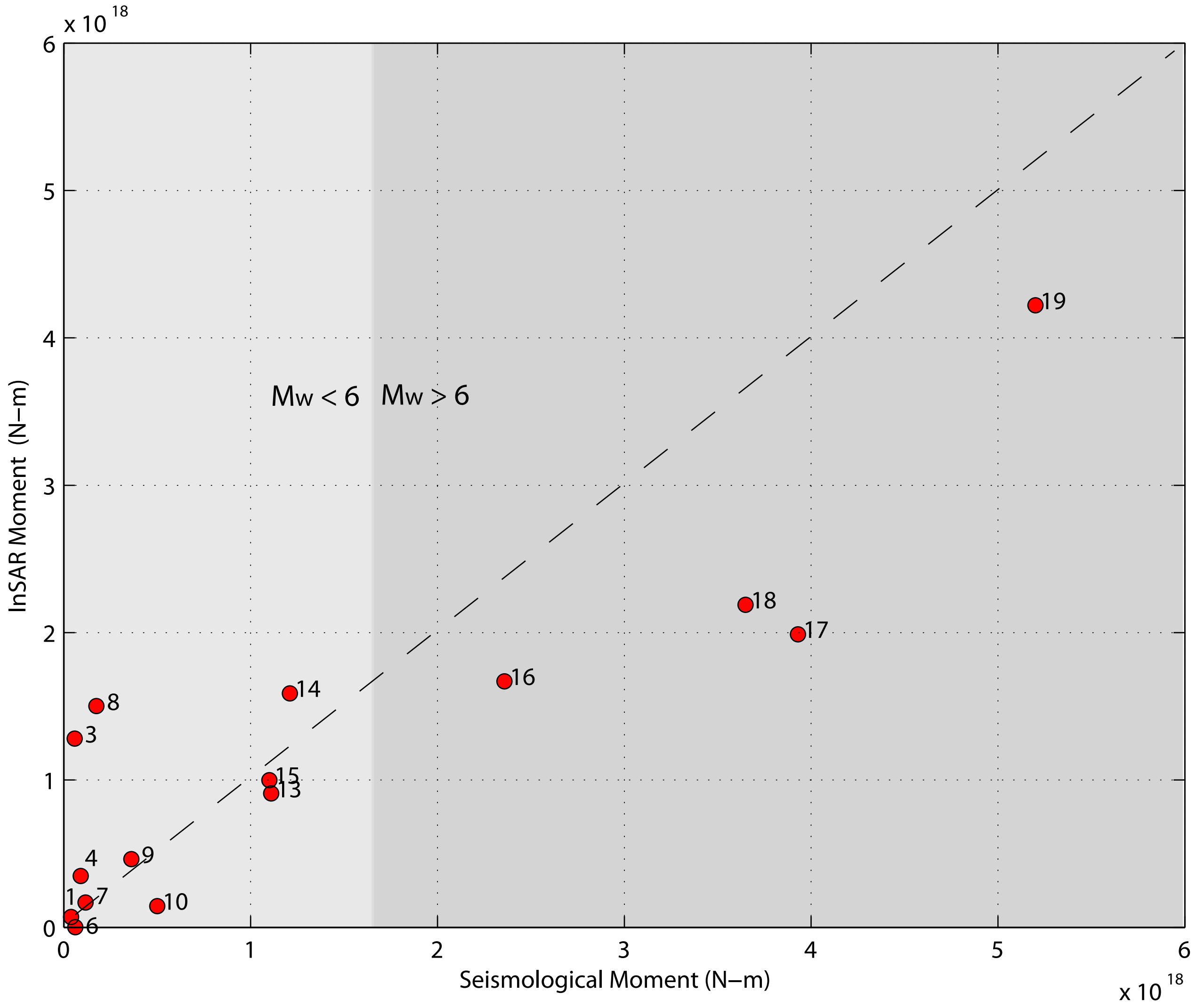

Figure 24. Comparison of seismological- and InSAR-derived scalar moments. Event ID numbers are indicated.

5. DISCUSSION & RECOMMENDATIONS

Our study takes some important steps towards the goal of creating an InSAR-based GT5 catalog for remote regions. We have shown that InSAR, provided that data bracketing the seismic events have been acquired, can routinely image the ground deformation associated with small ~M_w 5 earthquakes which are the best candidates for GT5 calibration events (Figures 3-22). Although we encountered many challenges with the successful application of this technique, we firmly believe that the outlook for the future of InSAR to provide ground truth is very good. This prognosis is based one the new generation of satellite-born SAR systems, as well as the application of emerging techniques.

5.1 New Satellites

When this study began in mid 2004, the primary source of data was the ERS 1/2 data archive from ESA (the new Envisat platform had been in operation for only about one year at that time). As discussed above, ERS 1 ceased operation in 2000, and ERS 2 suffered navigational problems in early 2001 that complicated (if not precluded) interferometry. Even before that navigational failure, orbits of the ERS satellites were not always maintained appropriately for interferometry – i.e., the satellite baselines were simply too large. Owing to limited onboard storage data were not always acquired, and even if they were, the baselines were not always useful. It should be remembered that the ERS satellites were not designed with interferometric applications in mind. Hence, we believe that the future prospects should not be inferred from experiences with the older ERS 1/2 data.

The usefulness of data from the new generation of SAR platforms has been well demonstrated with SAR data from ESA's Envisat in this study. Unlike the ERS satellites, Envisat was designed with interferometric applications in mind. Compared with the older ERS missions, Envisat has significantly better navigational systems, as well as large onboard data storage capacity. Hence, in the past 3 years of operation, the data archive has grown significantly, and much more of the data are appropriate for interferometry. Envisat also has the ability to acquire radar data with different polarizations – in comparison with the standard vertical/vertical polarization, horizontal/horizontal polarization can improve coherence in regions with some vegetation.

Aside from Envisat, other new generation satellite platforms will also become operational within the next year, including Radarsat-2 (a fully polarimetric, C-band radar system), ALOS (a dual polarization, L-band radar system). Within a decade, a significant constellation of satellite-born SAR systems will exist, facilitating interferometric applications more regularly than were possible using data from the 1990s.

5.2 New Techniques

Aside from new data sources, new techniques have the prospect of expanding the range of applicability of InSAR for determining ground truth events. Aside from multi-polarimetric capabilities mentioned above, most of the new SAR systems also can acquire wide SAR images – what is commonly known as ScanSAR mode. Although lower in spatial resolution by a factor of 5, they cover significantly larger areas. ScanSAR interferometry has recently been demonstrated to be feasible – the benefit of this approach is that a sufficiently large area can be imaged that it will encompass the uncertainties in the seismological locations.

Modeling of atmospheric phase anomalies using other weather models (e.g. Foster et al., 2006) and/or remote sensing data has been explored in recent years Cloudless total water vapor estimates based on near infrared imagery are provided by NASA’s Aqua and Terra satellites (the MODIS sensor), as well as Envisat’s MERIS sensor. These have spatial resolutions of 1 km or better, which can facilitate modeling of phase anomalies that can be subtracted from the interferograms.

Another emerging technique involves the use of permanent (or persistent) scatterers (e.g., Ferretti et al., 2001; Werner et al., 2003; Hooper et al.). These techniques avoid temporal decorrelation by identifying stable scattering pixels and determining deformation for those pixels only, based on a large volume of SAR scenes. As part of the process, atmospheric phase contributions are filtered and removed. The volume of data also improves the sensitivity of the technique to less than a mm of range change (e.g. Werner et al., 2003). Although originally developed to monitor small deformations, these same techniques can also be applied to co-seismic deformation. With the removal of atmospheric phase anomalies and the increased sensitivity to deformation, it is conceivable that these techniques may permit imaging deformation of earthquakes smaller than magnitude 5.

5.3 Creation of an InSAR-based GT Catalog

We have shown that the Gibbs Sampling approach for inverting the InSAR-derived displacement field can provide source parameter estimates for the seismic events which allows self-consistent assessment of whether they satisfy GT5 criteria. It is important to note that in this study, because our goal was to remain as objective as possible, we have not ‘tuned’ our approach based on assumptions, such as expected dislocation aspect ratios, ranges of strikes and dips, or focal mechanisms. We fully recognize that there are proper ways of incorporating into our inversion useful prior information and their errors (such as focal mechanism, or regional tectonics) but the goal of this first stage of research was to investigate the possibility of displacement fields alone to yield GT5 results. Our success rate of delivering GT5 parameters for events less than Mw 5.5 was 25% (2 of 8). Accordingly, we find that more often than not, additional information is likely needed to provide GT5 results from InSAR-derived displacement fields. The ‘other’ information could include: multiple InSAR look-angle displacement fields from the same event (e.g.Wright et al., 2004), focal mechanisms, waveforms.

Furthermore, actually populating a catalog with GT5 events is particularly challenging, because little is known about the source mechanics of small earthquakes (e.g.McGuire, 2004). For instance, in order to form a computationally tractable inverse problem, we follow Okada's (1985) approximation of an earthquake slip patch as a rectangular dislocation in an elastic half-space. However, how accurate is it to approximate the slip patch associated with a small earthquake by a rectangle?

As a result, we recommend that further programmatic and research steps be undertaken to improve the efficiency of InSAR-based GT5 events. Specifically, we recommend that:

1) For regions of heightened interest, the AFRL should routinely task and archive data from all available satellites. As discussed above, the lack of data acquisition was one one of the major reasons why this study could not produce more GT5 candidate events.
2) Further research be undertaken to allow consistent and appropriate incorporation of additional information into the inversion of the displacement field. This could range from performing full joint displacement field/waveform inversions to using focal mechanism kinematic constraints on the current formulation of the coseismic geodetic inverse problem.
3) Further research be undertaken to reformulate the coseismic geodetic inverse problem so that it does not rely on rectangles, but rather on smaller scale geometrical elements, such as point sources.

REFERENCES

Basu, A., and Frazer, L.N., 1990, Rapid Determination of the Critical Temperature in Simulated Annealing Inversion: Science, v. 249, p. 1409-1412.

Begnaud, M.L., McNally, K.C., Stakes, D.S., and Gallardo, V.A., 2000a, A crustal velocity model for locating earthquakes in Monterey Bay, California: Bulletin of the Seismological Society of America, v. 90, p. 1391-1408.

Begnaud, M.L., Velasco, A.A., and Steck, L.K., 2000b, Utilizing results from InSAR to develop seismic location benchmarks and implications for seismic source studies, 22nd Annual DOD/DOE Seismic Research Symposium: New Orleans, LA.

Brooks, B., and Frazer, L.N., 2005a, Importance reweighting reduces dependence on temperature in Gibbs samplers: an application to the coseismic geodetic inverse problem: Geophys. J Int., v. 161, p. 12-21.

Brooks, B.A., and Frazer, L.N., 2005b, Importance reweighting reduces dependence on temperature in Gibbs samplers: an application to the coseismic geodetic inverse problem: Geophys. J Int., v. 161, p. 12-21.

Burgmann, R., Rosen, P.A., and Fielding, E.J., 2000, Synthetic Aperture Radar interferometry to measure Earth's surface topography and it's deformation: Ann. Rev. Earth Planet. Sci., v. 28, p. 169-209.

Cervelli, P., Murray, M.H., Segall, P., Aoki, Y., and Kato, T., 2001, Estimating source parameters from deformation data, with an application to the March 1997 earthquake swarm off the Izu Peninsula, Japan: Journal of Geophysical Research, v. 106, p. 11,217-11,237.

Chen, C., and Zebker, H., 2000, Network approaches to two-dimensional phase unwrapping: intractability and two new algorithms: Journal of the Optical Society of America, v. 17, p. 401-414.

Constantini, M., 1998, A novel phase unwrapping method based on network programming: IEEE Transactions on Geoscience and Remote Sensing, v. 36, p. 813-821.

Council, N.R., 1997, Research required to support comprehensive nuclear test ban treaty monitoring: Washington, D.C., National Academy Press, 138 p.

Creutz, M., 1980, Monte-Carlo study of quantized SU(2) gauge theory: Phys. Rev. D, v. 21, p. 2308-2315.

Doyle, G.S., Stow, R.J., and Inggs, M.R., 2001, Satellite radar interferometry reveals mining induced seismic deformation in South Africa, Geoscience and Remote Sensing Symposium, 2001. IGARSS '01., Volume 5, IEEE 2001 International, p. 2037 - 2039.

Engdahl, E.R., van der Hilst, R.D., and Buland, R.P., 1998, Global teleseismic earthquake relocation with improved travel times and procedures for depth determination: Bulletin of the Seismological Society of America, v. 88, p. 722-743.

Foster, J., Brooks, B., Cherubini, T., Shacat, C., Businger, S., and Werner, C.L., 2006, Mitigating atmospheric noise for InSAR with a high resolution weather model: Geophys. Res. Lett., v. 33, p. doi:10.1029/2006GL026781.

Geman, S., and Geman, D., 1984, Stochastic relaxation, Gibbs distributions and the Bayesian restoration of images: IEEE Trans. Patt. Analysis Mach. Int., v. 6, p. 721-741.

Gomez, F., Khawlie, M., Tabet, C., Khair, K., Darkal, A.N., and Barazangi, M., 2006, Neotectonics of the northern Dead Sea fault system in Lebanon and Syria based on SAR imagery and high resolution DEM data: Earth and Planetary Science Letters, p. 913-931.

Hagos, L., Shomali, H., and Roberts, R., 2006, Re-evaluation of focal depths and source mechanisms of selected earhquakes in the Afar depression: Geophys. J Int., v. 167, p. 297-308.

Jaschke, L., 1997, Geophysical Inversion by the Freeze Bath Method with an Application to Geoacoustic Ocean Bottom parameter Estimation [Ph.D. thesis], University of Victoria.

Jónsson, S., Zebker, H., Segall, P., and Amelung, F., 2002, Fault slip distribution of the 1999 Mw 7.1 Hector Mine, California, earthquake, estimated from satellite radar and GPS measurements: Bulletin of the Seismological Society of America, v. 92, p. 1377-1389.

Kirkpatrick, S., Gelatt, C.D.J., and Vecchi, M.P., 1983, Optimization by simulated annealing: Science, v. 220, p. 671-680.

Lohmann, R.B., Simons, M., and Savage, B., 2002, Location and mechanism of the Little Skull Mountain earthquake as constrained by satellite radar interferometry and seismic waveform modeling: Journal of Geophysical Research, v. 107.

Lu, Z., and Freymueller, J.T., 1998, Synthetic aperture radar interferometry coherence analysis over Katmai volcano group, Alaska: Journal of Geophysical Research, B, Solid Earth and Planets, v. 103, p. 29,887-29,894.

Massonnet, D., and Feigl, K.L., 1998, Radar interferometry and its application to changes in the earth's surface: Reviews of Geophysics, v. 36, p. 441-500.

Massonnet, D., and K.L. Feigl, K.L., 1995, Discrimination of Geophysical Phenomena in Satellite Radar Interferograms,: Geophysical Research Letters, v. 22, p. 1537-1540.

Massonnet, D., Rossi, M., Carmona, C., Adragna, F., Peltzer, G., Feigl, K., and Rabaute, T., 1993, The displacement field of the Landers earthquake mapped by radar interferometry: Nature, v. 364, p. 138-142.

McGuire, J.J., 2004, Estimating Finite Source Properties of Small Earthquake Ruptures: Bulletin - Seismological Society of America, v. 94, p. 377-393.

Metropolis, N., Rosenbluth, A., Rosenbluth, M., Teller, A., and Teller, E., 1953, Equation of state calculations by fast computing machines: J. Chem. Phys, v. 21, p. 1087-1092.

Mosegaard, K., and Sambridge, M., 2002, Monte Carlo analysis of inverse problems: Inverse Problems, v. 18, p. 29-54.

Murray, M.H., Marshall, G.A., Lisowski, M., and Stein, R.S., 1996, The 1992 M=7 Cape Mendocino, California, earthquake: Coseismic deformation at the south end of the Cascadia megathrust: Journal of Geophysical Research, v. 101, p. 17,707-17,725.

Myers, S., and Schultz, C., 2000, Improving sparse network location with Bayesian kriging and teleseismically constrained calibration events: Bull. Seismol. Soc. Am., v. 90, p. 199-211.

Okada, Y., 1985, Surface deformation due to shear and tensile faults in a half-space: Bulletin of the Seismological Society of America, v. 75, p. 1135-1154.

Peltzer, G., and Rosen, P., 1995, Surface displacement of the 17 May 1993 Eureka Valley, Claifornia earthquake observed by SAR interferometry: Science, v. 268, p. 1333-1336.

Pomeroy, P., Best, J., and McEvilly, T., 1982, Test ban treaty verification with regional data - a review: Bull. Seism. Soc. Am., v. 72, p. S89-S129.

Press, W.H., Teukolsky, S.A., Vetterling, W.T., and Flannery, B.P., 1992, Numerical Recipes in C: New York, Cambridge Univ. Press, 994 p.

Price, E.J., and Burgmann, R., 2002, Interactions Between the Landers and Hector Mine, California, Earthquakes from Space Geodesy, Boundary Element Modeling, and Time-dependent Friction: BSSA, v. 92, p. 1450-1469.

Rebbi, C., 1984, *in* Binder, K., ed., Applications of the Monte Carlo Method: New York, Springer-Verlag, p. 277-298.

Rosen, P.A., Hensley, S., Joughin, I.R., Li, F.K., Madsen, S.N., Rodriguez, E., and Goldstein, R.M., 2000, Synthetic Aperture Radar Interferometry: Proceed. of the IEEE, v. 88.

Rothman, D.H., 1985, Nonlinear inversion, statistical mechanics, and residual statics estimation: Geophysics, v. 50, p. 2784-2796.

—, 1986, Automatic estimation of large residual statics corrections: Geophysics, v. 51, p. 332-346.

Sandwell, D.T., and Price, E.J., 1998, Phase gradient approach to stacking interferograms: Journal of Geophysical Research, v. 103, p. 30,183-30,204.

Sandwell, D.T., and Sichoix, L., 2000, Topographic phase recovery from stacked ERS interferometry and a low-resolution digital elevation model: Journal of Geophysical Research, v. 105, p. 28,211-28,222.

Schultz, C., Myers, S., Hipp, J., and Young, C., 1998, Nonstationary Bayesian kriging: application of spatial corrections to improve seismic detection, location and identification: Bull. Seism. Soc. Am., v. 88, p. 1,275-1,288.

Werner, C., Wegmüller, U., Strozzi, T., and Wiesmann, A., 2000, GAMMA SAR and Interferometric Processing Software, ERS-ENVISAT Symposium: Gothenborg, Sweden.

Wicks, C.W., Jr., Thatcher, W.R., and Dzurisin, D., 1998, Migration of fluids beneath Yellowstone Caldera inferred from satellite radar interferometry: Science, v. 282, p. 458-462.

Williams, S., Bock, Y., and Fang, P., 1998, Integrated satellite interferometry: Tropospheric noise, GPS estimates and implications for interferometric synthetic aperture radar products.: Journal of Geophysical Research, p. 27,051-27,067.

Wright, T.J., Parsons, B., and Lu, Z., 2004, Toward mapping surface deformation in three dimensions using InSAR: Geophysical Research Letters, v. 31, p. 1607.

Zebker, H.A., Rosen, P.A., Goldstein, R.M., Gabriel, A., and Werner, C.L., 1994, On the derivation of coseismic displacement fields using differential radar interferometry: The Landers earhtquake: Journal of Geophysical Research, v. 99, p. 19,617-19,634.

Zebker, H.A., Rosen, P.A., and Hensley, S., 1997, Atmospheric effects in interferometric synthetic aperture radar surface deformation and topographic maps: Journal of Geophysical Research, v. 102, p. 7547-7563.

Zebker, H.A., and Villasenor, J., 1992, Decorrelation in interferometric radar echoes: EEE Trans. Geo. Rem. Sensing, v. 30, p. 950-959.

Appendix A.
Seismological Results

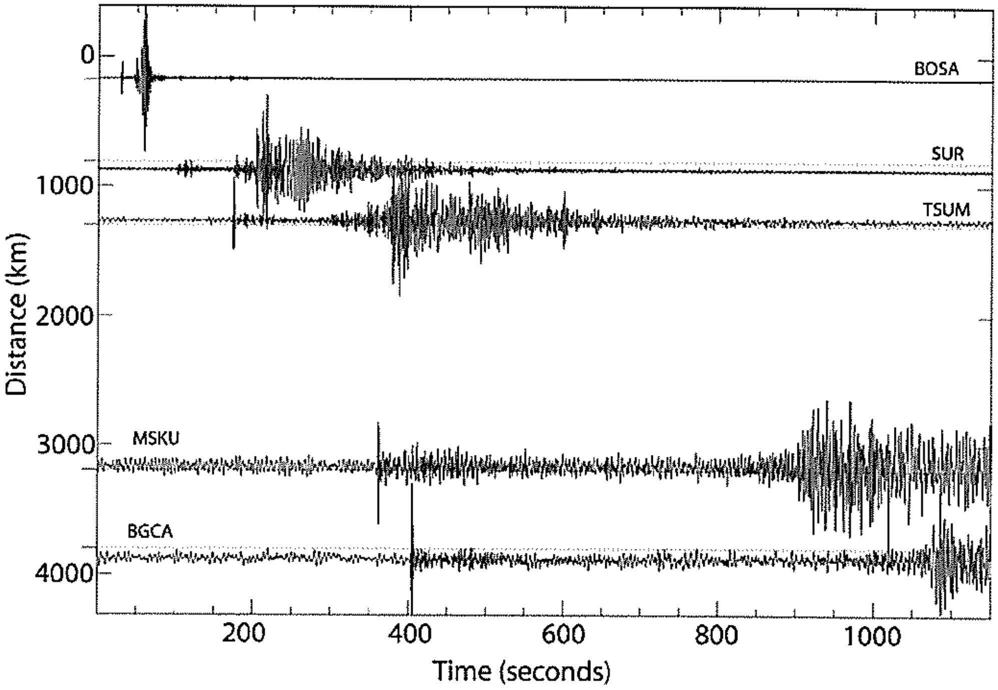

Figure A1. Example of origin time determination for the South Africa event.

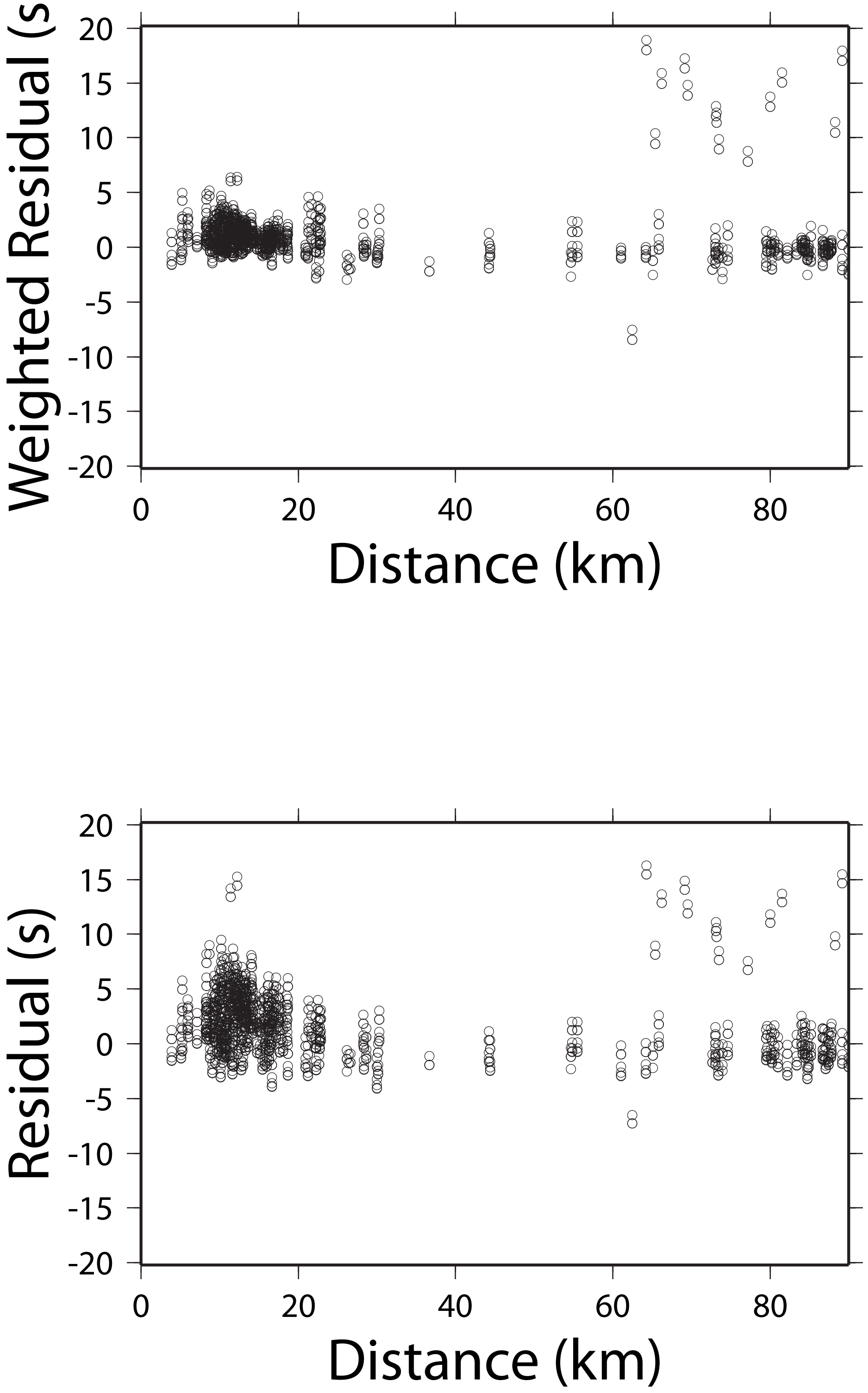

Figure A1. Weighted and unweighted residuals from the origin time recalculation as a function of distance for Event 1 (Tunisia, 3/20/97).

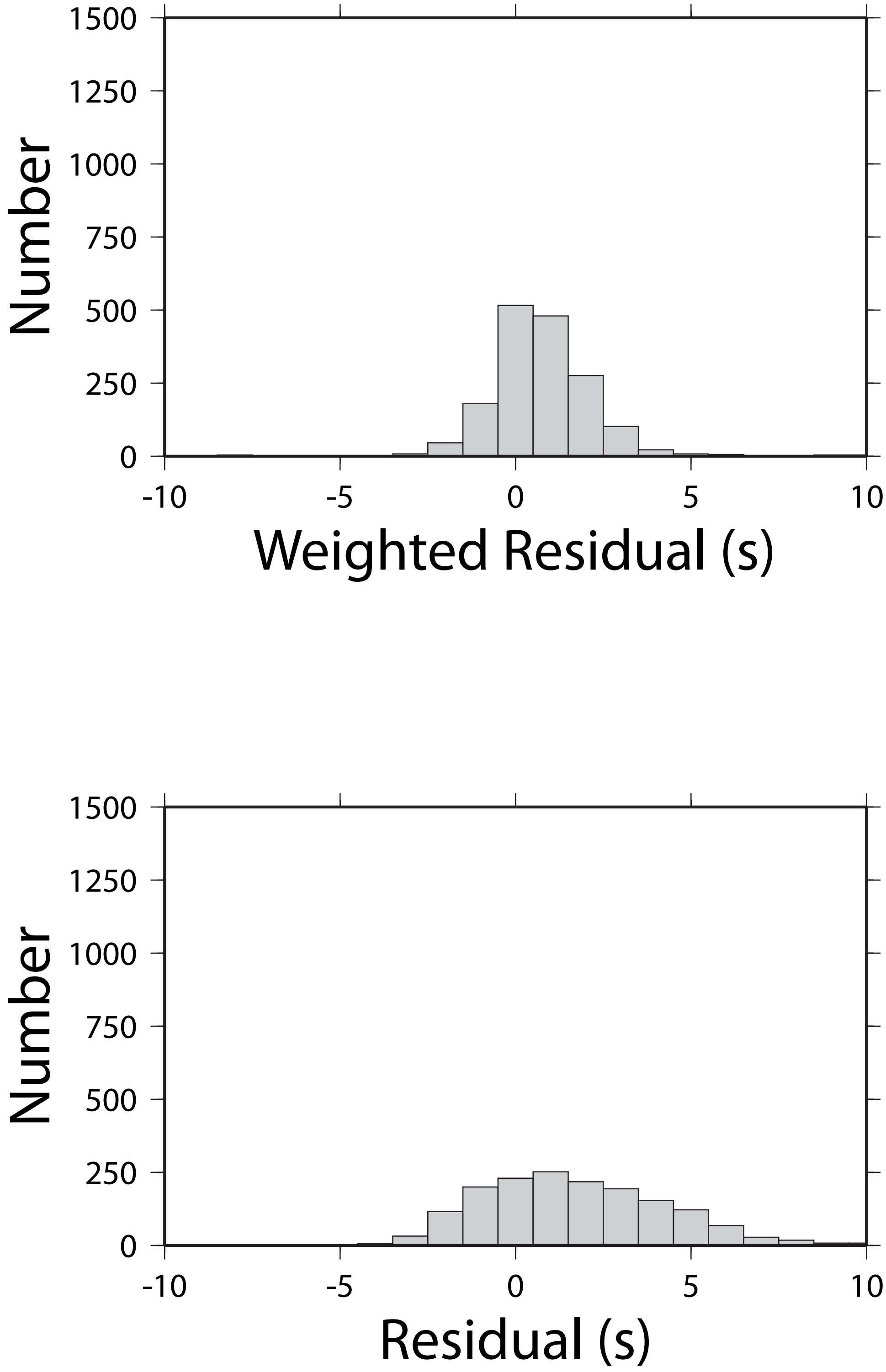

Figure A2. Histograms of weighted and unweighted residuals from the origin time recalculation for Event 1 (Tunisia, 3/20/97).

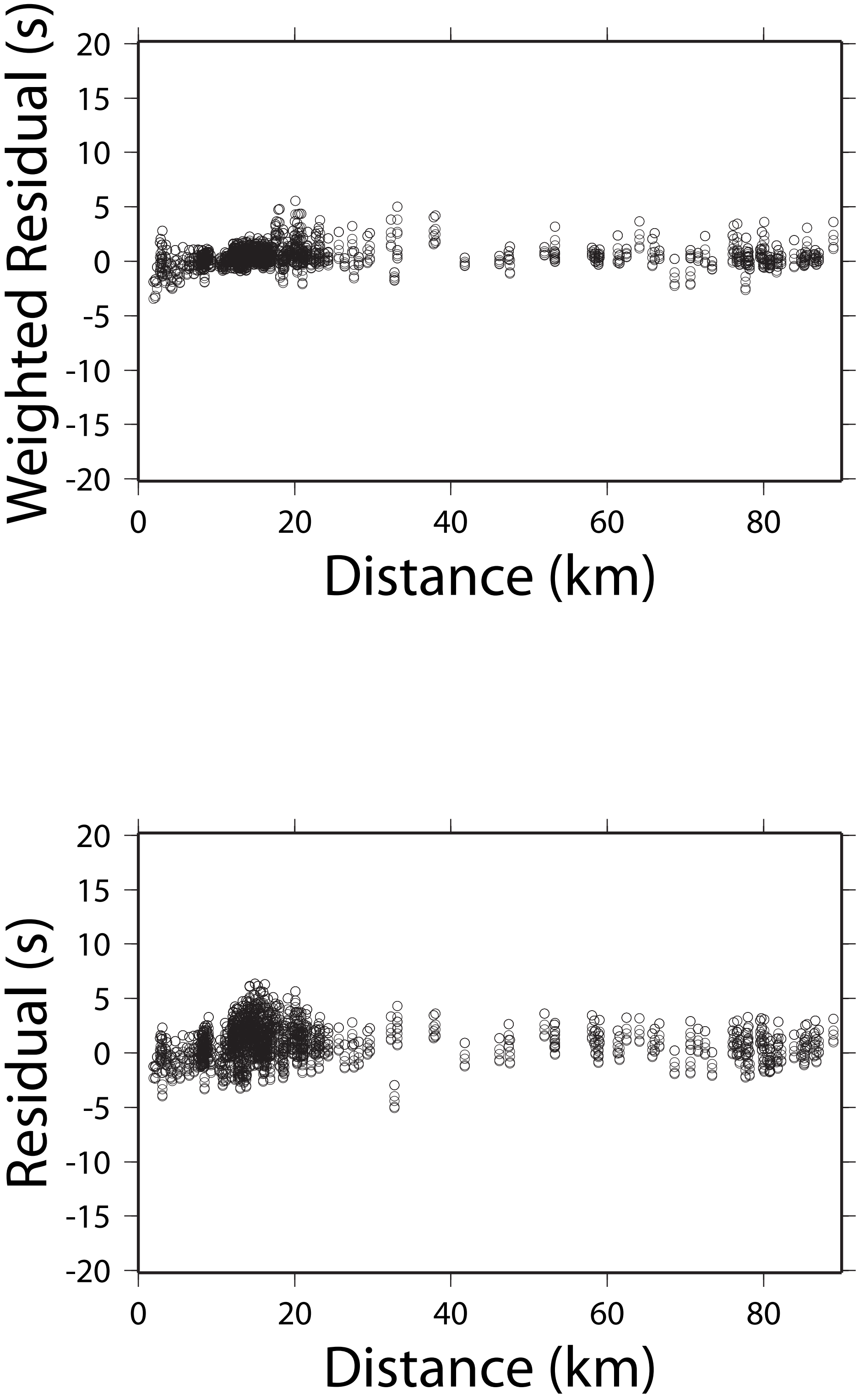

Figure A3. Weighted and unweighted residuals from the origin time recalculation as a function of distance for Event 3 (Morocco, 12/04/04).

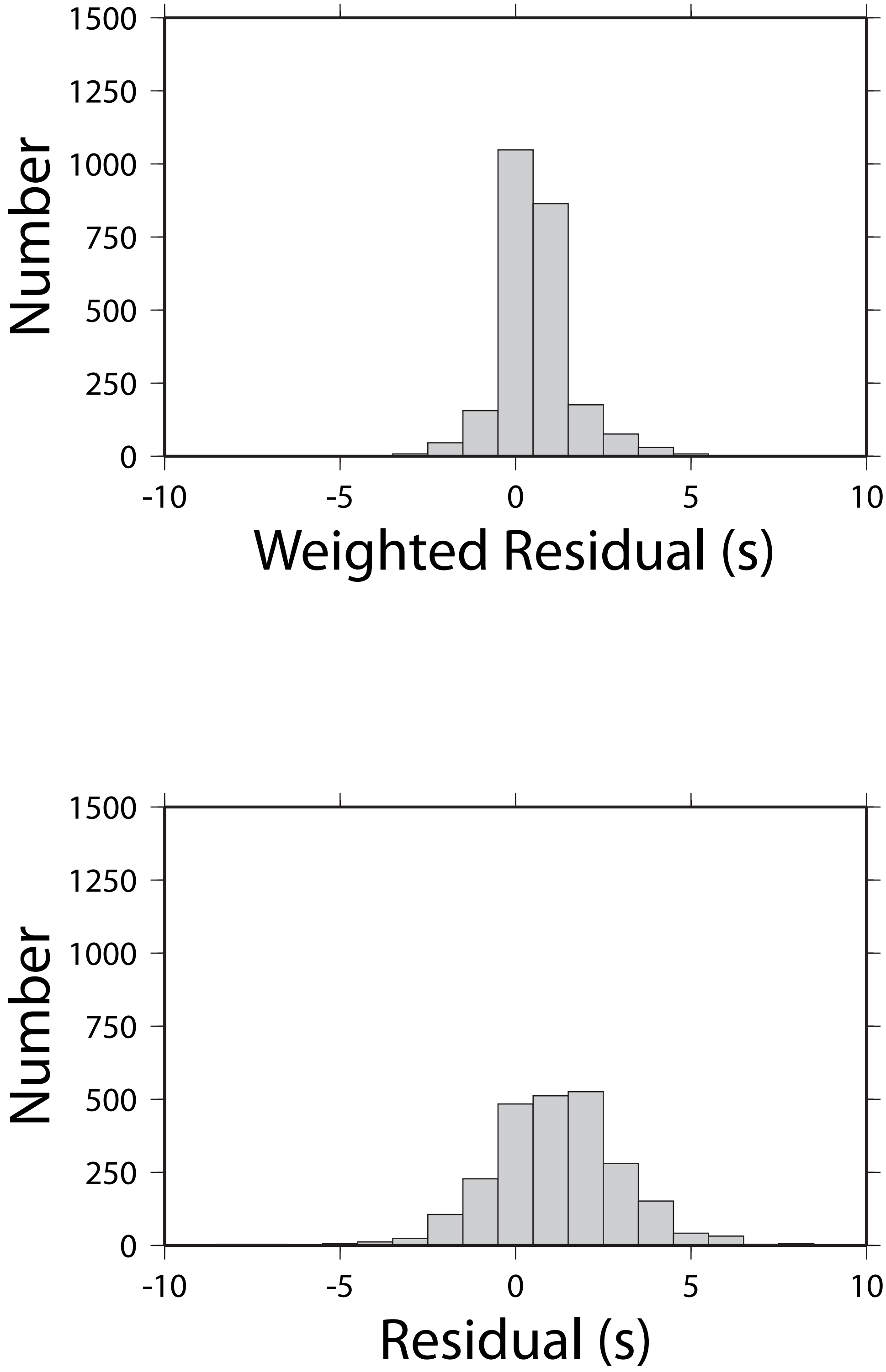

Figure A4. Histograms of weighted and unweighted residuals from the origin time recalculation for Event 3 (Morocco, 12/04/04).

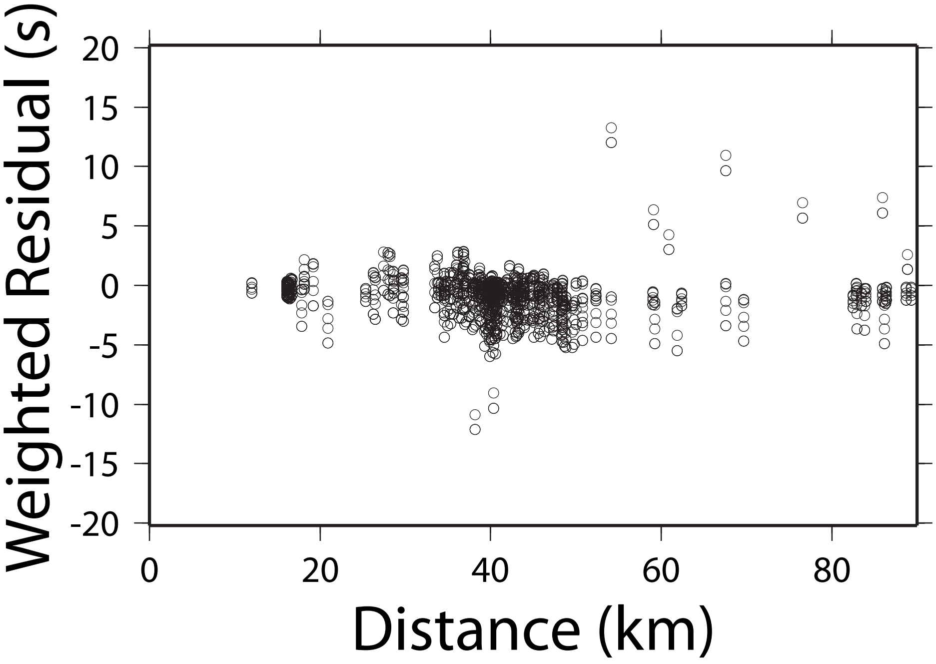

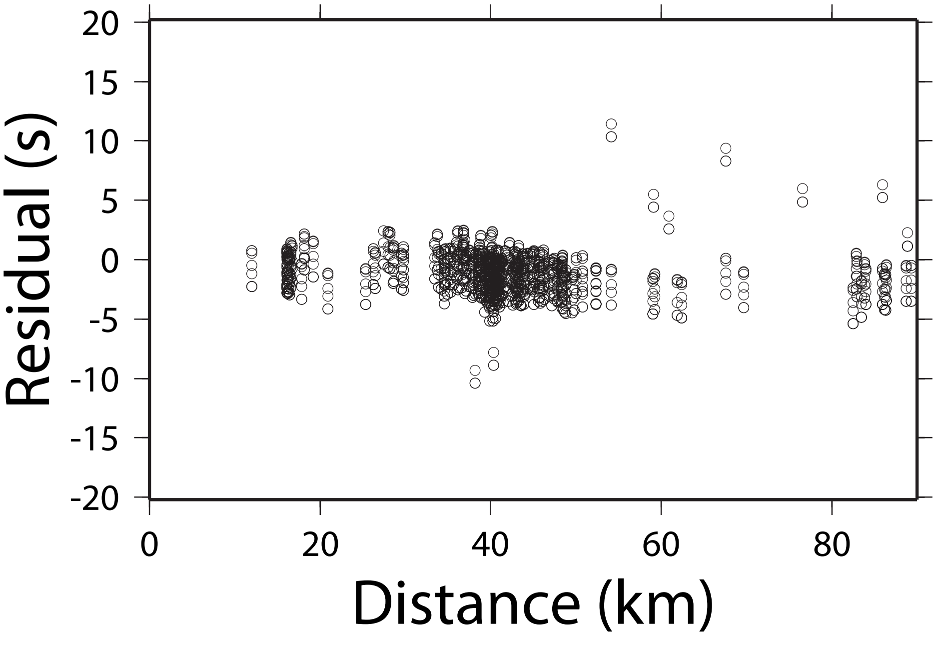

Figure A5. Weighted and unweighted residuals from the origin time recalculation as a function of distance for Event 6 (Iran 4/30/99).

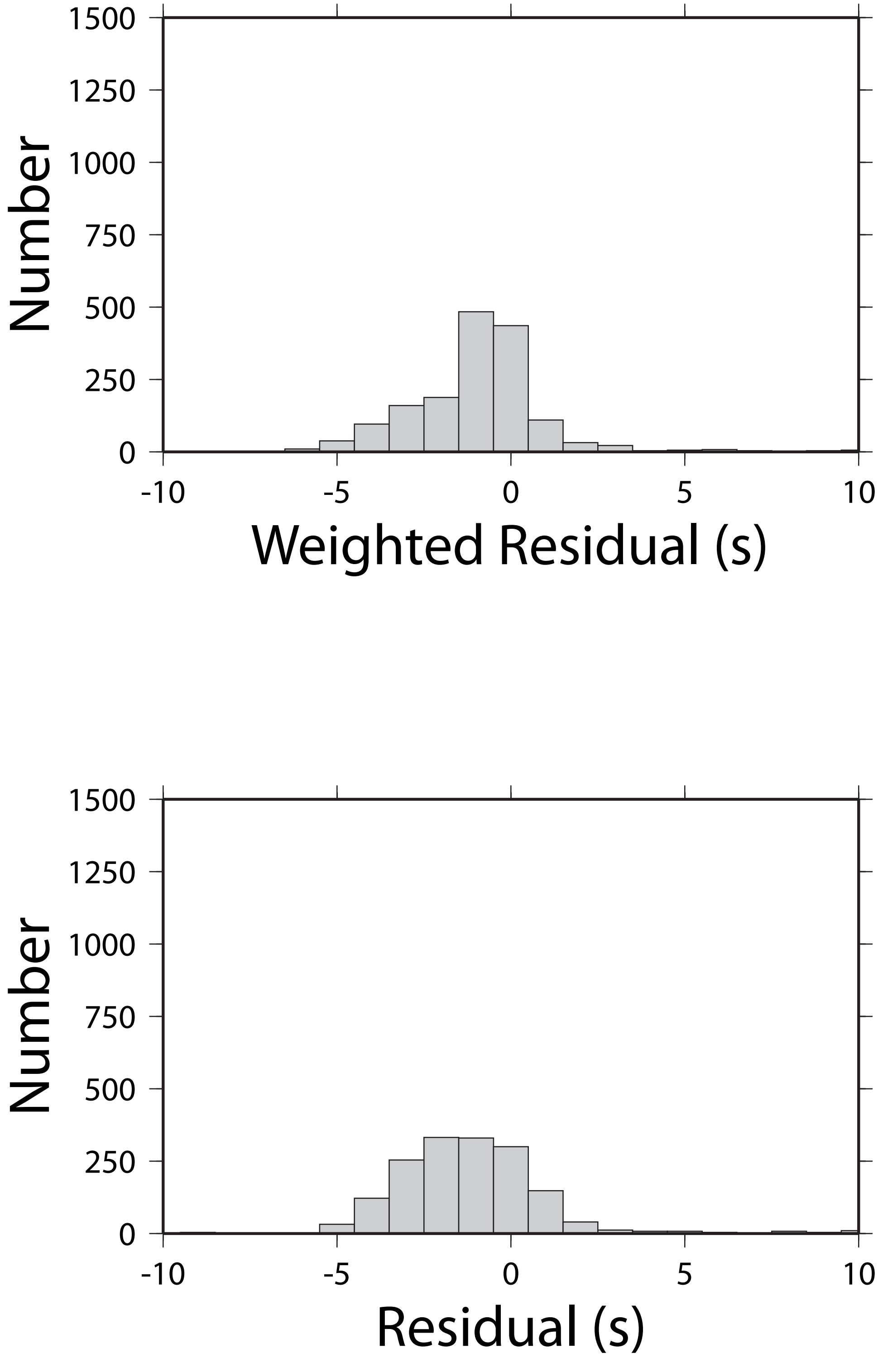

Figure A6. Histograms of weighted and unweighted residuals from the origin time recalculation for Event 6 (Iran 4/30/99).

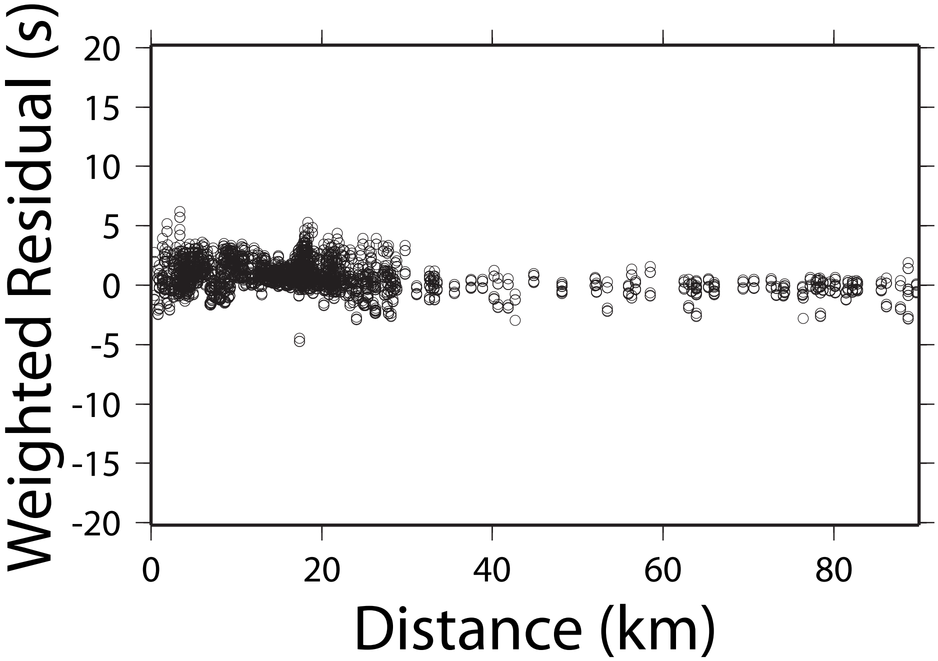

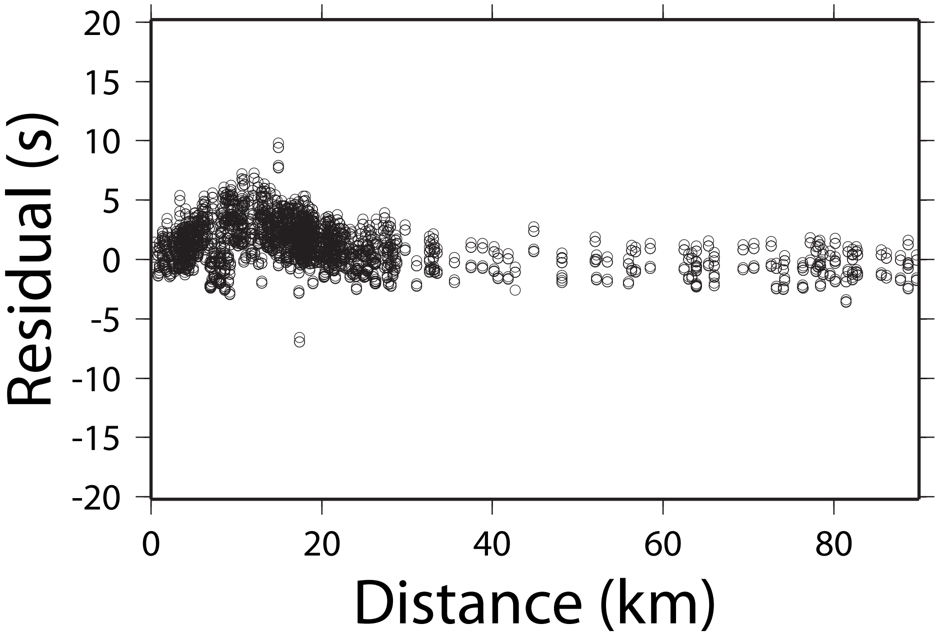

Figure A7. Weighted and unweighted residuals from the origin time recalculation as a function of distance for Event 7 (SW Turkey, 12/20/04).

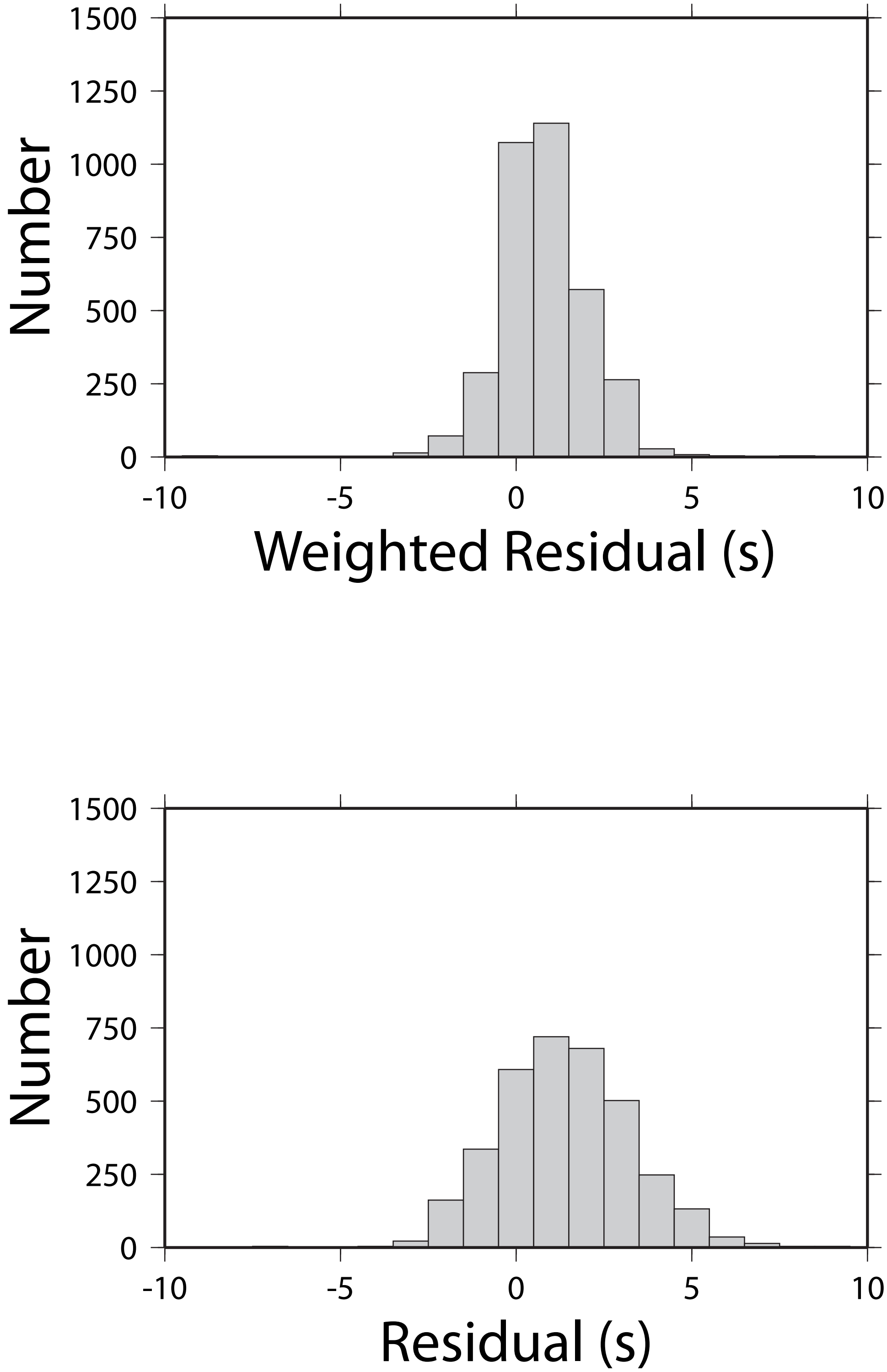

Figure A8. Histogams of weighted and unweighted residuals from the origin time recalculation for Event 7 (SW Turkey, 12/20/04).

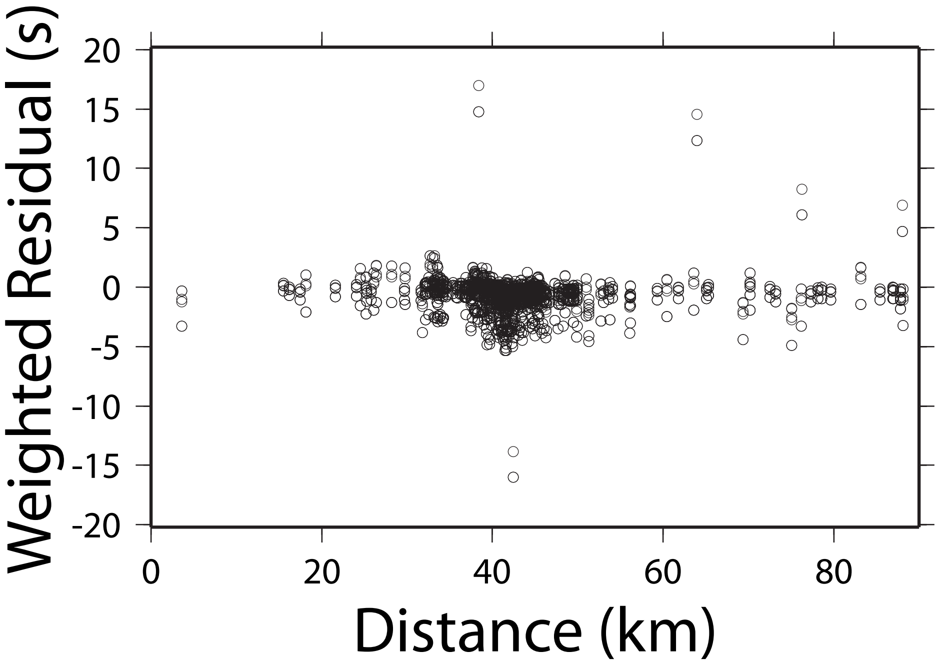

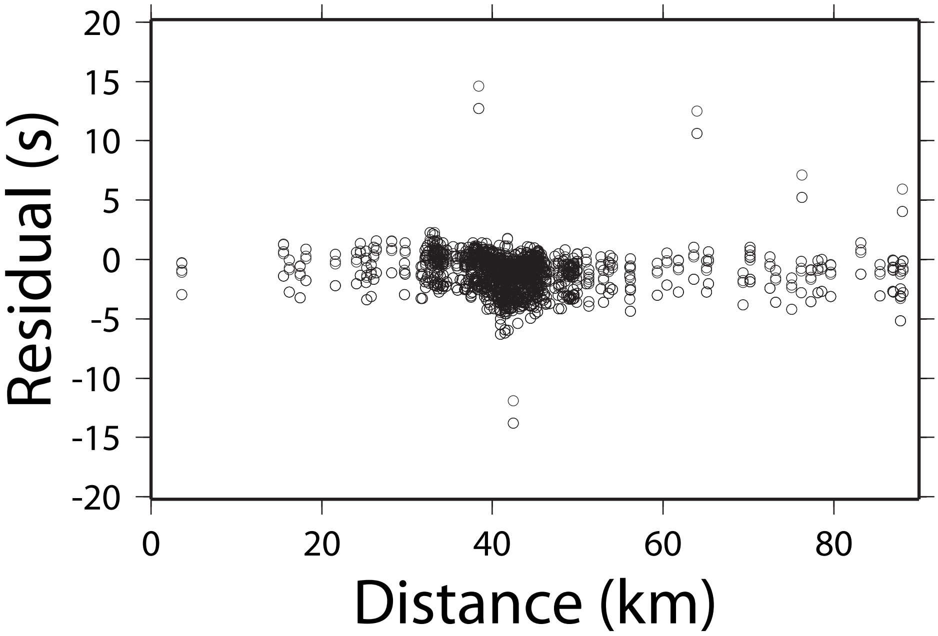

Figure A9. Weighted and unweighted residuals from the origin time recalculation as a function of distance for Event 8 (Eritrea, 10/22/04).

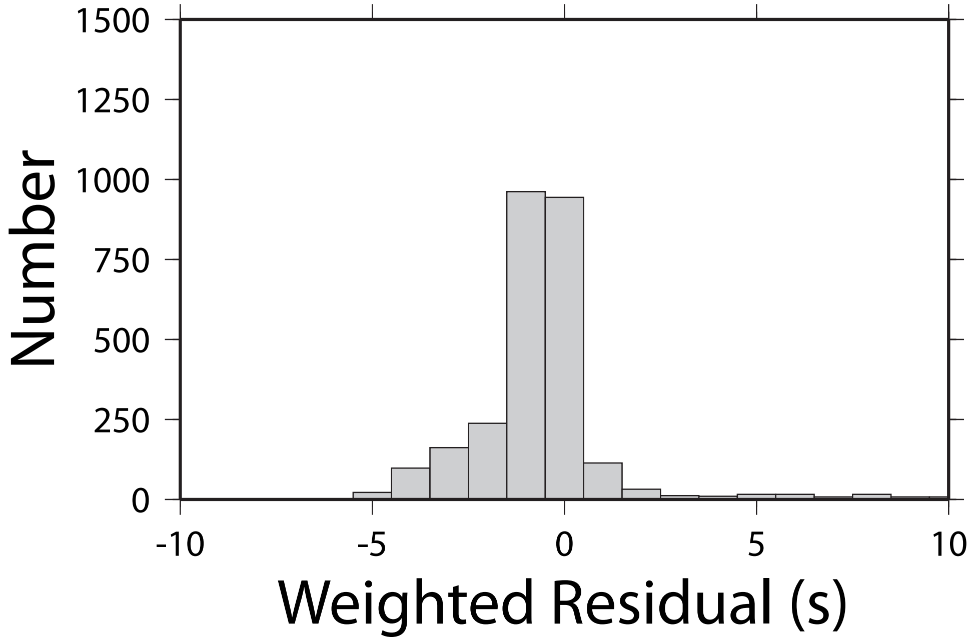

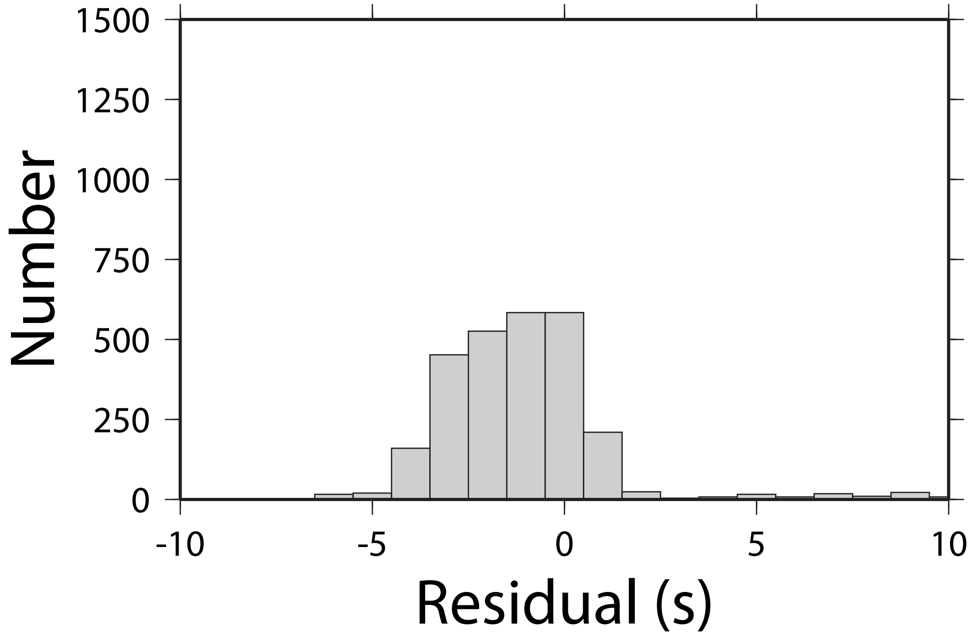

Figure A10. Histograms of weighted and unweighted residuals from the origin time recalculation for Event 8 (Eritrea, 10/22/04).

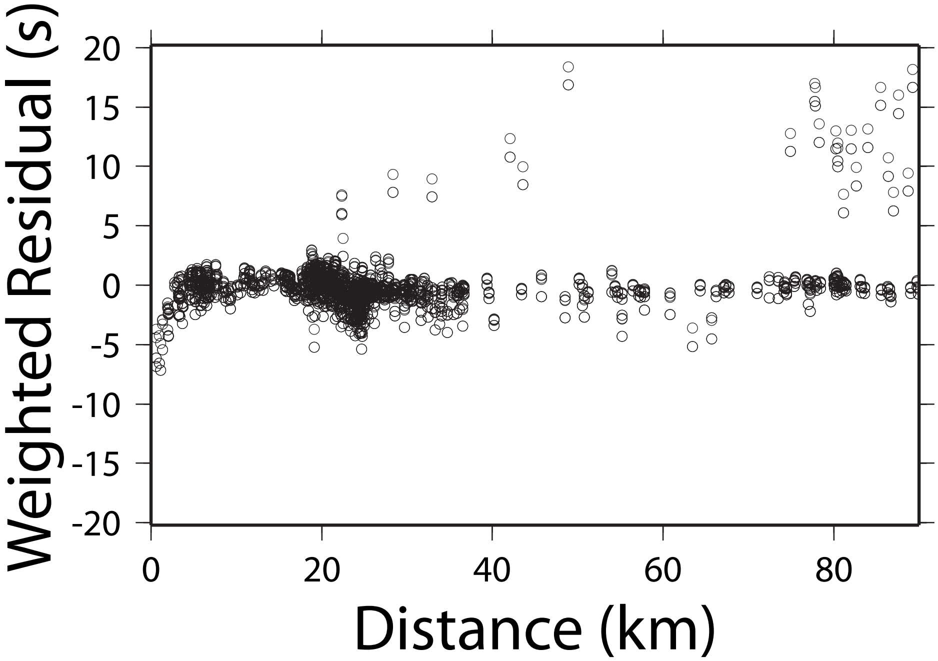

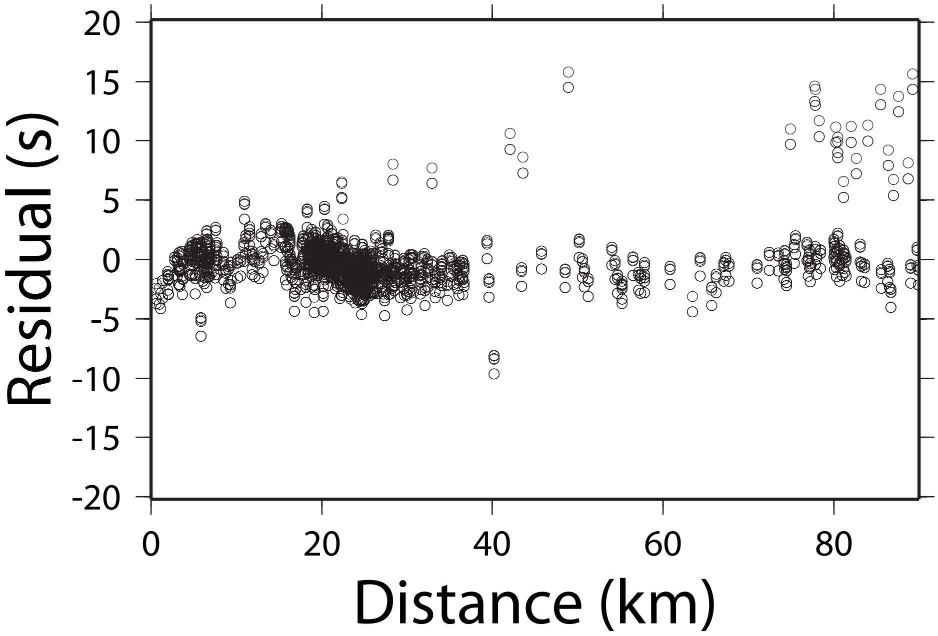

Figure A11. Weighted and unweighted residuals from the origin time recalculation as a function of distance for Event 9 (Turkey, 8/11/04).

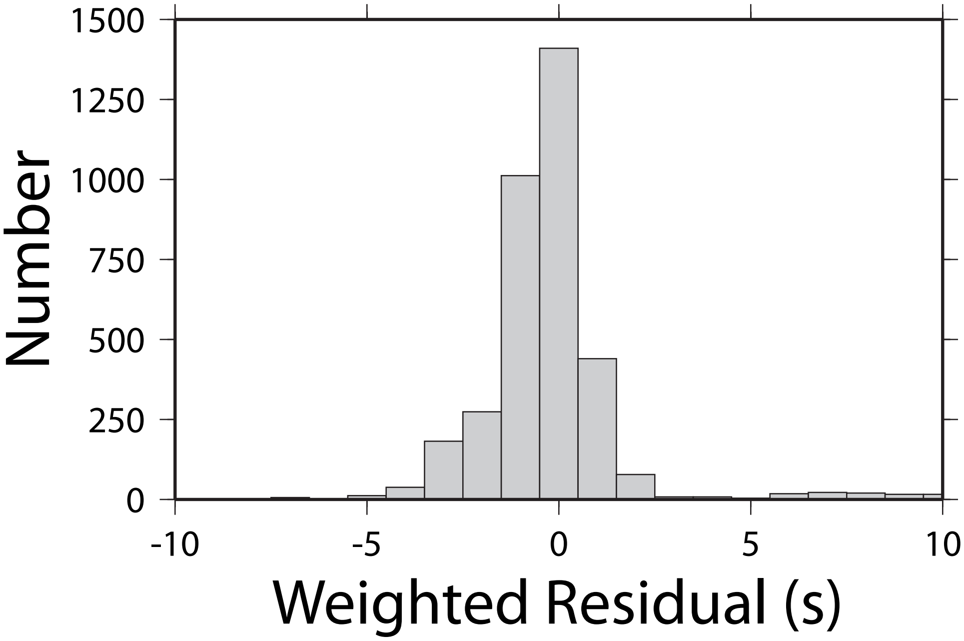

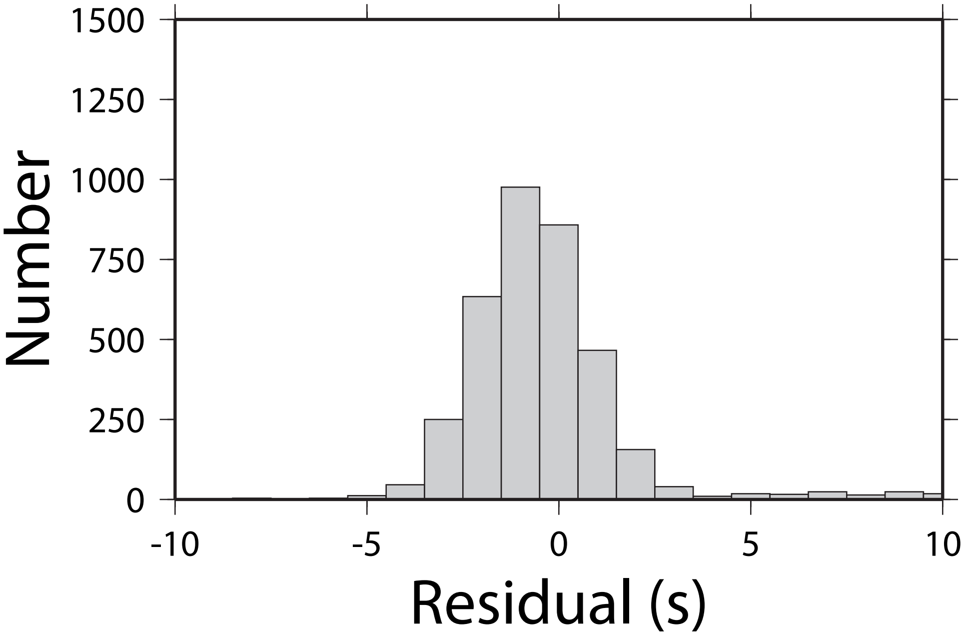

Figure A12. Histograms of weighted and unweighted residuals from the origin time recalculation for Event 9 (Turkey, 8/11/04).

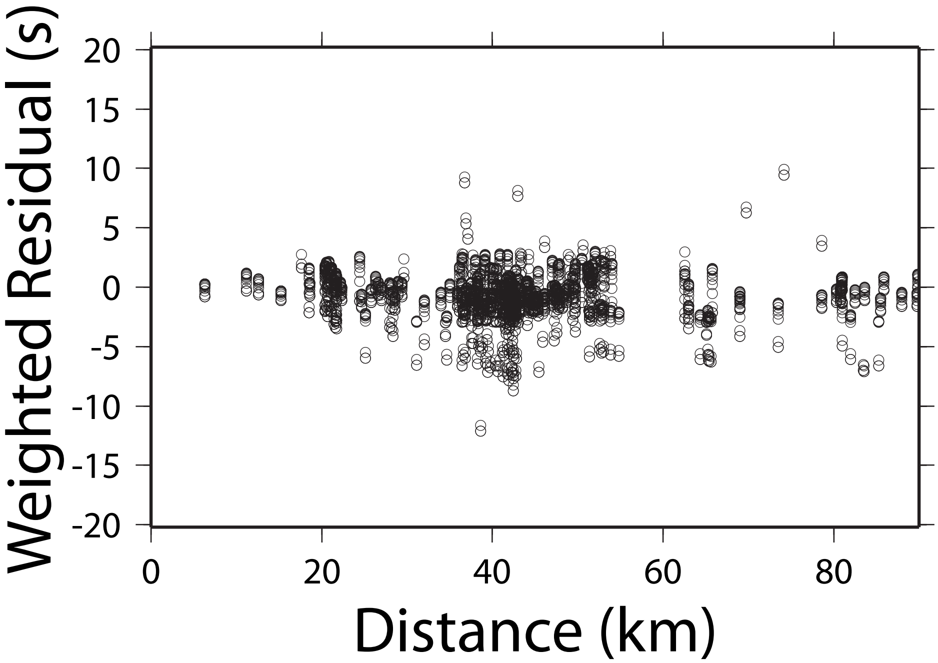

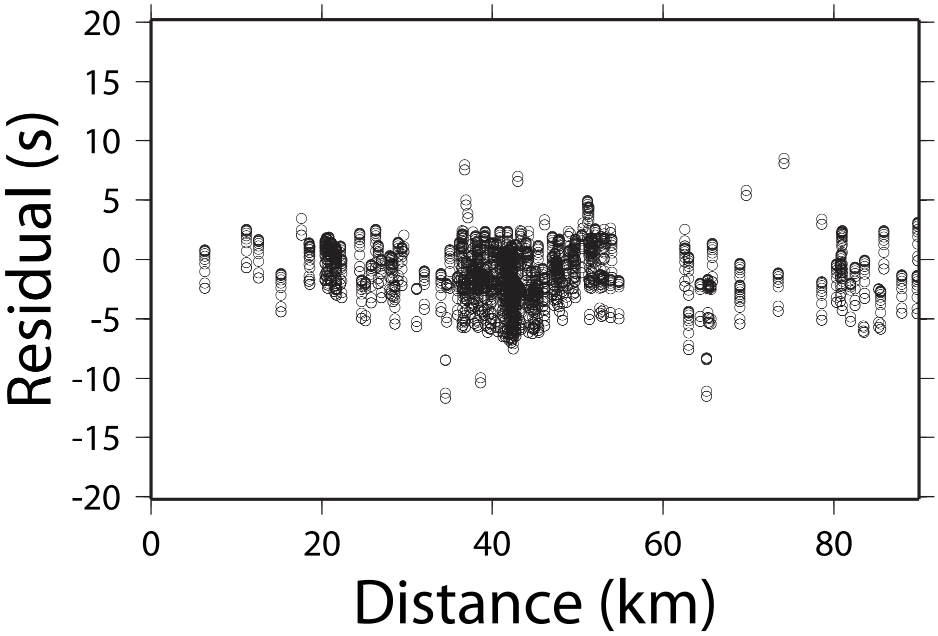

Figure A13. Weighted and unweighted residuals from the origin time recalculation as a function of distance for Event 10 (Iran, 4//10/98).

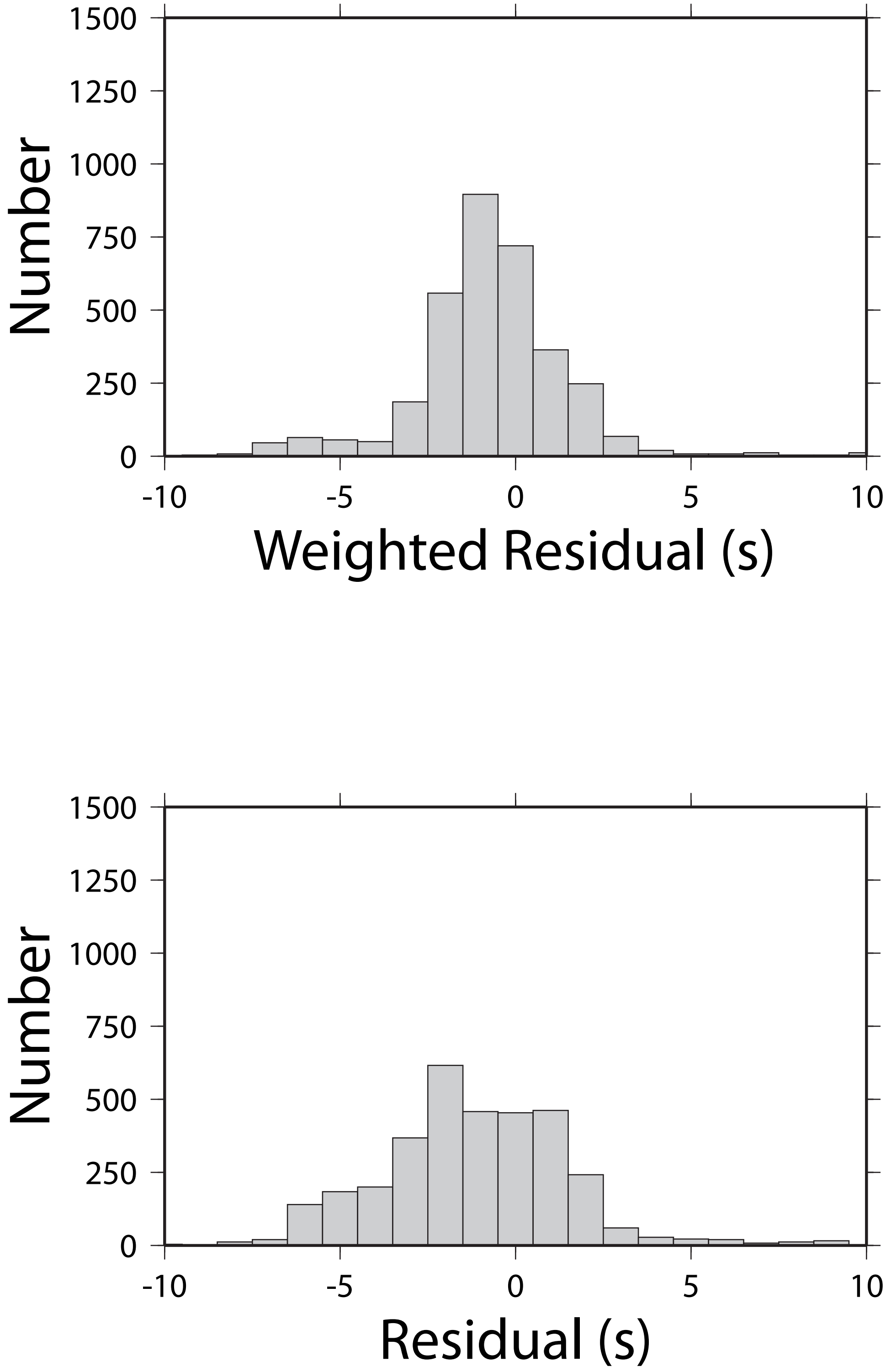

Figure A14. Histograms of weighted and unweighted residuals from the origin time recalculation for Event 10 (Iran, 4//10/98).

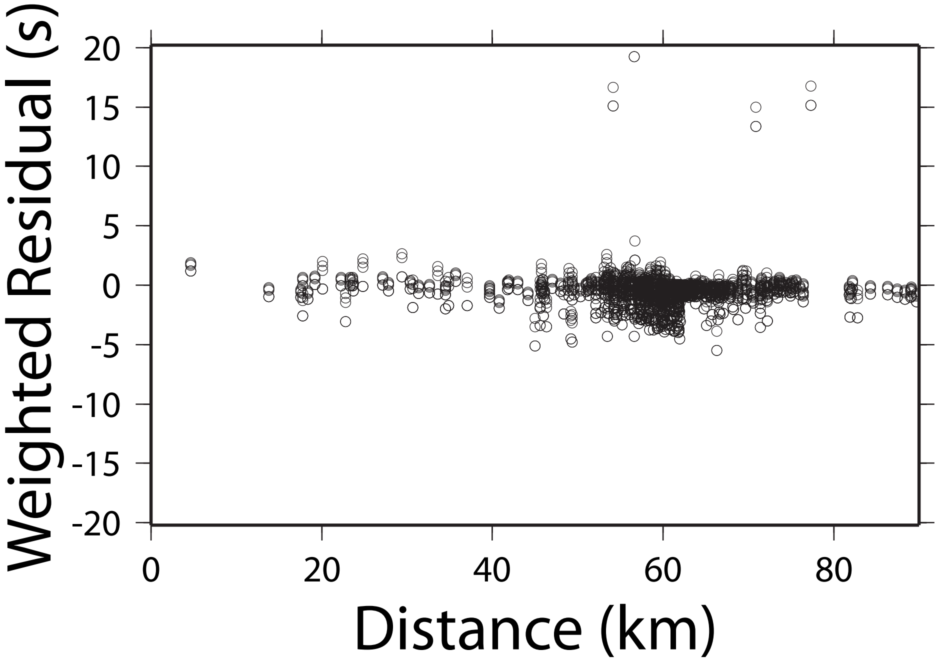

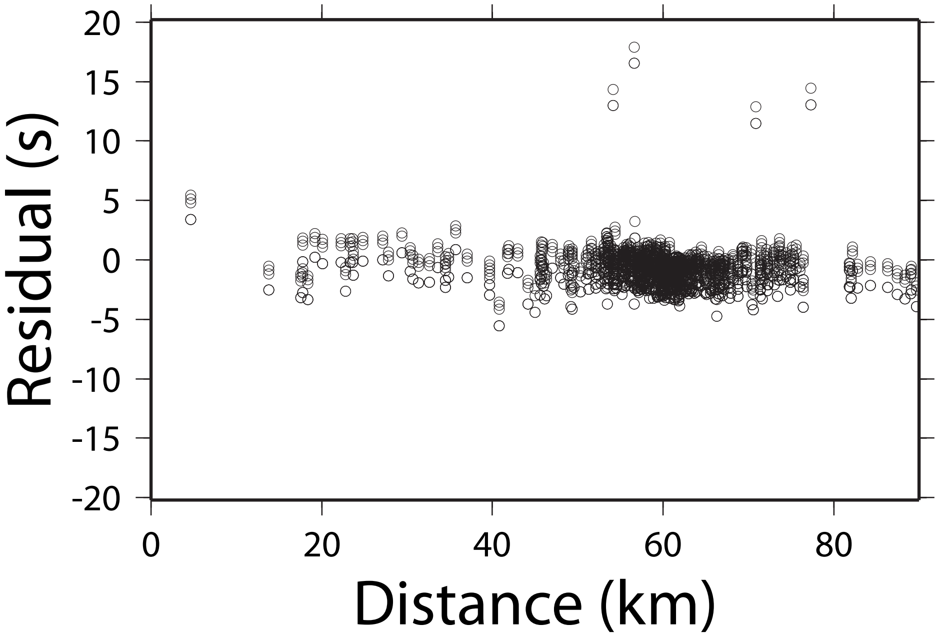

Figure A15. Weighted and unweighted residuals from the origin time recalculation as a function of distance for Event 13 (Tibet, 3/27/04).

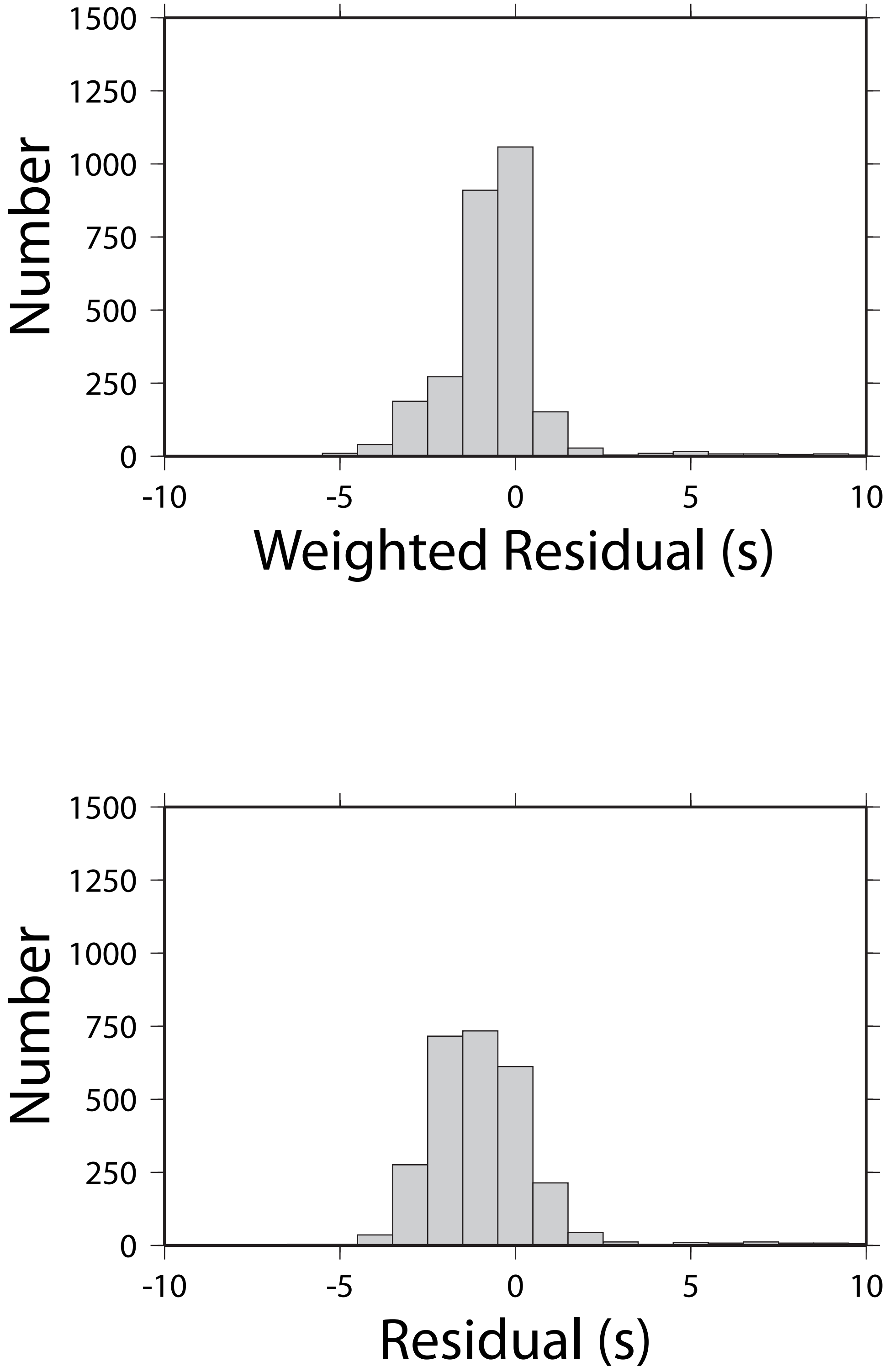

Figure A16. Histograms of weighted and unweighted residuals from the origin time recalculation for Event 13 (Tibet, 3/27/04).

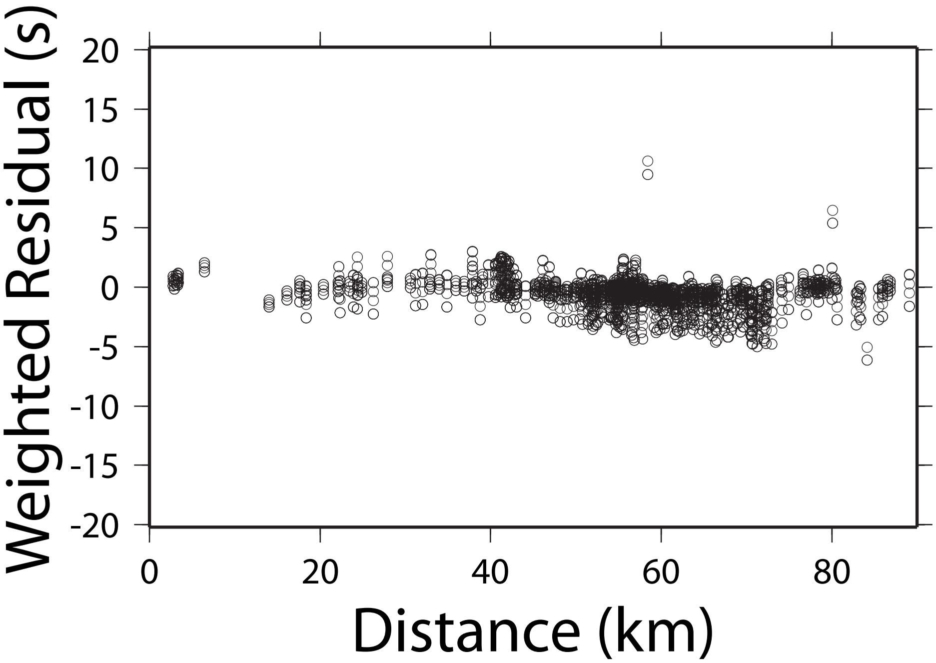

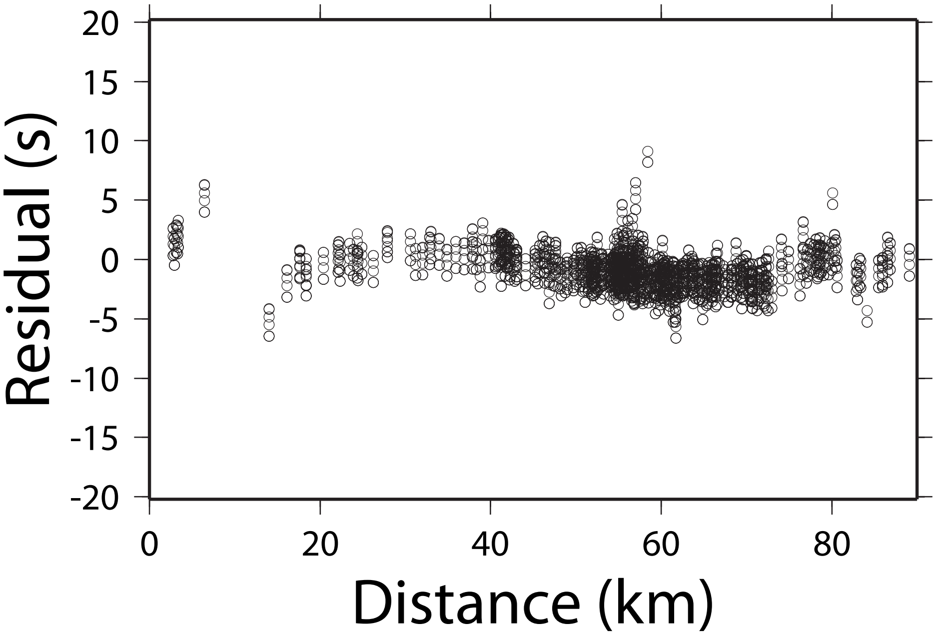

Figure A17. Weighted and unweighted residuals from the origin time recalculation as a function of distance for Event 17 (Tibet, 7/11/04).

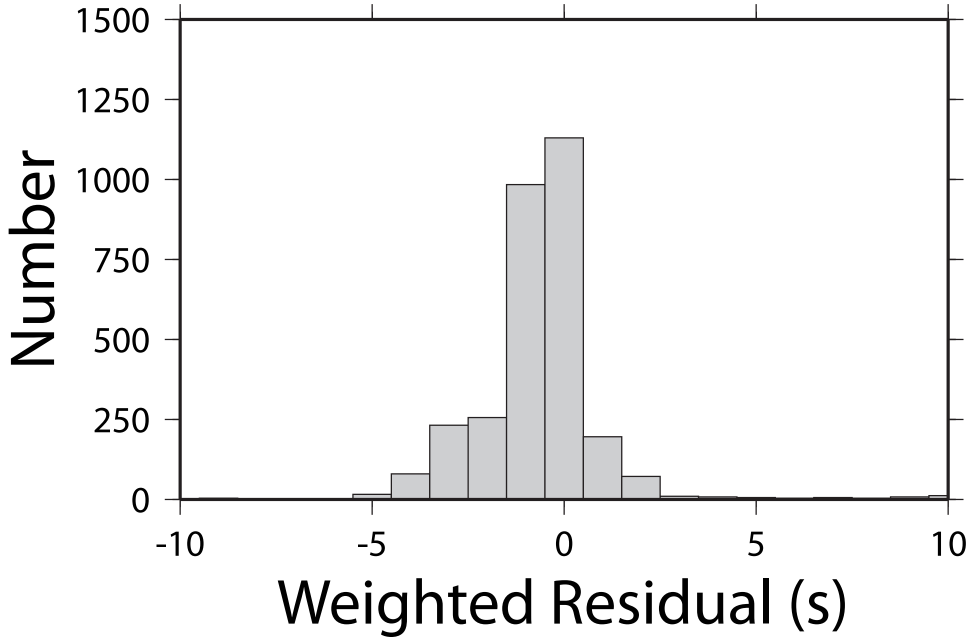

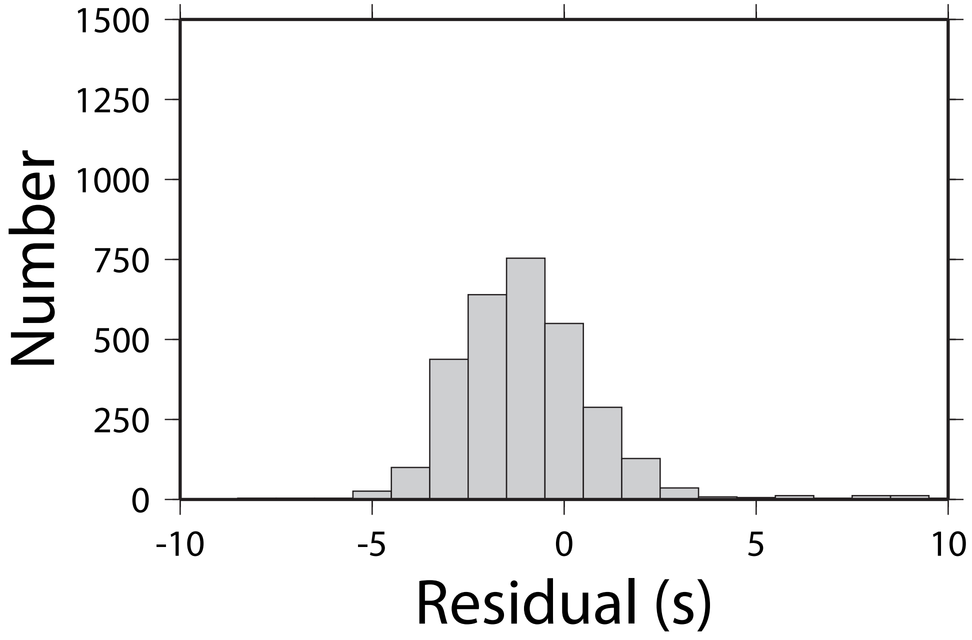

Figure A18. Historgams of weighted and unweighted residuals from the origin time recalculation for Event 17 (Tibet, 7/11/04).

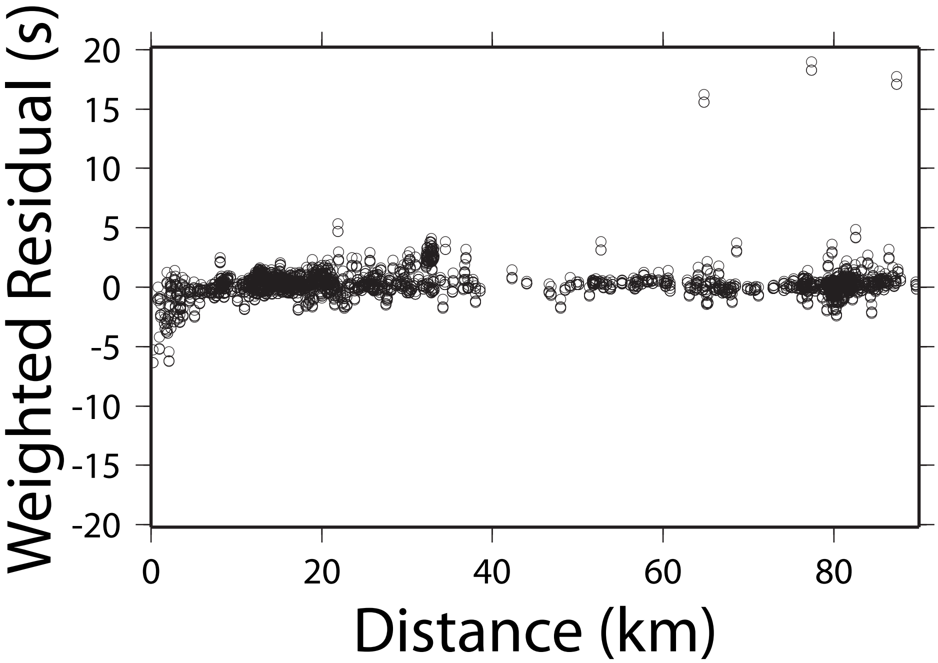

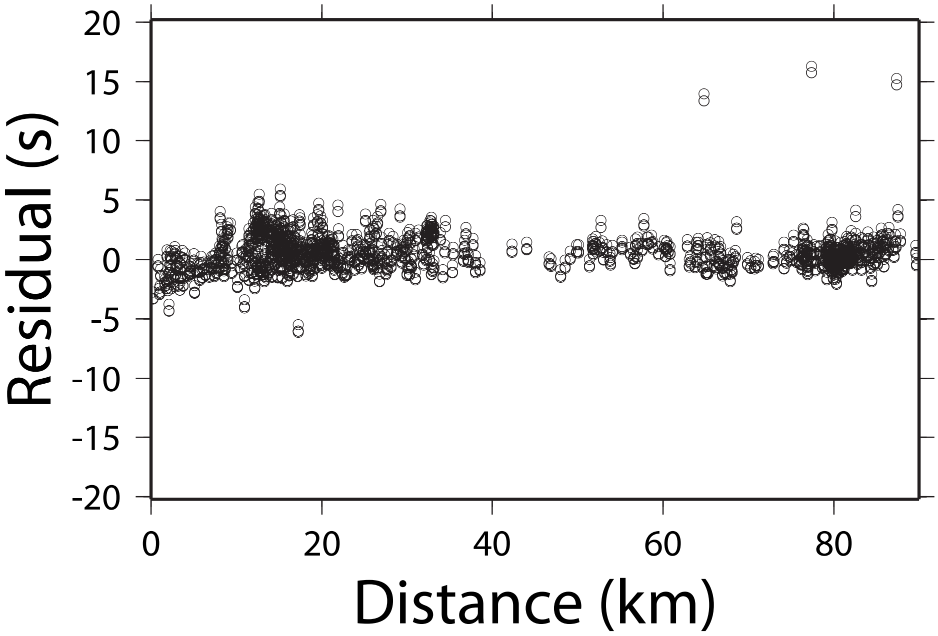

Figure A19. Weighted and unweighted residuals from the origin time recalculation as a function of distance for Event 18 (Morocco, 4/24/04).

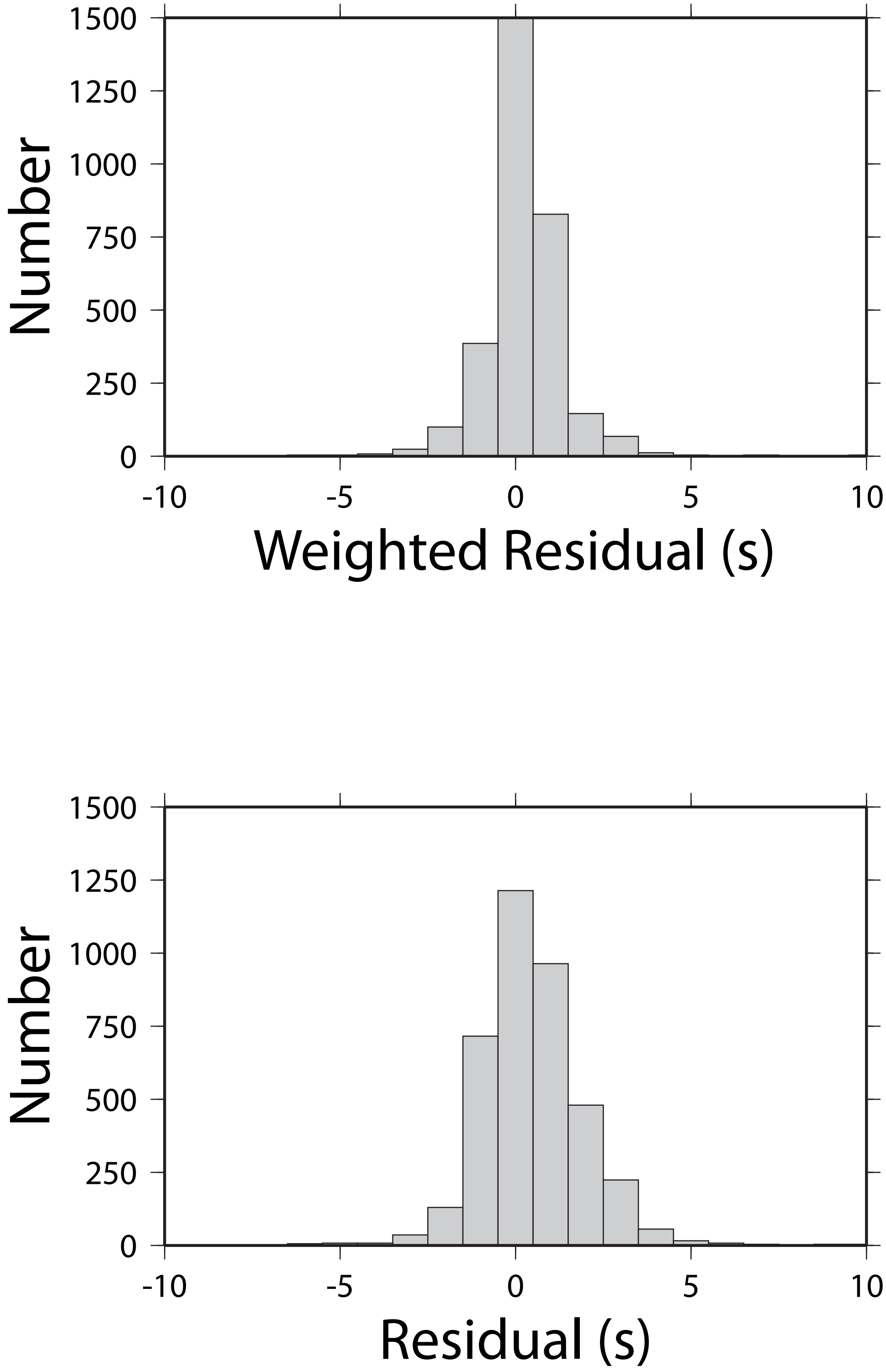

Figure A20. Histograms of weighted and unweighted residuals from the origin time recalculation for Event 18 (Morocco, 4/24/04).

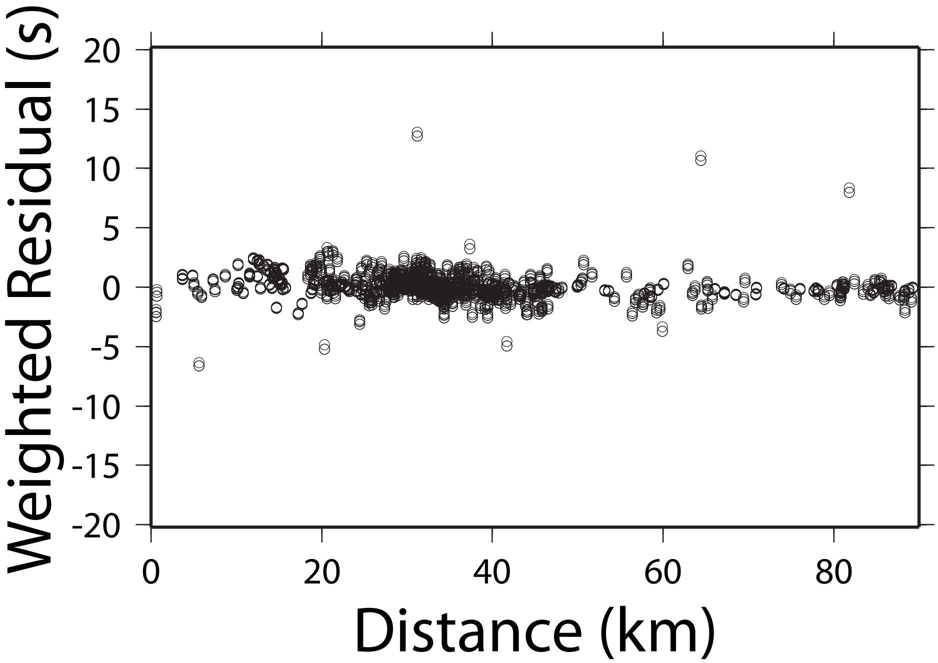

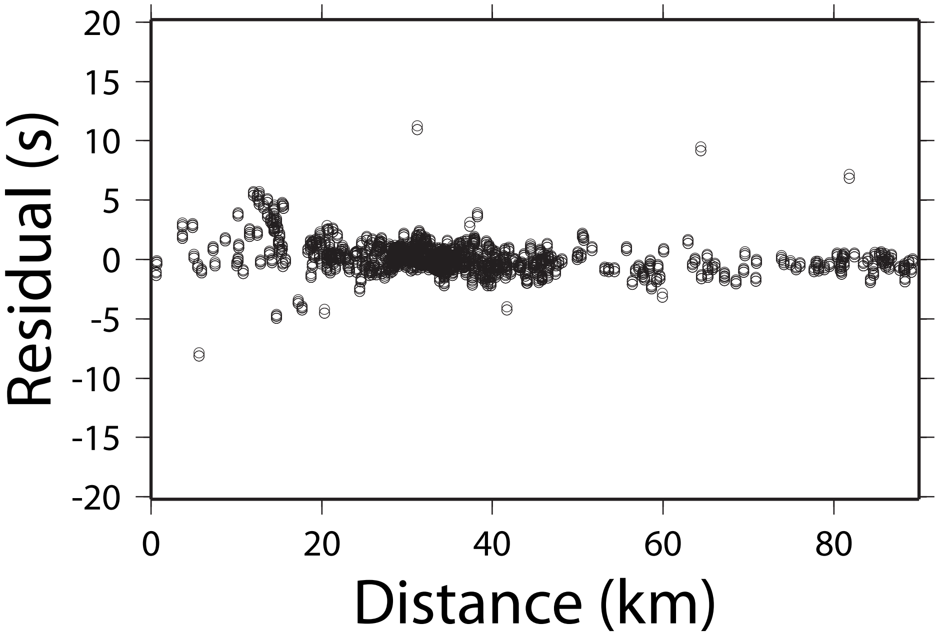

Figure A21. Weighted and unweighted residuals from the origin time recalculation as a function of distance for Event 19 (Iran, 5/28/04).

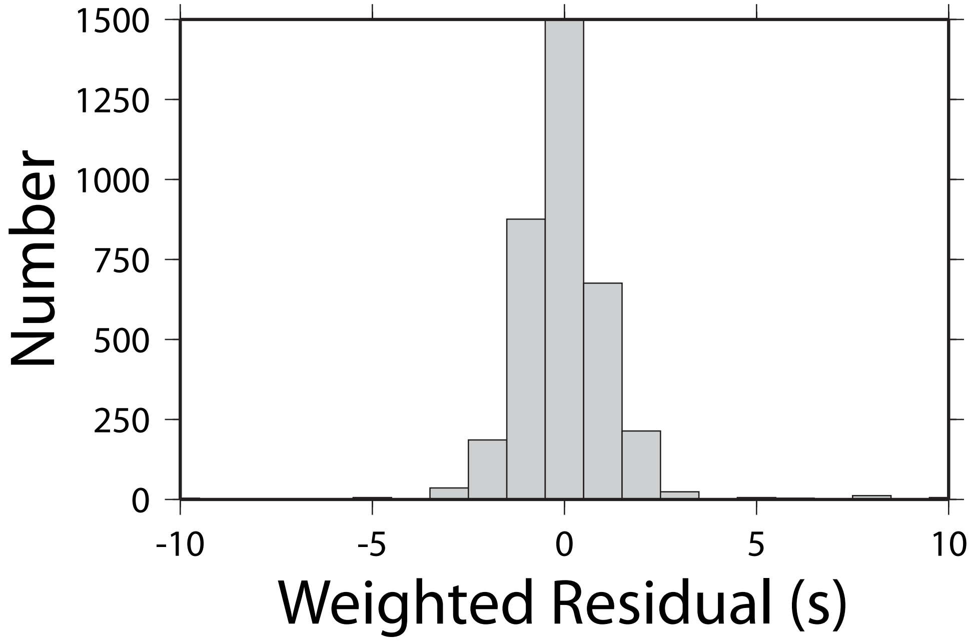

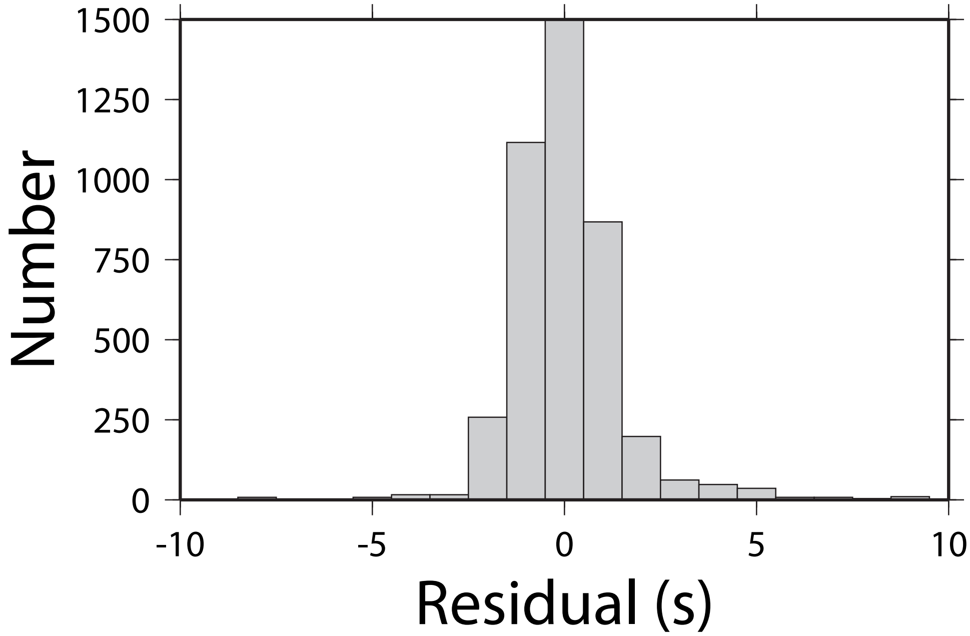

Figure A22. Histograms of weighted and unweighted residuals from the origin time recalculation for Event 19 (Iran, 5/28/04).

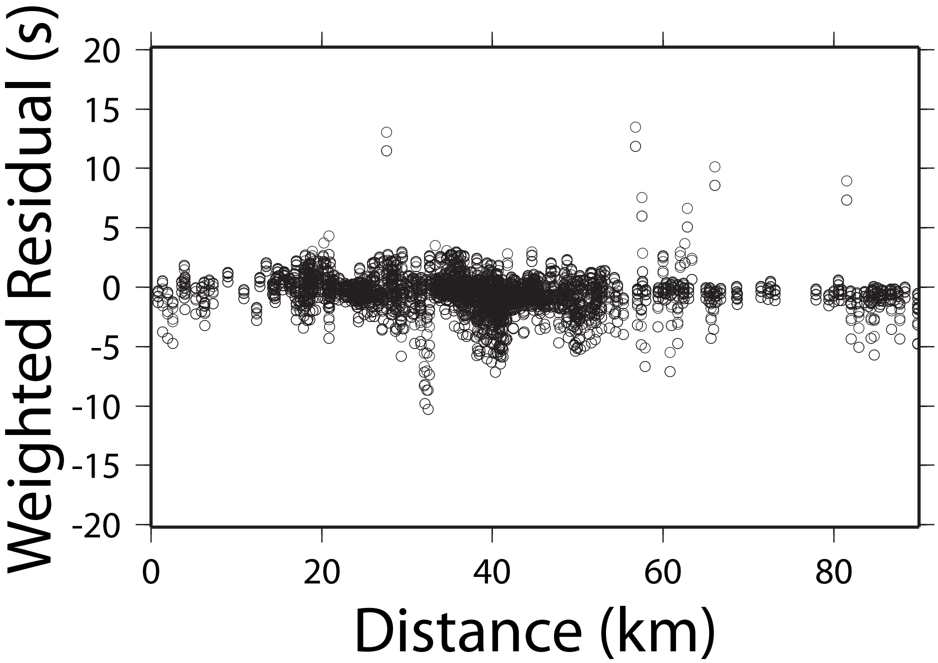

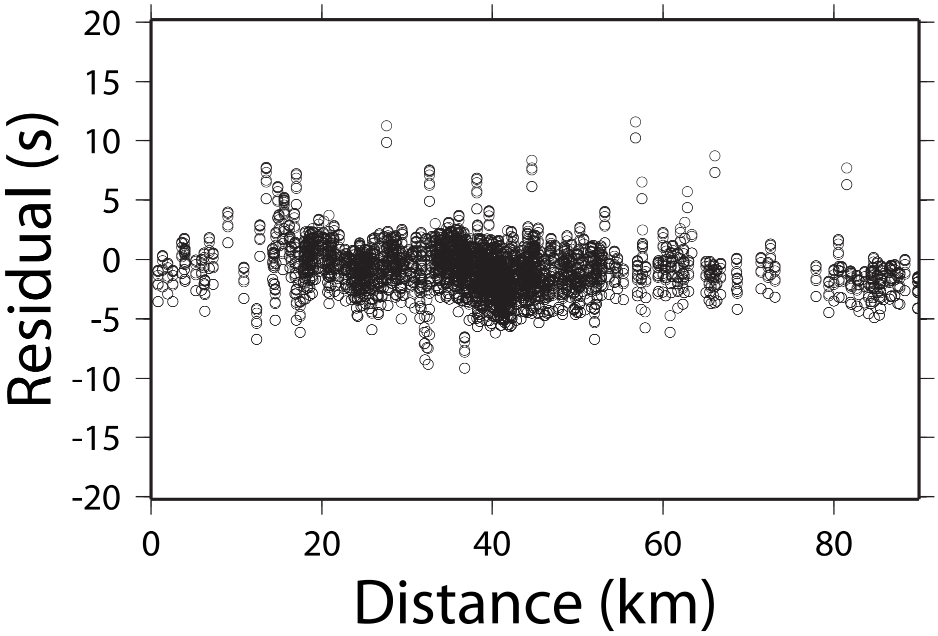

Figure A23. Weighted and unweighted residuals from the origin time recalculation as a function of distance for Event 20 (Iran, 2/22/05).

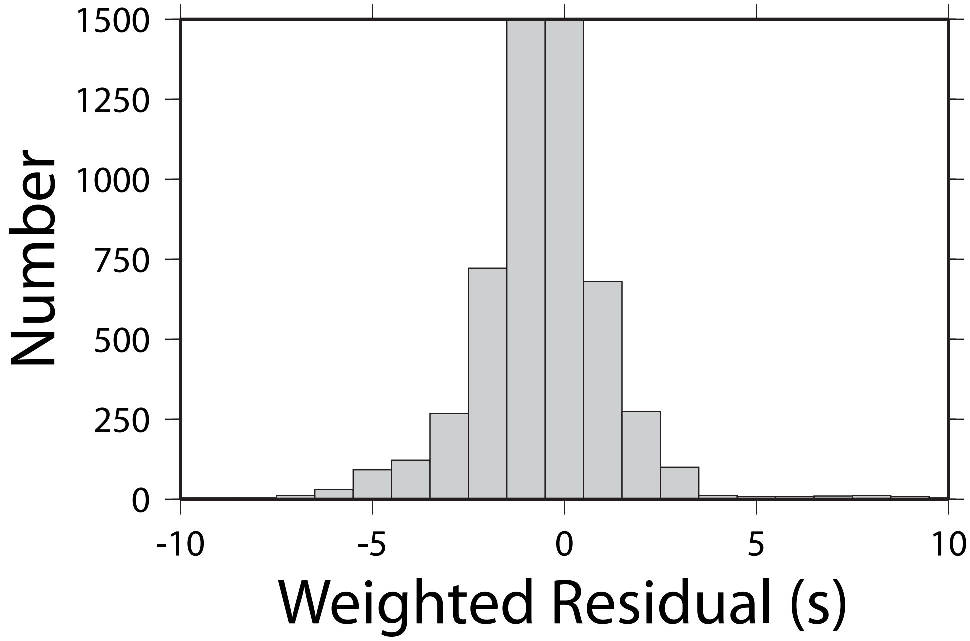

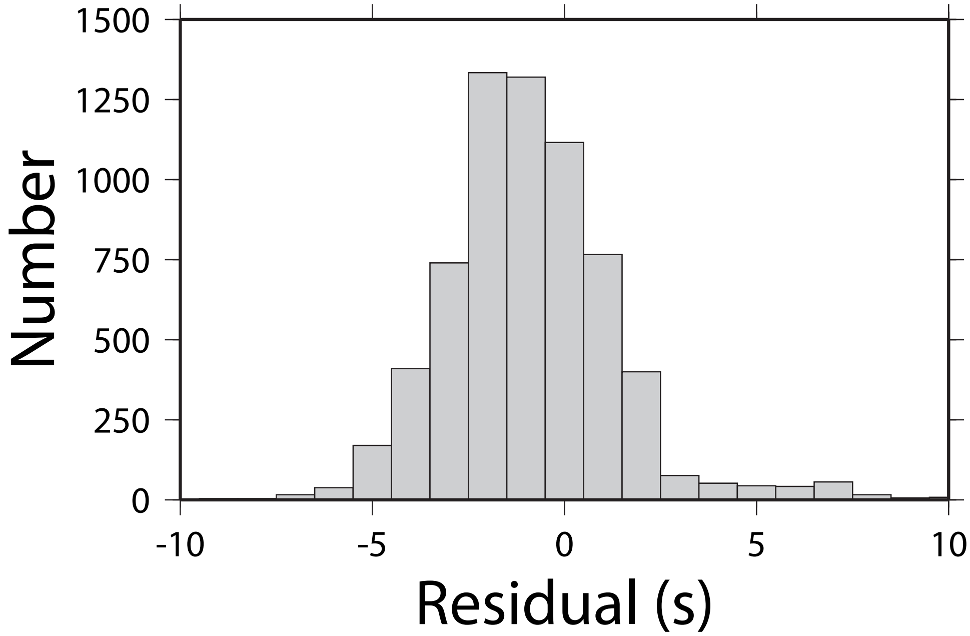

Figure A24. Histograms of weighted and unweighted residuals from the origin time recalculation for Event 20 (Iran, 2/22/05).